JOURNAL OF PETROLOGY

Journal of Petrology, 2016, Vol. 57, No. 1, 185–228
doi: 10.1093/petrology/egw005
Original Article

OXFORD

Prolonged Ediacaran–Cambrian Metamorphic History and Short-lived High-pressure Granulite-facies Metamorphism in the H.U. Sverdrupfjella, Dronning Maud Land (East Antarctica): Evidence for Continental Collision during Gondwana Assembly

Jim Pauly[1†], Horst R. Marschall[2]*, Hans-Peter Meyer[3], Nilanjan Chatterjee[4] and Brian Monteleone[2]

[1]Institut für Geologie, Universität Bern, Baltzerstraße 1 + 3, 3012 Bern, Switzerland; [2]Woods Hole Oceanographic Institution, 266 Woods Hole Road, Woods Hole, MA 02543, USA; [3]Institut für Geowissenschaften, Universität Heidelberg, Im Neuenheimer Feld 234–236, 69120 Heidelberg, Germany and [4]Department of Earth, Atmospheric and Planetary Sciences, Massachusetts Institute of Technology, Cambridge, MA 02139, USA

*Corresponding author. Telephone: +1 508 289-2776. E-mail: hmarschall@whoi.edu
[†]Present address: 33, rue Dr Welter, L-3879 Schifflange, Luxembourg.

Received July 17, 2014; Accepted January 19, 2016

ABSTRACT

The H.U. Sverdrupfjella is part of the high-grade Maud Belt in Dronning Maud Land (East Antarctica), which was located in a central position of the Gondwana supercontinent. Here we study high-pressure granulites from the eastern H.U. Sverdrupfjella and present a detailed reconstruction of the *P–T–t* history based on a combination of Zr-in-rutile and Ti-in-zircon thermometry, zircon U–Pb dating, monazite chemical dating, garnet diffusion modelling and petrological modelling. Peak metamorphic conditions of ~930°C and 1·45 GPa persisted for less than 6 Myr and were attained at 570 ± 7 Ma, embedded in a well-documented clockwise loading, heating, and decompression path. The rocks had already been rapidly exhumed to a crustal depth of ~30 km at 556 ± 7 Ma. In addition to the very short-lived ultrahigh-temperature peak, zircon preserves evidence for protracted granulite-facies conditions with temperatures above 800°C from as early as *c.* 590 Ma, persisting for *c.* 40 Myr. Constraints on prograde metamorphism are recorded in zircon and in rutile inclusions in garnet. Zr-in-rutile thermometry using rutile included in different generations of garnet is used to reconstruct the prograde *P–T* path, documenting burial followed by heating to ultrahigh temperatures at peak pressures. Complementary Ti zonation in prograde cores of zircon grains documents and dates heating and peak temperatures, whereas younger zircon rims show lower Ti-in-zircon temperatures and date the retrograde stages of metamorphism. Our results provide the first evidence for Neoproterozoic high-pressure granulite-facies metamorphism and ultrahigh-temperature conditions for this region. The clockwise loading–heating path and the peak *P–T* conditions strongly indicate that the rocks preserved in Dronning Maud Land were part of the lower plate during a continent–continent collision event related to Gondwana assembly at *c.* 570 Ma. The metamorphic evolution determined in this study and the correlation with similar *P–T* evolutions documented in adjacent terranes favour the continuation of the *c.* 580–560 Ma Mozambique Belt into Dronning Maud Land. Furthermore, the striking contemporaneity of the metamorphism in the different parts of central Gondwana suggests that the Coats Land Block was part of greater India prior to this collision.

Key words: high-pressure granulite; monazite; rutile thermometry; zircon thermometry; zircon geochronology

INTRODUCTION

Orogenesis, the formation of mountain belts, is a major plate tectonic process that subjects rocks of the continental crust to metamorphism, deformation and anatexis. The roots of ancient mountain belts are witnesses to continental collision processes in Earth's history, and can be used as archives to reconstruct the palaeogeography and amalgamation of continents and supercontinents. High-temperature–high-pressure (HT–HP) metamorphic terranes are typically found in the internal zones of orogens; they record processes in the otherwise inaccessible deep crustal roots.

HP granulites are crustal rocks equilibrated at high temperatures at deep crustal or upper mantle levels. They are thus indicators of major plate tectonic processes, such as crustal thickening above subduction zones, in back-arcs or along continental arcs, or stacking or doubling of the crust in the course of continental collision (e.g. Harley, 1989, 1998; Bohlen, 1991; O'Brien & Rötzler, 2003). HP granulites have equilibrated at the extreme end of crustal metamorphism, forming in some cases at ultrahigh temperatures (UHT) in excess of 900°C at depths in excess of 50 km. HP–UHT granulites are the best indicators of continent–continent collision, and have been identified, for example, in the internal orogenic zone of the Variscan orogen of central Europe (Marschall *et al.*, 2003; O'Brien & Rötzler, 2003). In this study, we describe the pressure–temperature–time evolution of newly discovered high-pressure granulites from the Ediacaran–Cambrian Maud Belt in Dronning Maud Land (DML), East Antarctica, and discuss their implications for Neoproterozoic continental collision during the assembly of the Gondwana supercontinent.

GEOLOGICAL SETTING

The H.U. Sverdrupfjella (0°30′W to 1°40′E and 72°00′S to 72°50′S) is situated in Western DML and covers *c.* 6000 km^2 (Groenewald & Hunter, 1991; Fig. 1a). The mountain range forms part of the high-grade Maud Belt of DML, which is characterized by plutonic igneous rocks and amphibolite- to granulite-facies metamorphic rocks, extending for some 1800 km from the Lützow–Holmbukta in the east (*c.* 40°E) to the Heimefrontfjella (*c.* 12°W) near the Weddell Sea in the west. In Western DML, the Maud Belt borders the Archean Grunehogna Province (Fig. 1a). Geographically, the Maud Belt in Western DML is subdivided from NE to SW into the H.U. Sverdrupfjella, the Kirwanveggen and the Heimefrontfjella (e.g. Krynauw, 1996; Fig. 1). The area south of the Maud Belt is covered in ice and provides no rock outcrop.

The Grunehogna Province is thought to represent a fragment of the Kalahari Craton of southern Africa (Fig. 2) that became detached during the Jurassic break-up of Gondwana (e.g. Dietz & Sproll, 1970; Smith & Hallam, 1970; Martin & Hartnady, 1986; Groenewald *et al.*, 1991, 1995; Moyes *et al.*, 1993*a*; Jacobs *et al.*, 1998, 2008*a*; Fitzsimons, 2000; Marschall *et al.*, 2010, 2013*b*). The Kalahari–Grunehogna Craton had existed since at least 3·1 Ga, and its break-up was probably facilitated by Jurassic reactivation of large Ediacaran–Cambrian shear zones that formed during SW-directed escape tectonics in the course and aftermath of Neoproterozoic continental collision (Jacobs & Thomas, 2004).

The Maud Belt mainly consists of meta-igneous and meta-sedimentary rocks that were metamorphosed under amphibolite- to granulite-facies conditions (e.g. Grantham *et al.*, 1995; Groenewald *et al.*, 1995; Board *et al.*, 2005; Pant *et al.*, 2013; Grosch *et al.*, 2015). Two orogenic events were responsible for the high-grade metamorphism: the Mesoproterozoic or Grenville-age orogeny (1090–1030 Ma) related to the assembly of the Rodinia supercontinent, and the Neoproterozoic to early Phanerozoic Pan-African orogeny (650–480 Ma) related to the amalgamation of Gondwana (Arndt *et al.*, 1991; Groenewald *et al.*, 1995; Jacobs *et al.*, 2003*a*, 2003*b*, 2008*b*; Board *et al.*, 2005; Bisnath *et al.*, 2006).

The reconstruction of the Neoproterozoic–Cambrian collision includes the correlation of high-grade metamorphic terrains and their timing with the northern extension of the Maud Belt to the Mozambique Belt in southeastern Africa (e.g. Arndt *et al.*, 1991; Groenewald *et al.*, 1991; Jacobs *et al.*, 1998, 2003*a*, 2008*a*; Wareham *et al.*, 1998; Grantham *et al.*, 2013; Fig. 2). The back-rotation of East Antarctica into its most appropriate position within Palaeozoic Gondwana aligns the Antarctic coastline and the Maud Belt with Mozambique, Sri Lanka and southern India, and it places the Grunehogna Craton in contact with the Kaapvaal Craton of South Africa (e.g. Boger, 2011; Harley *et al.*, 2013; Harley, 2003; Fig. 2). Jacobs and co-workers (Jacobs, 1999; Jacobs *et al.*, 2003*a*, 2008*a*; Jacobs & Thomas, 2004) argued for a continuous East African–Antarctic collisional orogen extending for ~8000 km from Arabia to southwestern Dronning Maud Land and to some smaller crustal blocks at the Palaeo-Pacific coast of Gondwana.

The western limit of the East African–Antarctic orogen and the limit of associated high-grade metamorphism is well defined in the Heimefrontfjella by a major shear zone (Jacobs *et al.*, 1995, 2003*a*; Fig. 1a). In the H.U. Sverdrupfjella, the Neoproterozoic orogenic front is probably obscured by the ~60 km wide Jutulstraumen–Pencksøkket glaciers (Fig. 1a), which separate the

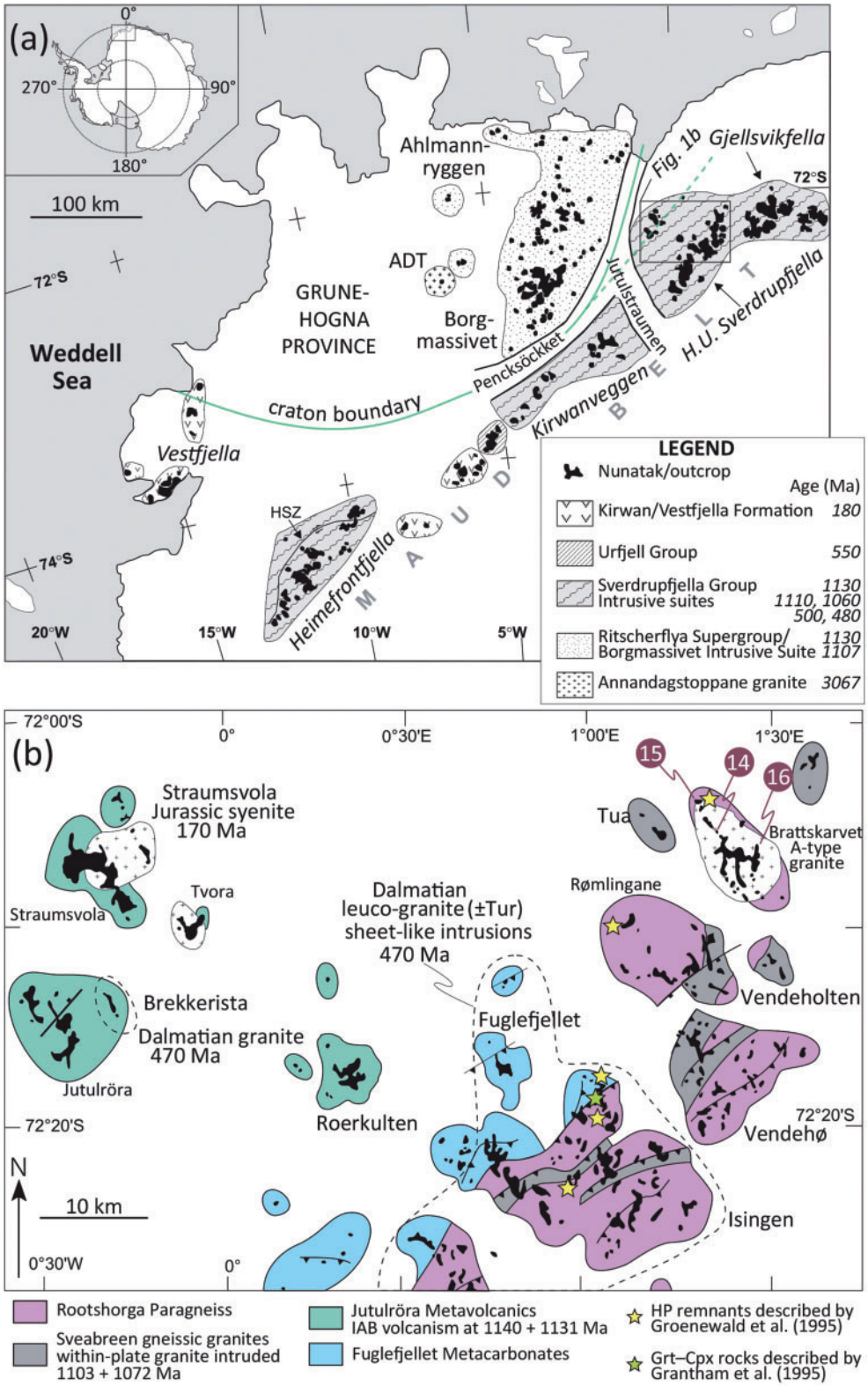

Fig. 1. (a) Simplified map of Dronning Maud Land (DML) (modified after Board *et al.*, 2005). The major geological units are the high-grade metamorphic Maud Belt (Meso- and Neoproterozoic), Mesoproterozoic sediments and sills in the Ritscherflya Supergroup (including Ahlmannryggen and Borgmassivet), and the Archaean basement of the Grunehogna Craton (exposed at Annandagstoppane, ADT). The H.U. Sverdrupfjella is part of the Maud Belt. The inset shows the Antarctic continent with the location of DML at the edge of the Weddell Sea. (b) Simplified map of the northern part of H.U. Sverdrupfjella [modified after Groenewald *et al.* (1995) and Board *et al.* (2005)]. Sample locations are marked by numbers 14, 15, and 16, which indicate the localities of samples Z7-14-5, Z7-15-2 and Z7-15-5, and Z7-16-4, respectively.

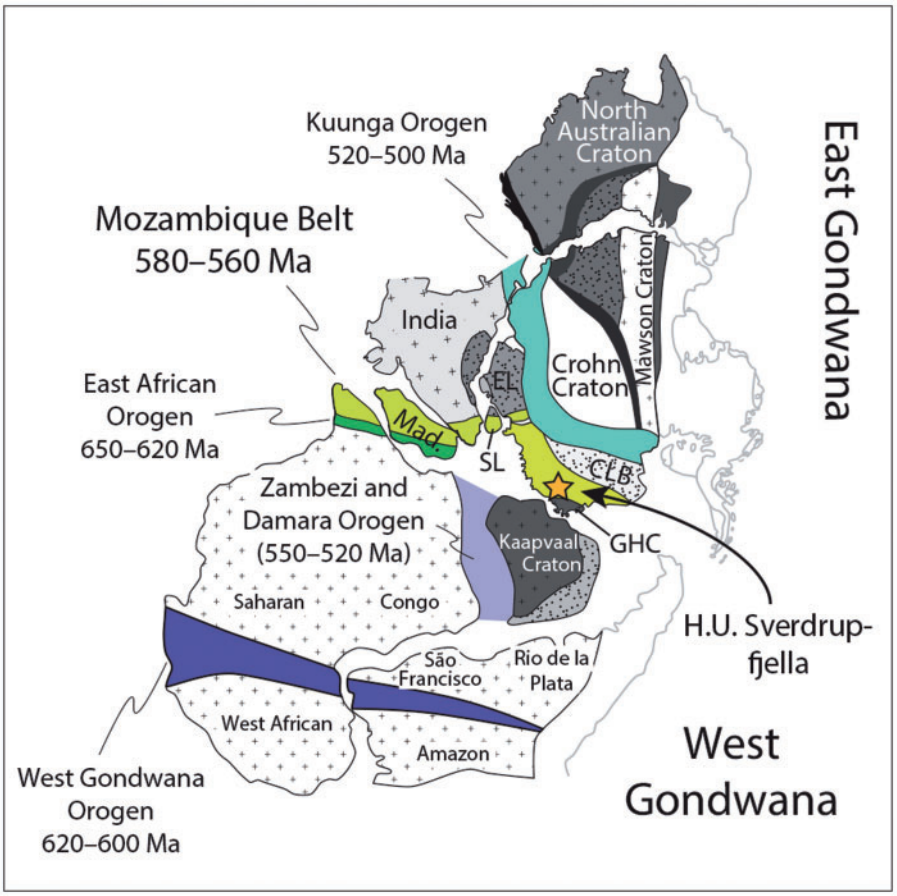

Fig. 2. Palaeogeographical reconstruction of Gondwana [modified after Boger (2011)] indicating the position of the H.U. Sverdrupfjella. Most of Dronning Maud Land is interpreted as part of the Kalahari Craton (which also includes the Kaapvaal Craton) and was, therefore, part of West Gondwana prior to Gondwana amalgamation. The Coats Land Block (CLB), the Prydz Bay area and Enderby Land (EL) are interpreted as part of greater India in East Gondwana. Several consecutive stages of Pan-African collision led to formation of Gondwana between 650 and 500 Ma. The 580–560 Ma Mozambique Belt extends from Somalia to Madagascar (Mad), southern India and Sri Lanka (SL) to DML, and includes the H.U. Sverdrupfjella. Cratons and Precambrian landmasses are distinguished by patterned fills. GHC, Grunehogna Craton.

amphibolite-facies metamorphic rocks of western H.U. Sverdrupfjella from unmetamorphosed to lower-greenschist-facies metamorphic sediments of the Ritscherflya Supergroup (e.g. Wolmarans & Kent, 1982; Marschall *et al.*, 2013*b*; Grosch *et al.*, 2015). This puts the samples investigated in this study close (60–100 km) to the western front of Neoproterozoic orogenesis. The eastern limit of the orogen in Antarctica is much more difficult to locate, because of the scarcity of outcrops further inland. It may be located at the Forster Magnetic Anomaly, ~175 km SE of our sample locality, or it may lie ~750 km to the east at a line connecting the Shackleton Range with Lützow–Holmbukta (e.g. Jacobs *et al.*, 1998; Shiraishi *et al.*, 2008; Will *et al.*, 2010; Riedel *et al.*, 2013).

The H.U. Sverdrupfjella has been subdivided into three major lithological units, which were probably deposited in the late Mesoproterozoic (*c.* 1130 Ma) in a continental arc setting at the southeastern margin of the Kalahari–Grunehogna Craton (Groenewald *et al.*, 1995; Harris *et al.*, 1995; Frimmel, 2004; Grosch *et al.*, 2007; Grantham *et al.*, 2011). The lowest unit is the Jutulrøra Formation, consisting of a volcanic arc sequence of metamorphosed interlayered mafic and felsic calc-alkaline volcanic rocks and clastic sedimentary rocks (Groenewald *et al.*, 1995; Grantham *et al.*, 2011). The sequence is dominated by intercalated tonalitic orthogneisses and hornblende–biotite gneisses that were metamorphosed at upper-amphibolite-facies conditions during the Neoproterozoic orogeny (Groenewald *et al.*, 1995; Grantham *et al.*, 2011; Grosch *et al.*, 2015). The Fuglefjellet Formation is the structurally overlying unit and is dominated by marble and compositionally layered, and in some places migmatitic, biotite–hornblende gneiss (Grantham *et al.*, 1995; Board *et al.*, 2005). The Fuglefjellet Formation is overlain by the Rootshorga Formation. The contact between these two units was initially interpreted as a major thrust fault (Groenewald *et al.*, 1995), but reports from more recent fieldwork have described a gradational transition between the two formations and interpreted it as a change in sedimentary protolith composition (Board *et al.*, 2005).

The Rootshorga Formation dominates the eastern outcrops of H.U. Sverdrupfjella (Grantham *et al.*, 1995;

Board *et al.*, 2005). A pelitic to semipelitic garnet–biotite paragneiss containing sillimanite or kyanite and subordinate boudinaged mafic lenses and calc-silicate enclaves constitutes the Rootshorga Formation. Late Mesoproterozoic sheet-like granites intrude the unit. They occur as megacrystic orthogneisses throughout the area with intrusion ages between 1100 and 1070 Ma and subsequent Mesoproterozoic metamorphism at 1050–1030 Ma (Grantham *et al.*, 1995; Harris *et al.*, 1995; Board *et al.*, 2005).

Previous studies have documented high-grade metamorphic assemblages in the H.U. Sverdrupfjella ranging from upper amphibolite to granulite facies (Groenewald & Hunter, 1991; Grantham *et al.*, 1995; Moyes & Groenewald, 1996; Board *et al.*, 2005). It has been suggested that the Jutulrøra Formation in the western H.U. Sverdrupfjella was metamorphosed at slightly lower metamorphic conditions (amphibolite facies) compared with the granulite-facies Rootshorga Formation in the eastern part, and that the eastern Rootshorga Formation was thrust over the western Fuglefjellet and Jutulrøra formations (Grantham *et al.*, 1995; Groenewald *et al.*, 1995). However, the identity of the thrust faults and the differences in metamorphic grades have been questioned by other workers and a continuous crustal section with >10 km apparent thickness was proposed instead (Board *et al.*, 2005).

The timing of metamorphism in the different parts of the Maud Belt in general, and in the H.U. Sverdrupfjella in particular, is not well constrained, despite a relatively large number of geochronology studies. Initially it was argued that folding, penetrative deformation and granulite-facies metamorphism were restricted to late Mesoproterozoic events related to Rodinia assembly at *c.* 1050 Ma, and that the Pan-African orogeny caused only reheating of the metamorphic sequence (Moyes *et al.*, 1993*a*; Groenewald *et al.*, 1995). However, it has been demonstrated subsequently that the Neoproterozoic event caused intense deformation, folding and metamorphic recrystallization at upper amphibolite-facies conditions (Board *et al.*, 2005). Zircon U–Pb ages of both orogenic events are preserved throughout the Maud Belt, but it is unclear which of the observed high-grade mineral assemblages were formed or equilibrated during the Mesoproterozoic orogeny or the Pan-African orogeny. Previous allocations of *P–T* conditions or paths to one event or the other have to be viewed with caution in cases where geochronological data have not been directly linked with petrographic evidence. This has been recognized before and *P–T* estimates have been published with question marks regarding their allocation to one of the two major orogenic events (e.g. Board *et al.*, 2005).

Decameter-sized boudins of metabasic rocks are embedded in the Rootshorga paragneiss, which have been interpreted as retrogressed eclogites and taken as evidence for subduction prior to the onset of Neoproterozoic collision (Groenewald *et al.*, 1995). The importance of these rocks for the tectonic interpretation of DML demanded that one of these 'eclogite' lenses was re-sampled and investigated in more detail in the study presented here.

Cambrian to Ordovician granite intrusions, as well as numerous undeformed granitic dykes, occur throughout the H.U. Sverdrupfjella. These include the Dalmatian granite, a two-mica S-type granite, intruded at *c.* 470 Ma (Grantham *et al.*, 1991) and the large Brattskarvet intrusive complex. The Brattskarvet Suite is a plutonic complex of alkaline A2-type monzonitic, syenitic to granitic composition that intruded the Rootshorga gneisses in the northernmost H.U. Sverdrupfjella (Fig. 1b). The intrusive contacts of the pluton with its country-rock are well exposed and large blocks of country-rock within the granitoids are exposed in the ~11 km × 6 km outcrop area of the pluton. The age of intrusion of the Brattskarvet complex is not well defined. It is post-tectonic with respect to the penetrative deformation events identified in the surrounding gneisses, and thus has to be late in the Pan-African orogenic cycle. Moyes *et al.* (1993*b*) estimated the emplacement age at 519 ± 15 Ma based on Rb/Sr and Sm/Nd whole-rock data, whereas an age of 489 ± 10 Ma (C. Jackson, unpublished data) was reported by Bisnath & Frimmel (2005). The last magmatic activity in the area is related to the Jurassic break-up of Gondwana, which produced syenite plutons and basaltic dykes in the Jutulstraumen rift zone at Straumsvola and Tvora (Harris & Grantham, 1993; Grantham, 1996; Riley *et al.*, 2009; Fig. 1b).

SAMPLES

The samples were collected during the British Antarctic Survey 2007–2008 field campaign in Dronning Maud Land by a two-man party (H.R.M. and field assistant S. Tamm). All samples investigated in this study were taken from the Rootshorga Formation and from the Brattskarvet intrusion (Figs 1b and 3a, b). Based on thin section studies, two granulite-facies samples were selected to be studied in detail (samples Z7-14-5 and Z7-15-2; Fig. 3d and e) along with a sample of the Rootshorga paragneiss (sample Z7-15-5; Fig. 3c and f) and a granite sample of the Brattskarvet intrusion (sample Z7-16-4; Fig. 3a and b; Tables 1 and 2). Sample Z7-15-2 was taken from a mafic boudin, 20 m in diameter, embedded within the Rootshorga paragneiss at the northern contact of the Brattskarvet intrusion (Figs 1b and 3d). The locality is identical to the northernmost 'eclogite' locality described by Groenewald *et al.* (1995) (Fig. 1b). Sample Z7-14-5 represents part of a large angular block (or xenolith; 30 m × 8 m) composed of intermediate (biotite-rich) and garnet-bearing felsic gneiss within the Brattskarvet intrusion (Fig. 3e). The contact between the block and the granite is sharp and does not show any obvious alteration in the contact region. The distance between the two samples is 4·3 km (Fig. 1b).

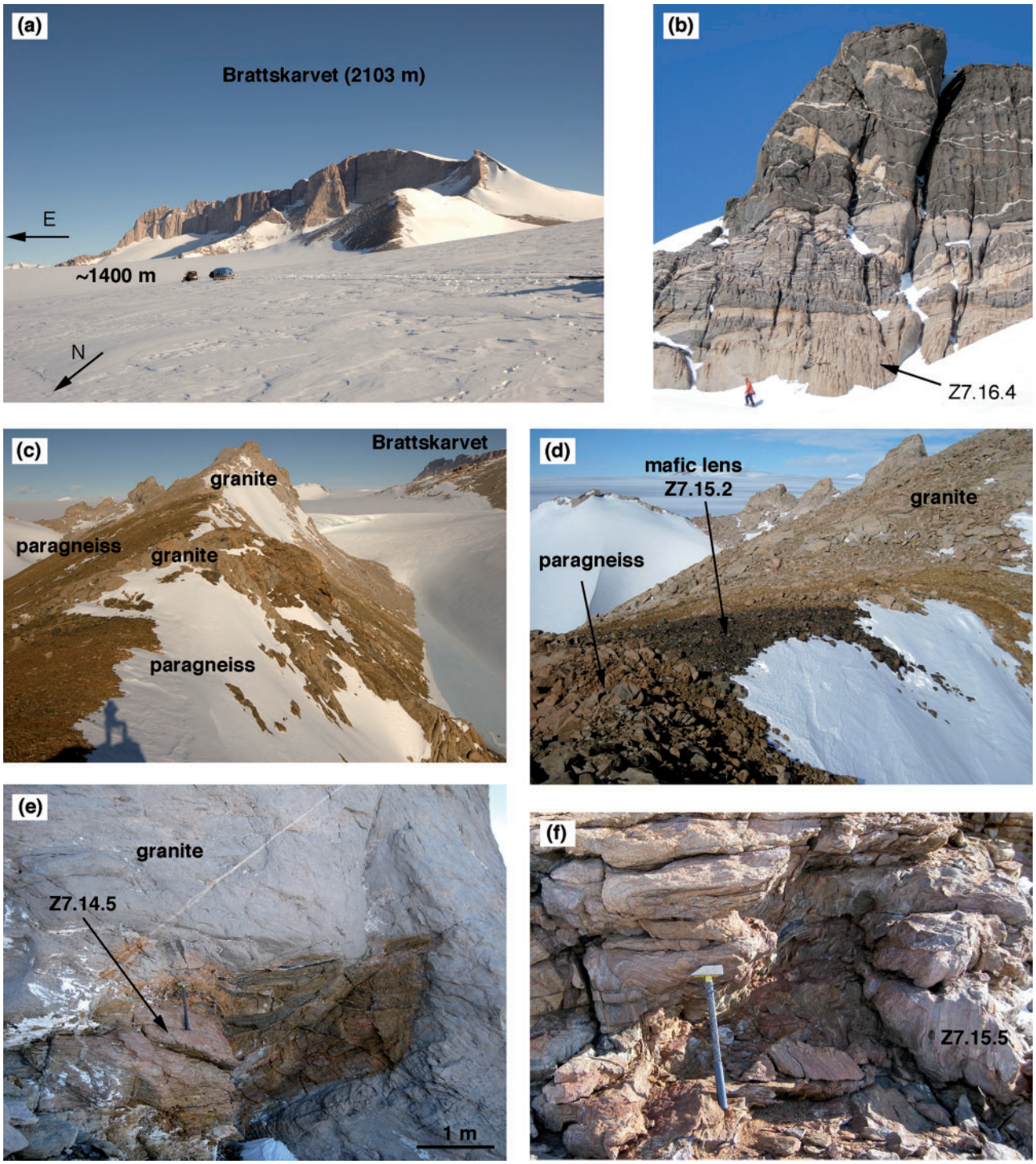

Fig. 3. Field images showing the study area in the northern H.U. Sverdrupfjella. (a) The Brattskarvet intrusive complex is best exposed along its several hundreds of meters high north-facing wall. (b) The Brattskarvet complex is composed of various layers of monzonite, melano-syenite, quartz syenite and granite, and is crosscut by aplite and pegmatite dykes. (c) The contact between intrusion and country rock paragneiss of the Rootshorga Formation is well exposed in some places. (d) Amphibolized mafic garnet granulite sample Z7-15-2 was taken from a mafic boudin embedded in the reddish-brown paragneiss of the Rootshorga Formation in the vicinity of the intrusive contact with the beige granite. (e) Felsic granulite sample Z7-14-5 was taken from a large xenolithic block within the Brattskarvet granite. (f) Sample Z7-15-5 was taken from the paragneiss of the Rootshorga Formation that forms the country rock to the boudin of amphibolized mafic garnet granulite and to the Brattskarvet intrusive complex. It shows several generations of foliation and folding.

Table 1: List of samples investigated in this study

Name	Rock type	Locality	Latitude (S)	Longitude (E)	Peak assemblage	Retrograde phases
Z7-14-5	felsic granulite	Brattskarvet	72°05·830′	001°22·955′	Grt, Afs, Atp, Ky, Qz, Rt, Zrn, Mnz	Ilm, Bt, Sil, Crd/pinite, Ms
Z7-15-2	mafic amphibolite	Beacon Ridge	72°03·862′	001°19·415′	Grt, Cpx(?), Pl-I, Rt, Qz, Zrn	Opx, Mag, Ilm, Hbl, Cum, Pl-II, Ser, Py
Z7-15-5	paragneiss	Beacon Ridge	72°03·909′	001°18·780′	Pl, Afs, Qz, Bt, Zrn, Py	Ms, myrmekite, Ser
Z7-16-4	granite	Brattskarvet	72°06·319′	001°28·783′	Afs, Pl, Qz, Cpx, Am, Bt, Zrn, Ttn, Aln, Ap	Chl, myrmekite, Ser

Mineral abbreviations after Whitney & Evans (2010): Afs, alkali feldspar; Aln, allanite; Ap, apatite; Atp, anti-perthite; Bt, biotite; Cpx, clinopyroxene; Cum, cummingtonite; Grt, garnet; Hbl, hornblende; Ilm, ilmenite; Ky, kyanite; Mag, magnetite; Mnz, monazite; Ms, muscovite; Opx, orthopyroxene; Py, pyrite; Qz, quartz; Rt, rutile; Sil, sillimanite; Ser, sericite; Zrn, zircon.

Table 2: Whole-rock composition of the felsic granulite (Z7-14-5), the mafic granulite (Z7-15-2) and the Brattsakrvet granite (Z7-16-4)

Sample	Z7-14-5	Z7-15-2	Z7-16-4
SiO_2	73·32	51·46	68·94
TiO_2	0·18	1·95	0·34
Al_2O_3	13·96	13·45	15·22
Fe_2O_3*	1·41	16·50	2·58
MnO	0·01	0·23	0·04
MgO	0·35	7·03	0·46
CaO	1·26	6·82	1·58
Na_2O	2·91	0·55	4·35
K_2O	4·97	1·64	5·36
P_2O_5	0·07	0·15	0·12
Sr (μg g^{-1})	610	110	1580
Zr (μg g^{-1})	95	100	310
Ba (μg g^{-1})	1100	445	2830
LOI	0·72	1·49	0·45
Total	99·37	101·27	99·76

Element analyses are oxide wt % unless otherwise stated. LOI, loss on ignition.
*Total Fe given as Fe_2O_3.

Felsic granulite Z7-14-5

The sample is a felsic gneiss (composition given in Table 2) primarily composed of large garnet grains (up to 6 mm; 4%), two feldspars (perthite and antiperthite; 60%), quartz (34%) and angular aggregates of fibrolitic sillimanite (1·5%). Accessory minerals are rutile, monazite, zircon and apatite.

The rock shows layering defined by dark, millimeter-thick layers enriched in sillimanite aggregates and small garnet grains (≤0·5 mm diameter) that are partly replaced by pinite and biotite coronas, as well as near-complete replacement of matrix rutile by ilmenite (Fig. 4a–c). These darker layers are separated by centimeter- to decimeter-thick quartz–feldspar-rich leucocratic layers that contain larger garnet grains (≤6 mm) and rutile prisms (≤0·8 mm in length) that are visible in hand specimen (Fig. 4a). Some garnet grains show fracturing and fragmentation. A moderately strong foliation parallel to the layers is defined by disc-like quartz and by the orientation of the sillimanite aggregates, rutile prisms, and elongated garnet fragments (Fig. 4a and b).

In thin section, garnet is light pink and most grains show a narrow corona structure (Fig. 4b and c) of pinite and/or symplectitic biotite + quartz ± muscovite. Rutile inclusions are abundant in garnet cores and rims, and many inclusions are composed of several minerals, such as combinations of rutile with ilmenite, zircon, quartz, and/or Zn-rich hercynite. Some rutile inclusions are connected to the grain matrix through cracks in the garnet host and show the formation of Ti-rich biotite at the rutile–garnet interface. Many other inclusions, however, are apparently well concealed by their host and show neither cracks nor signs of retrogression. Apatite, zircon, monazite and ilmenite inclusions were also observed.

Perthite and antiperthite, as well as microcline and plagioclase are present. The fibrolitic sillimanite forms angular aggregates that are probably pseudomorphs after kyanite (Fig. 4b and c). No relic kyanite was observed in the thin sections.

The dominant Ti-mineral is rutile, which occurs as prismatic grains in many places (typically 500 μm in the long dimension; Fig. 4a and b). It occurs in the matrix and as inclusions in garnet. Ilmenite is the dominant Ti mineral in the dark layers of the rock (Fig. 4c) and occurs as inclusions in garnet, either in combination with rutile or (more rarely) as isolated inclusions.

Brown biotite is part of the symplectitic coronae around garnet and occurs as coarse, as well as symplectitic grains in contact with garnet and sillimanite. In the latter case it is accompanied by muscovite. Muscovite occurs as coarse grains in a paragenesis with biotite next to garnet and sillimanite, and as a symplectite together with biotite and quartz in garnet coronae.

Amphibolized mafic garnet granulite Z7-15-2

This rock is a fine-grained (<1 mm) metabasite (Table 2) that is mainly composed of two amphiboles (50%), orthopyroxene (10%), plagioclase (25%, of which ~50% is sericitized), quartz (10%), opaque minerals (5%), rutile and accessory apatite and zircon. The opaque minerals are ilmenite and magnetite (which are associated with rare Zn-rich spinel), as well as sulphides (pyrite and chalcopyrite). Part of the rock is composed of quartz and garnet relics, plagioclase–orthopyroxene symplectites surrounding garnet, and angular aggregates of quartz–plagioclase symplectites (Fig. 4d). However, irregular domains and layers show partial or complete replacement of orthopyroxene and garnet by subhedral to euhedral amphibole (Fig. 4e and f). In domains where

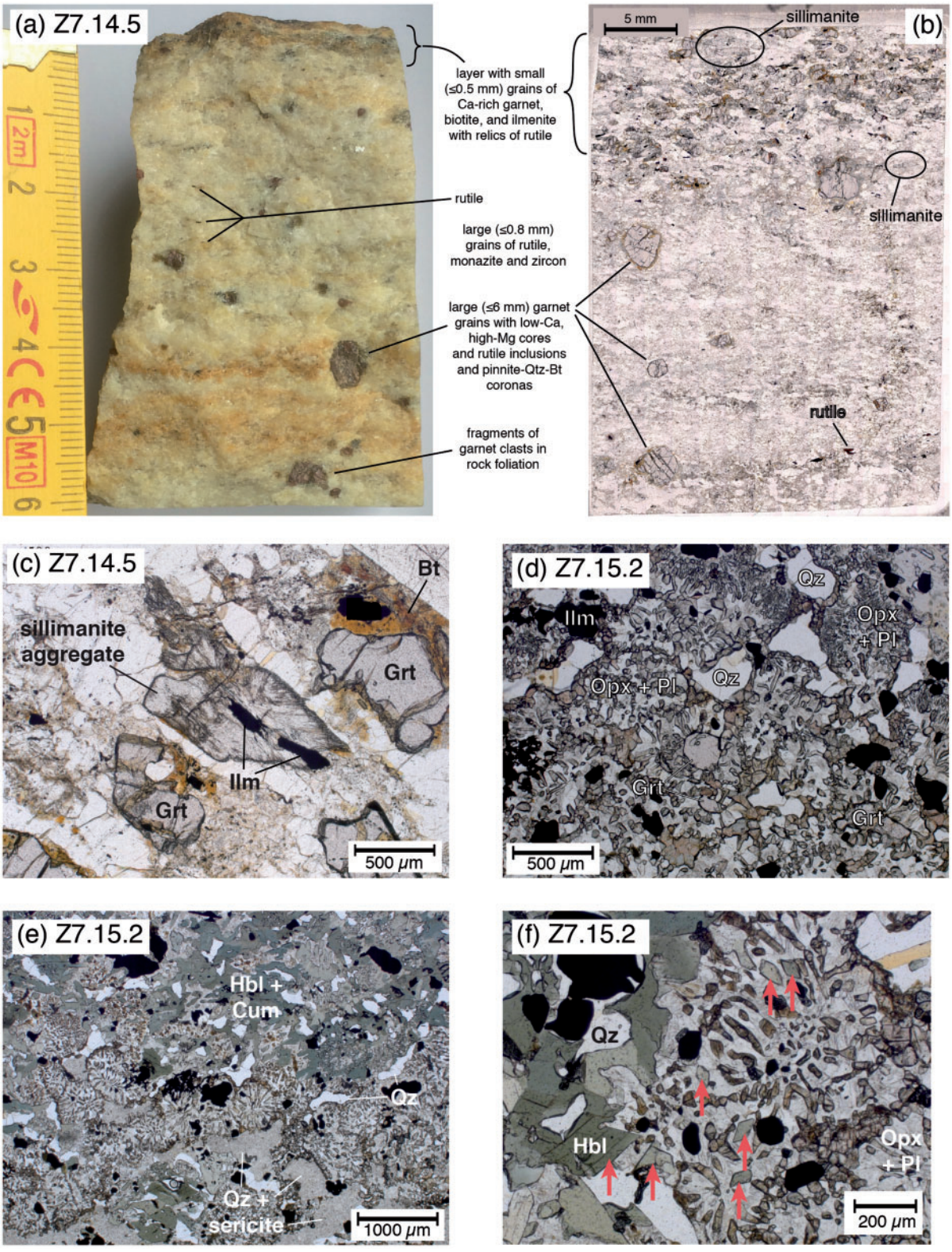

Fig. 4. (a) Hand specimen of felsic granulite sample Z7-14-5 showing garnet porphyroclasts and prismatic rutile grains in the quartz–feldspar-rich, foliated rock mass, as well as thin darker layers that are more fine-grained and contain more biotite and ilmenite. (b) Plane-polarized light (PPL) photomicrograph of a full thin section of sample Z7-14-5 showing layering and foliation, as well as garnet grain-size variation and large, prismatic rutile grains. (c) Thin-section PPL photomicrograph of felsic granulite Z7-14-5 showing small, subhedral garnet grains enclosed in a corona of cordierite (pinite), biotite and ilmenite, and angular aggregate of fibrous sillimanite. (d–f) Thin-section PPL photomicrographs of amphibolized mafic garnet granulite Z7-15-2 at different magnifications. (d) Relic garnet grains and quartz separated by orthopyroxene–plagioclase symplectite. The opaque minerals are ilmenite and minor magnetite. (e) Transition from an amphibole-free domain of the rock to a domain dominated by coarse-grained green hornblende, colourless cummingtonite and quartz. The amphibole-free domain consists of orthopyroxene–plagioclase symplectites, quartz, and angular aggregates of symplectites of quartz and (partly) sericitized An-rich plagioclase. (f) Euhedral amphibole (red arrows) occurs at the edges and within the orthopyroxene–plagioclase symplectites.

amphibole growth is most advanced, orthopyroxene relics are replaced by cummingtonite and biotite, the latter being recognizable by pleochroism from pale pink to brown (Fig. 4f). Ilmenite and magnetite occur in the anhydrous domains and in the amphibole-rich domains, whereas the sulphides are restricted to the amphibole-bearing domains.

Weakly pink garnet relics (up to 300 μm diameter) show a corona structure with symplectitic orthopyroxene + plagioclase ± ilmenite ± magnetite (Fig. 4d). Most of the symplectites do not contain garnet relics though, which is probably due to cutting effects and to complete resorption of many garnet grains (Fig. 4d and e). No relics of clinopyroxene were observed in this rock.

The most abundant amphibole is green hornblende, which contains exsolution lamellae of cummingtonite that are less than 1 μm wide. This low-Al amphibole also occurs as tens of micrometers wide zones at the rims of hornblende and as separate coarser grains (≤100 μm diameter). Cummingtonite also occurs as a pseudomorph after orthopyroxene.

Two textural varieties of plagioclase are present. One occurs as part of the symplectite around garnet and the other as large subhedral grains (several hundred micrometers in the long dimension; Fig. 4e). Sericitization is very advanced and has led to the commonly observed symplectites of sericite + quartz ± magnetite, surrounded by orthopyroxene (Fig. 4e).

Rootshorga paragneiss sample Z7-15-5

Sample Z7-15-5 was taken from the country rock of the Brattskarvet intrusion at a distance of ~50 m from the intrusive contact. The gneiss is layered with biotite-rich and quartz–feldspar-rich layers and is strongly folded (Fig. 3f). The sample is a coarse-grained (millimeter-sized grains), recrystallized gneiss showing biotite-rich layers (~50% biotite) and layers rich in quartz, plagioclase (partly sericitized) and alkali feldspar (showing microcline twinning). Subordinate muscovite forms large grains around biotite. Larger pyrite grains are partly replaced by Fe-oxi-hydroxides. No garnet, sillimanite or kyanite was observed and consequently no *P–T* estimates were attempted for this sample. Instead, zircon was separated from this sample to supplement the geochronological information extracted from granulite samples Z7-14-5 and Z7-15-2. The extracted zircon grains show a large range of shapes and internal zoning patterns, from long-prismatic with oscillatory zonation, to large isometric grains with sector zoning ('soccer-ball zircon'), which are typical for granulites. Many grains are larger than 300 μm in the longest dimension.

Brattskarvet granite sample Z7-16-4

One sample from the layered Brattskarvet intrusive complex (Fig. 3a and b) was used in this study to determine the intrusion age of the plutonic suite. The sample is a medium-grained (2–3 mm average grain size), alkali-rich granite (69% SiO_2, 10% $K_2O + Na_2O$; Table 2). It consists mainly of alkali feldspar (microcline twinning), plagioclase, quartz and <5% mafic minerals, as well as abundant accessory zircon, apatite, allanite, magnetite and titanite. The dominant mafic minerals are pale green clinopyroxene and dark green amphibole. Chloritization of the subordinate biotite and sericitization of plagioclase is limited. Alkali feldspar shows perthite exsolution. The weak anisotropy is defined by the parallel alignment of the mafic minerals. No evidence of sub-solidus deformation was observed, except for minor undulose extinction of quartz. Zircon in this sample is mostly short-prismatic (~200 μm long) with oscillatory zonation. Many grains show rim zones with a nebulous or patchy internal zonation that replaced the oscillatory zones along irregular boundaries.

ANALYTICAL METHODS

Whole-rock X-ray fluorescence (XRF) analyses were performed at Universität Heidelberg using a Rh-tube equipped Siemens® SRS303 instrument. Major and minor elements were measured on fused glass discs and trace elements were determined on pressed pellets. The operating conditions were 60 kV and 50 mA for the heavier elements and 30 kV and 99 mA for the lighter elements. The accuracy is reflected by the reproducibility of international standards measured for control purposes, and ranges from 0·5–1% for major elements to 5–10% for trace elements.

A Cameca® SX51 electron probe micro-analyser (EPMA) equipped with five wavelength-dispersive spectrometers was used to determine mineral compositions (Institut für Geowissenschaften, Universität Heidelberg). Operating conditions were 20 nA beam current and 15 kV acceleration voltage. Feldspar was analysed with a defocused beam of 10 μm to avoid loss of alkalis. Counting times were 10 s for Na and K, and 20 s for all the other elements. Natural and synthetic silicate and oxide international standards were used for calibration.

Compositions of garnet in felsic granulite sample Z7-14-5 were analysed using a JEOL® JXA-8200 Superprobe EPMA at the Massachusetts Institute of Technology (MIT), Cambridge, USA. An acceleration voltage of 15 kV and a beam current of 10 nA was employed. An almandine-rich garnet mineral reference material (Harvard almandine #112140; McGuire *et al.*, 1992) was used to calibrate the Superprobe for SiO_2 (38·4%), Al_2O_3 (22·5%), FeO (26·51%), MnO (2·19%), MgO (8·34%), CaO (1·73%) and Na_2O (0·12%) for garnet analyses in sample Z7-14-5. Counting times were 40 s and 20 s on peaks and backgrounds, respectively. Typical 1σ relative standard deviation of counts were 0·3–0·4% for Si, Al, and Fe, 0·7% for Mg, 1·7% for Ca, and 3–6% for Mn, Ti, Cr, Na, and K. Detection limits were between 0·009 and 0·032% for all analysed oxides.

Rutile was also analysed using the JEOL® JXA-8200 at MIT. The accelerating voltage was 15 kV and the beam current was 100 nA. Peak counting times were 300 s for

Nb and Zr, 200 s for Si, 170 s for Mg and Al, 70 s for Cr and Ca, 40 s for Ti and Fe, and 340 s for W. Background counting times were half of the peak counting times. Typical 1σ standard deviation of counts for the elements Zr, Nb, Al, Ca, and W were 4–5% at 500 μg g^{-1} concentration and 2·0–2·5% at 1000 μg g^{-1}. Cr and Fe show a slightly larger uncertainty of ~10% at 500 μg g^{-1}, 4–5% at 1000 μg g^{-1} and 0·7% at 10 000 μg g^{-1}. Counting precision for Si was ~8% at 100 μg g^{-1} and ~2% at 300 μg g^{-1} concentration. The error on Zr-in-rutile thermometry introduced by Zr counting precision is ±4°C at 500 μg g^{-1} and ±2·5°C at 1000 μg g^{-1}. Detection limits were 25–33 μg g^{-1} for Zr, Nb, Al, Ca, and W, 50 μg g^{-1} for Fe, 65 μg g^{-1} for Cr and Ti, 20 μg g^{-1} for Mg and 15 μg g^{-1} for Si. Natural and synthetic silicate and oxide international standards were used for calibration. Nb and W were calibrated using pure metals, and Zr was calibrated using natural zircon.

Elemental X-ray maps and chemical compositions of monazite were also obtained on the JEOL® JXA-8200 at MIT. Back-scattered electron images were also obtained with the same instrument. Monazite was analysed with an accelerating voltage of 15 kV and a beam current of 100 nA. The counting times were 200 s for Pb, 100 s for U, 60 s for Si, Ca, and Y, 20 s for Th, and 15–20 s for Fe, P, and rare earth elements (REE). Typical 1σ standard deviation of counts were 0·3% for P and Ce, 0·4–1·0% for Ca, La, Th, and Nd, 1–3% for Si, Y, and Pb, 3–6% for Pr, Gd, and U, 7–14% for Dy, Ho, and S, and 16–25% for Sm, Er, and Lu. The details of X-ray peak and background measurement, and interference correction, are the same as given by Chatterjee *et al.* (2010). The raw data were corrected for matrix effects with the program CITZAF (Armstrong, 1995) and the weighted-mean ages were calculated with the program ISOPLOT (Ludwig, 2003, 2008).

A Horiba® LabRAM HR Evolution confocal μ-Raman system equipped with three lasers of different wavelength was used for mineral identification on a micro- to submicrometer scale (Woods Hole Oceanographic Institution). The relevant measurements were performed with a 632 nm laser.

Cathodoluminescence (CL) imaging with a CL detector attached to a JEOL® JXA-733 Superprobe EPMA at MIT was employed to reveal intra-grain zoning patterns in zircon.

Zircon was dated at the Northeast National Ion Microprobe Facility (NENIMF) at the Woods Hole Oceanographic Institution by secondary ion mass spectrometry (SIMS) using a Cameca® IMS 1280 system. Analytical procedures were similar to those described by Schuhmacher *et al.* (1994). A 4–6 nA, 12·5 kV mass filtered $^{16}O^{2-}$ primary beam was focused to an ~30 μm (long axis) elliptical spot. A mass resolution of 6700 was applied as well as oxygen flooding to enhance the Pb ion yield. A rastered 180 s pre-sputtering was set prior to the 16 measuring cycles that included the following species: $^{90}Zr_2{}^{16}O^+$, $^{180}Hf^{16}O^+$, $^{204}Pb^+$, $^{206}Pb^+$, $^{207}Pb^+$, $^{208}Pb^+$, $^{90}Zr_2{}^{16}O_2{}^+$, $^{238}U^+$, $^{232}Th^{16}O^+$, $^{238}U^{16}O^+$, $^{238}U^{16}O_2{}^+$. The zircon standard 91500 was used for U/Pb calibration purposes, which has $^{206}Pb/^{238}U = 0{\cdot}17917$ (the accepted $^{207}Pb/^{206}Pb$ age is 1065·4 ± 0·3 Ma; Wiedenbeck *et al.*, 1995). The lead–lead ages of standard 91500 were consistent during the entire session and result in a pooled age of 1065·2 ± 7·2 Ma (95% confidence limit; Supplementary Data Table and Figs S6 and S7; Supplementary Data are available for downloading at http://www.petrology.oxfordjournals.org). The zircon Temora-2 (Black *et al.*, 2004) was analysed as a reference standard. The published $^{206}Pb/^{238}U$ age for this zircon standard is 416·78 ± 0·33 Ma (Black *et al.*, 2004) and agrees with the $^{206}Pb/^{238}U$–$^{207}Pb/^{235}U$ concordia age of 416·7 ± 5·4 Ma obtained by the ion microprobe during our session (Supplementary Data Table and Fig. S8). Contributions of common Pb were monitored by measuring ^{204}Pb and subsequently corrected for using present-day common Pb [Pb evolution model of Stacey & Kramers (1975)]. The common lead fraction was typically below 0·2%. Data reduction was done according to the procedures described by Williams (1998). A correction for instrumental mass fractionation of 2‰ per a.m.u. was applied for the Pb isotopes. Uncertainty on this correction is included in the calculation of errors on the U/Pb and Pb/Pb ratios. Corrections for minor changes in beam density or energy were made based on the comparison of U/Pb with $UO_2{}^+/UO^+$ ratios. Data were processed off-line using a MatLab-based in-house data reduction routine. Plots and age calculations were made using the program ISOPLOT (Ludwig, 2003, 2008).

The ion probe at Woods Hole was also used to determine Ti concentrations in zircon. The calibration was done using 91500, Temora-2 and FC1 as natural standards with Ti concentrations of 6·09 ± 0·74, 9·1 ± 0·6 and 21·9 ± 1·6 μg g^{-1}, respectively (Yuan *et al.*, 2004; Hiess *et al.*, 2008). ^{48}Ti, ^{96}Zr and ^{30}Si were measured with a 4·5 nA O^{2-} beam. A mass resolution of 10 000 was used to resolve the ^{48}Ti and $^{96}Zr^{2+}$peaks. Isobaric interferences from ^{48}Ca can be neglected because of its low abundance and the overall low concentrations of Ca in zircon. Calibration data are given in the Supplementary Data.

RESULTS

Mineral chemistry

Felsic granulite Z7-14-5

The composition and chemical zonation of garnet in this sample varies with grain size. The largest grains (up to 6 mm diameter in the longest dimension) show large, homogeneous core plateaux with high Mg contents and very low Ca contents (Fig. 5a), approximating $Prp_{30}Alm_{67}Grs_{2\cdot3}$. At a distance of ~600 μm from the grain edges, the Ca content shows a strong increase and reaches a maximum ~100 μm from the edge with grossular contents of >6%, beyond which the Ca contents drop to low levels close to the grain edges

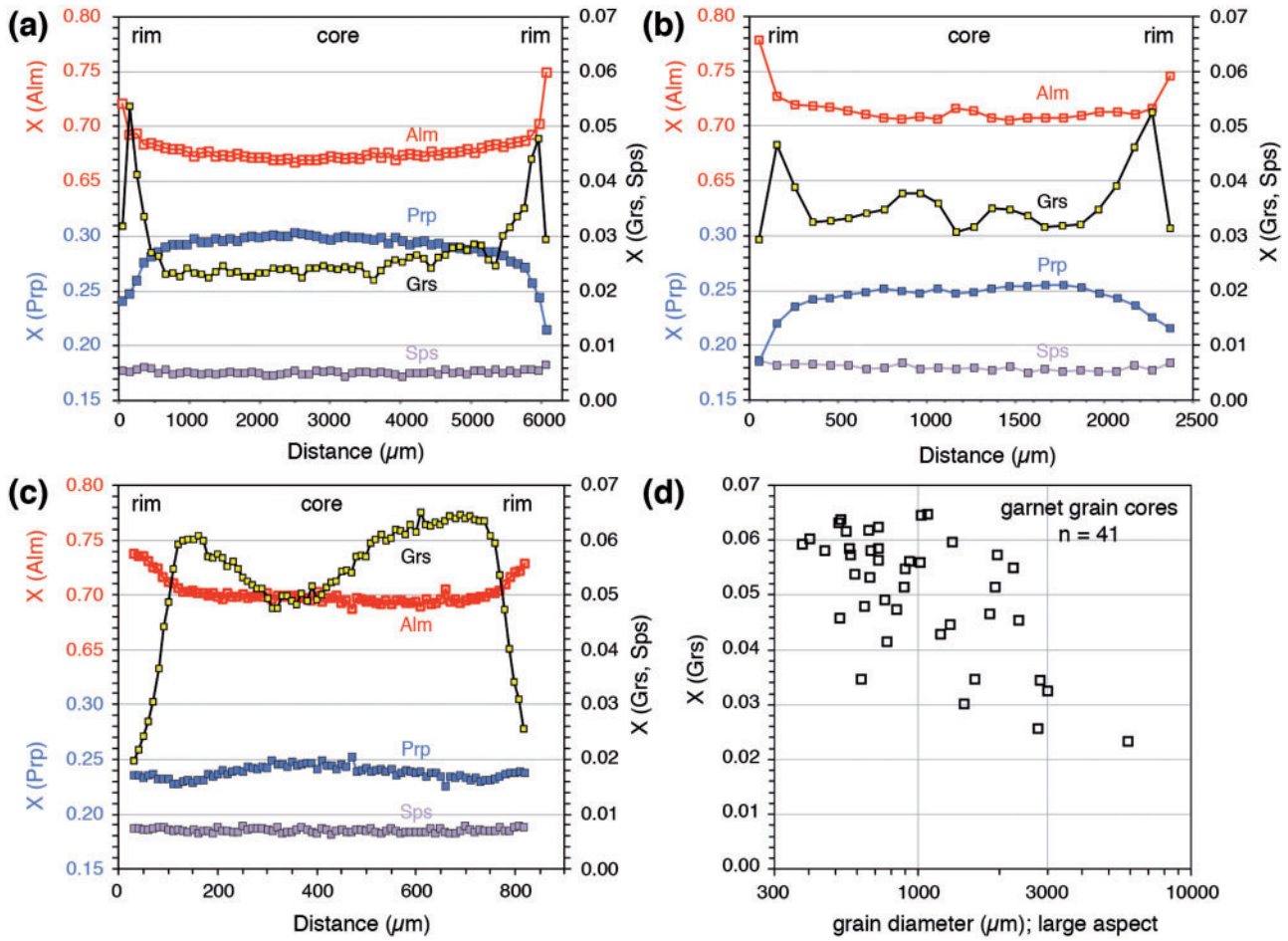

Fig. 5. (a–c) Across-grain compositional profiles of garnet grains of different diameter in felsic granulite sample Z7-14-5 (images of these grains are provided in Supplementary Data Fig. S9). The different *y*-axis scales refer to different components, but all data for a component are plotted on the same *y*-axis scale. (a) Large garnet grain (~6 mm diameter) with homogeneous core region with 30% pyrope and 2·3% grossular. More detailed profiles of Ca in the rim region are shown in Fig. 6. (b) Medium-sized garnet grain (~2·5 mm diameter) with lower pyrope (~25%) and higher grossular contents (~3·5%) in the core. (c) Small garnet grain (<1 mm diameter) with low pyrope (≤25%) and high grossular (≥5%) contents. All three grains show a strong increase of Ca at a distance of 100–200 μm from the grain edge and a decrease to very low Ca contents in the outermost 50 μm. (d) Grossular content of the cores of 41 garnet grains analysed in thin section plotted against their respective grain diameter as measured in thin section. The largest aspect is plotted in the case of non-isometrical grains. The lowest grossular contents are preserved in the largest grains, whereas the cores of small grains have high grossular contents. All data are given in the Supplementary Data tables.

(Figs 5a and 6). Mg contents show a simple decrease from the core plateaux to the grain edges in the outermost 1000 μm, compensated by an increase in Fe (Fig. 5a). Pyrope contents at the rim are between 20 and 25%. Smaller grains show qualitatively the same zoning patterns, but the grossular contents of the grain cores tend to be higher the smaller the grain diameter. For example, a medium-sized grain (2·5 mm diameter) shows a grossular content of ~3·5% in the core region, and an increase to >5% grossular at a distance of ~100 μm from the grain edge, beyond which the grossular content drops towards the grain edge (Fig. 5b). Small grains (<1 mm) do not show the low-Ca core plateaux, but still show slightly lower Ca contents in the core that increase to values >6% grossular at a distance of ~100 μm from the grain edge, beyond which Ca drops to very low contents at the edge (Fig. 5c). The highest Ca content observed in garnet from this sample is equivalent to 6·6% grossular (assuming all Fe to be divalent). The analyses of compositions of 41 garnet grains exposed in thin section reveals a broad negative correlation of grossular content and grain diameter (Fig. 5d), supporting the findings from single garnet zoning patterns described above.

Magnesium and Fe contents of the smaller grains show relatively homogeneous core plateaux, as do the large grains, but their Mg contents are distinctly lower at 23–25% pyrope. Most of the 41 analysed grains with diameters between 500 and 1000 μm show pyrope contents between 23 and 25%. The Mn content of all garnet grains is low (0·5–0·7% spessartine component) and reaches a maximum of 2% in a few analysed grains.

The trace element content of matrix rutile (complemented by large rutile grains from heavy-minerals separates) and rutile included in garnet was analysed to unravel the temperature history of this sample. Matrix

rutile shows a very restricted composition with regard to all elements, with a median of 970 ± 270 μg g^{-1} Zr (1SD; Table 3). In particular, 12 out of 67 analysed matrix rutile grains showed Zr concentrations below 800 μg g^{-1}; the remaining grains (82%) have Zr concentrations between 819 and 1256 μg g^{-1} with three narrow peaks in a probability density plot at 948, 1075 and 1151 μg g^{-1} (not shown). Concentrations of other trace elements in matrix rutile cluster at 1000 μg g^{-1} Nb, 1400 μg g^{-1} Fe, 1050 μg g^{-1} Cr, 200 μg g^{-1} Al, and Si and Ca below detection limit (Fig. 7; Table 3 and Supplementary Data table). Some matrix rutile grains show increased W contents, particularly along annealed cracks that show oscillatory W zonation with WO_3 concentrations of up to 1·65 wt % in the W-rich domains. These grains show very low Zr contents (100–200 μg g^{-1}). In most analysed grains, however, W contents were below detection limit (<26 μg g^{-1}).

Rutile inclusions in garnet occur in two groups; the first group are composite inclusions, where rutile coexists with ilmenite, biotite and/or zircon, and the second group comprises single-phase rutile inclusions or inclusions of rutile and minerals such as hercynite or quartz that do not contain significant Ti or Zr. Most rutile grains in the first group show relatively low Zr contents similar to matrix rutile and show more scatter in other trace elements (Fig. 7). Images of all rutile inclusions in garnet are provided in the Supplementary Data (Fig. S2).

Isolated rutile inclusions (second group), in contrast, show elevated Zr concentrations of up to 4204 μg g^{-1} (Table 3). Nb (median 540 μg g^{-1}) and Cr (520 μg g^{-1}, with many analyses below detection limit) contents are lower than in matrix rutile, whereas Fe, Ca and Si contents are higher (Fig. 7; Table 3). In particular, Fe shows a positive correlation with Zr content (Fig. 7c). Silicon contents also increase with increasing Zr, but they do not follow the vector expected for analyses contaminated by zircon inclusions (Fig. 7b). Observed Si contents of the high-Zr rutile are between 47 and 265 μg g^{-1} (Table 3). Fe contents reach concentrations of ~1·2 wt % and Ca contents reach ~450 μg g^{-1} (Table 3; one outlier). Aluminium contents are slightly elevated in the inclusions (200–450 μg g^{-1}) compared with the matrix rutile. More elevated Al contents were found in two analyses that may be contaminated by the garnet host and also show elevated Si and, in one case, Mg contents (Fig. 7; Supplementary Data table).

Key observations in this study are (1) the connection between the Zr content of rutile inclusions in garnet and their position in the garnet host, and (2) the connection between rutile (Zr) and the grossular content of the garnet host at the position of the respective rutile inclusion. Some of the composite rutile with ilmenite, biotite and/or zircon inclusions (first group described above) show Zr contents below those of the matrix rutile and these grains show no correlation with their garnet host compositions. However, the single-phase rutile inclusions (second group, including composite rutile + quartz,

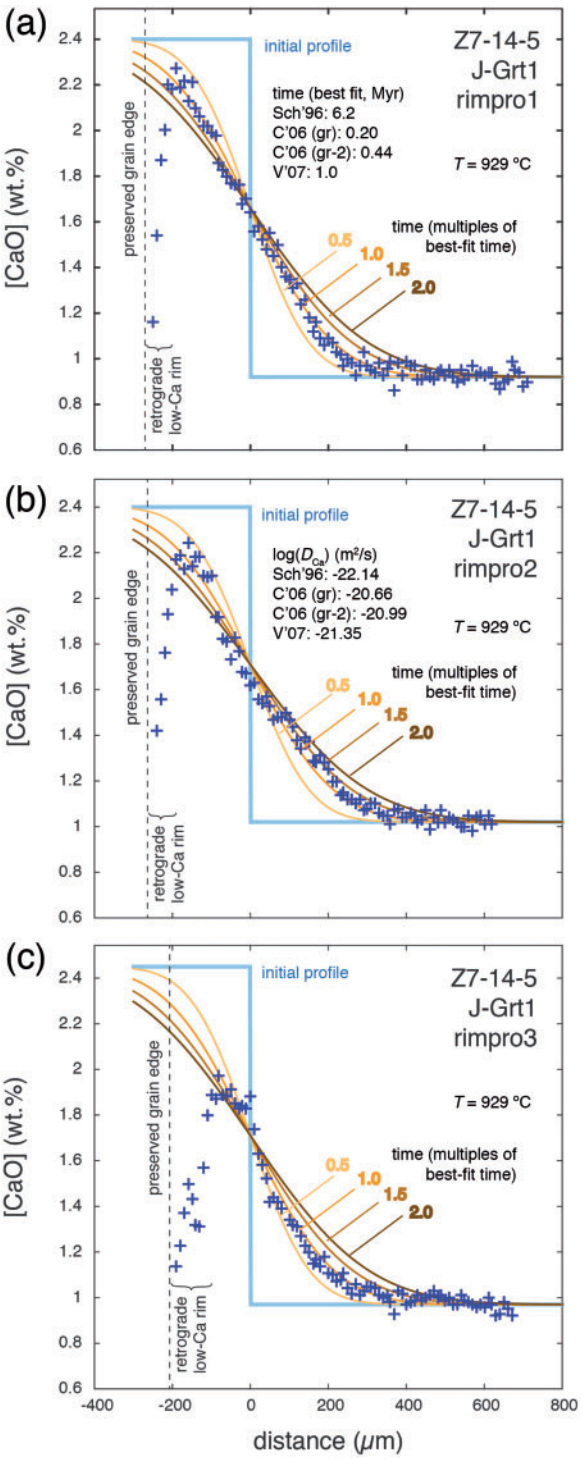

Fig. 6. Three detailed electron microprobe profiles (crosses; 10 μm spot distance) of the Ca zonation in the rim region of the large garnet grain shown in Fig. 5 and in the Supplementaty Data (Fig. S3). The curves display the results of diffusion modelling assuming an initial step function between low-Ca core and high-Ca rim and a one-dimensional semi-infinite diffusion model for a temperature of 929°C. The initial Ca content of the rim is the highest measured Ca in garnet from this sample. Diffusion coefficients: Sch'96, Schwandt *et al.* (1996); C'06, Carlson (2006) for fO_2 equal to the graphite–oxygen buffer (gr), and two log units below this buffer (gr – 2); V'07, Vielzeuf *et al.* (2007). The best-fit solution of *Dt* is plotted along with 0·5, 1·5 and 2·0 multiples of this solution in all three panels. It should be noted that all three profiles best fit the same model (i.e. the fit marked 1·0). Diffusion times in Myr given in (a) depend on the choice of the diffusion coefficient, given in (b).

Table 3: Minor and trace element content of rutile

Grain no.	Associated inclusions	Zr (μg g^{-1})	Nb (μg g^{-1})	Fe (μg g^{-1})	Cr (μg g^{-1})	Si (μg g^{-1})	*T* (°C)	*P* (GPa)	Grs (%) garnet	*d* (μm)
Sample Z7-14-5 (felsic granulite)										
Rutile inclusions in garnet not associated with zircon, biotite or ilmenite										
Rutile in low-Ca core region of garnet										
J-Grt1-Rt2	Qz	1448	541	3730	554	41	794	0·95	2·9	1362
J-Grt1-Rt3	Qz, Hc, Ap	1344	940	5306	470	48	786	0·95	3·3	1187
J-Grt1-Rt6		1290	503	11737	532	471	781	0·95	3·8	914
J-Grt1-Rt7	Hc	1348	602	11815	b.d.l.	90	786	0·95	2·9	1518
J-Grt1-Rt8		1316	600	11582	68	143	784	0·95	2·7	1482
Average							786 ± 9			
Rutile in low- to intermediate-Ca rim region of garnet										
J-Grt1-Rt9		4040	203	11271	b.d.l.	280	945	1·45	3·4	254
J-Grt1-Rt22		2028	81	9206	b.d.l.	54	857	1·45	2·8	539
J-Grt1-Rt15	Qz, Hc, Ap	2676	415	8665	b.d.l.	71	891	1·45	3·9	583
Very high-Ca garnet										
B-E10		1437	530	7102	758	56	818	1·45	5·2	—
B-F4		1854	1440	6987	606	90	847	1·45	5·4	—
H-Grt39	Qz	1804	933	5106	646	94	843	1·45	5·3	148
J-Grt1-Rt19	Qz	2157	1955	5042	b.d.l.	b.d.l.	864	1·45	5·4	176
J-Grt1-Rt20	Sil	2282	1239	8246	149	37	871	1·45	6·6	117
J-Grt1-Rt21		1481	1269	11115	160	67	821	1·45	6·3	32
Average							844 ± 44			
High-Ca garnet										
D-A3-s		3440	347	9533	640	117	923	1·45	4·0	—
D-A2-vs		3268	698	9976	473	265	917	1·45	4·2	—
D-A2-r		3798	345	8309	791	100	937	1·45	4·2	—
J-Grt1-Rt5		3371	220	10805	517	153	921	1·45	4·4	261
J-Grt1-Rt10	Qz, Hc	3514	317	11660	b.d.l.	87	926	1·45	4·5	224
J-Grt1-Rt12	Qz	4204	451	10727	b.d.l.	92	950	1·45	4·6	204
J-Grt1-Rt13	Ap	3554	232	10882	b.d.l.	47	928	1·45	3·9	342
Average							929 ± 23			
Matrix rutile ($n = 67$)										
median		969	1007	1405	1053	b.d.l.	738	0·65	≤2·0	—
mean		925	975	1564	995	b.d.l.	733	0·65	≤2·0	—
maximum		1256	2138	8464	1344	327	764	0·65	≤2·0	—
minimum		52	205	399	257	b.d.l.	514	0·65	≤2·0	—
Sample Z7-15-2 (mafic granulite)										
HMS-grain #1		54	187	4054	b.d.l.	b.d.l.	516	0·65	—	—
HMS-grain #2		879	175	1869	b.d.l.	b.d.l.	728	0·65	—	—
HMS-grain #4		81	441	3344	193	b.d.l.	541	0·65	—	—
HMS-grain #5		41	396	5420	b.d.l.	b.d.l.	501	0·65	—	—
HMS-grain #6		54	b.d.l.	3963	b.d.l.	b.d.l.	516	0·65	—	—
HMS-grain #7		1195	96	2565	b.d.l.	b.d.l.	759	0·65	—	—
Inclusion in Grt*	Qz	868	435	9119	b.d.l.	5528	741	0·95	—	—

Temperatures (*T*) are calculated from Zr contents assuming the pressure given using the calibration of Tomkins *et al.* (2007). The pressures (*P*) were estimated from grossular contents in garnet (for garnet inclusions) and from the retrograde equilibration stage at 0·65 GPa for matrix rutile. The last column *d* (μm) gives the distance of the rutile inclusion from the edge of the host garnet (distances are given only for rutile in garnet from thin sections, not grain mounts). b.d.l., below electron probe detection limit. Qz, quartz; Ap, apatite; Hc, hercynite; Sil, sillimanite. The grossular content of matrix garnet refers to the rim composition of garnet in this sample.

*This analysis was performed on a very small (6 μm × 6 μm) rutile inclusion in garnet and Si and Fe are affected by the host garnet.

rutile + quartz + hercynite, and one rutile + sillimanite inclusion) approximately fall into three subgroups (Fig. 8a; Table 3): (1) rutile included in the low-Ca cores of the largest garnet grains (~2·3% grossular) shows Zr contents between 1290 and 1448 μg g^{-1}; (2) rutile included in garnet with >5% grossular has Zr contents between 1403 and 2282 μg g^{-1}; (3) the highest Zr contents in rutile between 3268 and 4204 μg g^{-1} are found only in garnet with grossular contents between 3·9 and 4·6%.

The connection between the Zr content of rutile inclusions (19 grains) and their position within the host garnet was investigated in detail in one large grain ('J-Grt1; ≥6 mm diameter; Supplementary Data Fig. S3). The results show a clear relationship between the Zr content of rutile grains and their spatial position in the host garnet (Fig. 8b). Inclusions in the low-Ca core region of the garnet have low Zr contents between 1290 and 1448 μg g^{-1}, whereas the Zr contents of rutile grains included within 600 μm of the preserved grain edge are elevated to ~4000 μg g^{-1}. This is also the approximate width of the garnet rim region showing elevated Ca contents (discussed above). Rutile inclusions that are very close to the grain edge (within 200 μm) again show lower levels of Zr (1481–2282 μg g^{-1}; Fig. 8b; Table 3, and Supplementary Data table).

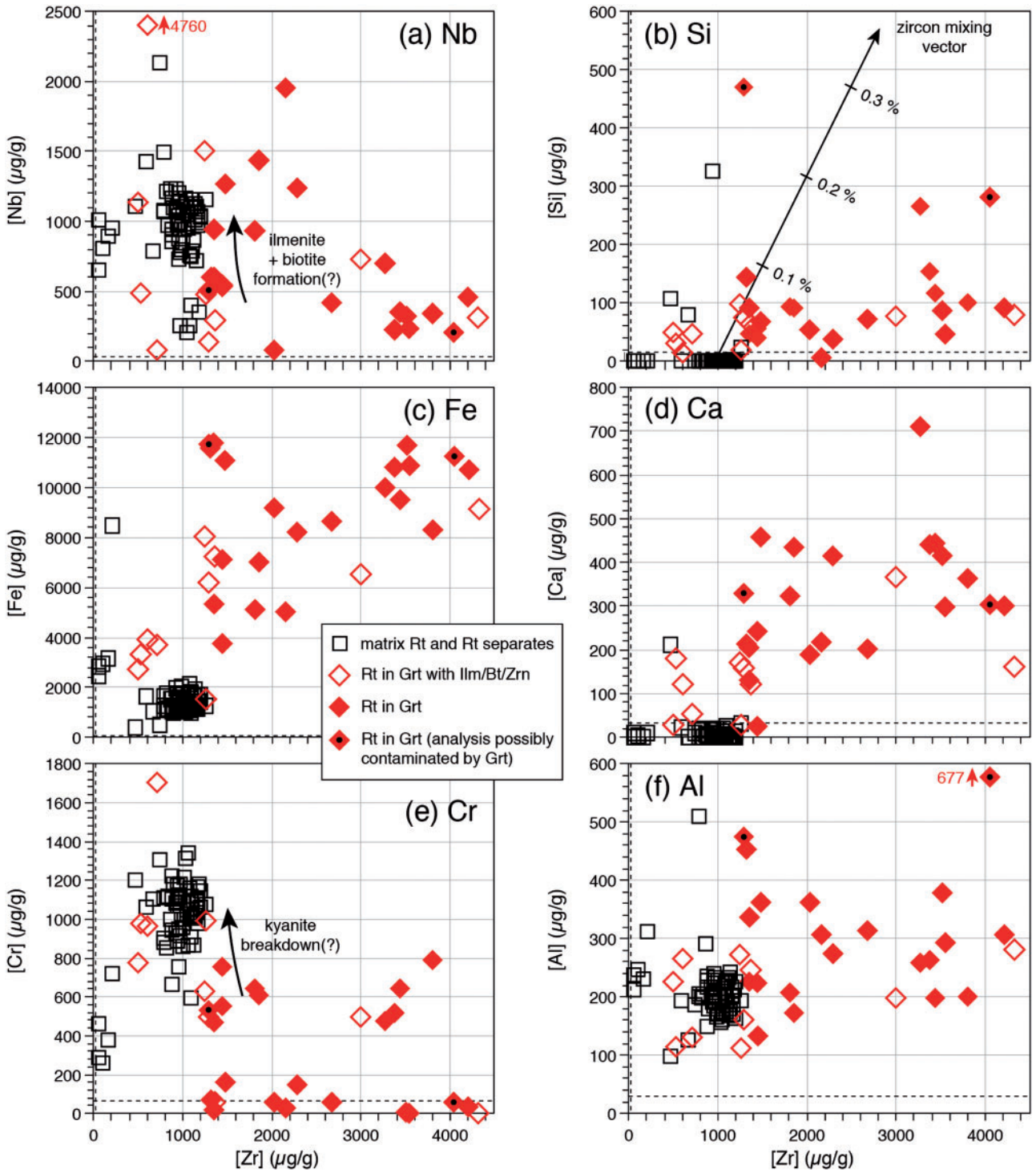

Fig. 7. Rutile trace element concentrations in felsic granulite sample Z7-14-5. Open squares, rutile grains in the rock matrix and grains picked from heavy-mineral separate ($n = 67$); open diamonds, rutile inclusions in garnet intergrown with ilmenite, biotite, and/or zircon; filled diamonds, isolated, single-phase rutile inclusions in garnet ($n = 9$) and rutile inclusions in garnet intergrown with quartz or hercynite + quartz ($n = 10$); filled diamonds with dot, analysis of rutile inclusion in garnet possibly contaminated by host garnet ($n = 2$). The majority of matrix grains have Zr, Nb, Fe and Cr abundances of ~1000 μg g^{-1}, and Ca and Si below the EPMA detection limit. The theoretical vector for mixed rutile–zircon analyses is shown in (b), but the analyses do not follow this vector. Many rutile inclusions in garnet preserve elevated Zr concentrations (equivalent to higher temperatures of equilibration), low Nb and Cr, but elevated Ca and Si contents. Higher Nb and Cr contents in matrix rutile are interpreted to reflect retrograde formation of ilmenite, biotite and sillimanite from rutile and kyanite. The full dataset is given in the Supplementary Data tables. Images of all rutile inclusions in garnet and an across-grain profile of a large matrix grain are provided in Supplementary Data Figs S1 and S2.

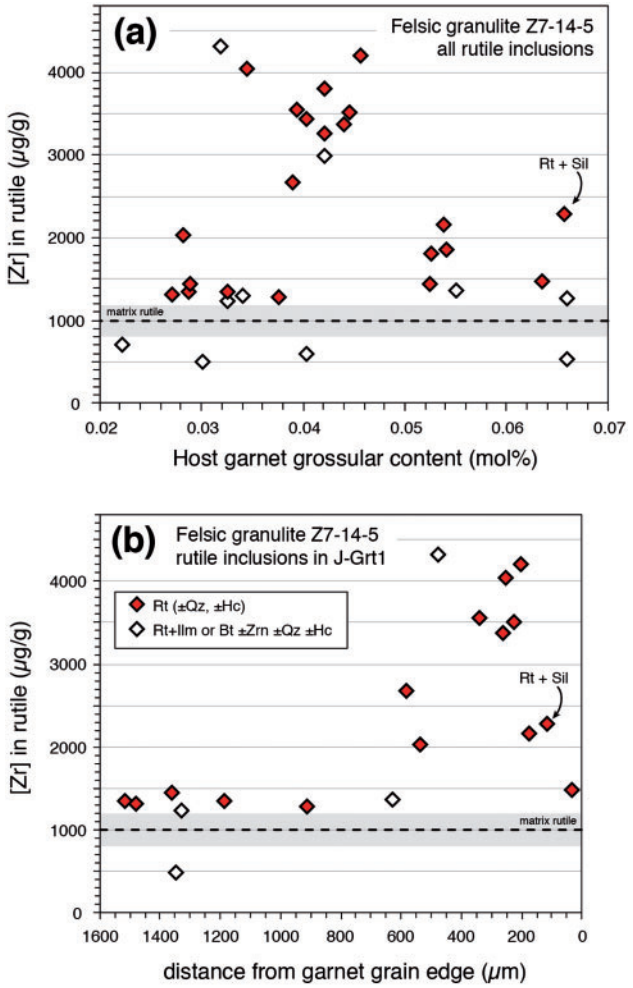

Fig. 8. Zirconium concentration of rutile grains included in garnet. Open diamonds, rutile inclusions in garnet intergrown with ilmenite, biotite, and/or zircon that are potentially influenced by retrograde exchange with the coexisting Zr–Ti-bearing minerals. Filled diamonds, isolated, single-phase rutile inclusions in garnet and rutile inclusions in garnet intergrown with quartz or hercynite + quartz or sillimanite. These rutile grains are probably shielded from post-entrapment Zr and Ti exchange with their environment. (a) Rutile Zr content vs grossular content of the garnet hosts at the site where the respective rutile is located. The rutile grains fall approximately into three distinct groups on this plot, which are critical to the reconstruction of the *P–T* path. (b) Zr content of rutile inclusions in garnet grain J-Grt1 (see Supplementary Data) as a function of distance from the edge of the garnet grain. It should be noted that high-Zr rutile is restricted to the rim of the garnet host. Images of all rutile inclusions are provided in Supplementary Data Fig. S2.

The compositions of the other rock-forming minerals in Z7-14-5 are as follows. Perthite consists of an alkali feldspar host ($Or_{88·5–93·2}Ab_{6·8–11·3}An_{<0·2}$) with albitic lamellae and rims ($Or_{1·0–2·0}Ab_{88·0–95·7}An_{1·4–11·0}$). Alkali feldspar grains without exsolution textures have a similar composition to the perthite hosts and probably represent recrystallized grains. Host compositions of the antiperthite are albite rich ($Ab_{77·0–81·1}$) with only a minor K-feldspar component (<1·3%), whereas the lamellae have a similar composition to the host domains of perthite ($Or_{90}Ab_{10}$).

Biotite is characterized by highly variable compositions. Chlorine contents correlate negatively with Mg# and range from 0·3 to 2·1 wt %. The Ti contents range from below detection limit (0·04 wt %) to 4·25 wt % TiO_2, and Mg# is 52·2–72·9. Biotite inclusions in garnet, large-sized biotite grains (>250 μm) and biotite next to sillimanite have the highest Ti contents.

Muscovite in the symplectites around garnet is characterized by 4·8–6·5 mol % paragonite. The celadonite component ranges from 7·4 to 10·5%. The chemical composition of muscovite next to sillimanite does not differ from that of the white mica within the coronae surrounding garnet.

Amphibolized mafic garnet granulite Z7-15-2

Garnet shows intra-grain zonation including homogeneous core plateaux and rim domains depleted in Mg and Ca and enriched in Fe and Mn. The compositions of most garnet relics are spessartine rich ($Alm_{63}Prp_{16}Grs_{12}Sps_9$), but some cores preserve chemical zoning towards more Mg–Ca-rich and Fe–Mn-poor composition ($Alm_{59}Prp_{21}Grs_{18}Sps_2$; Supplementary Data). Plagioclase has high anorthite contents of around 89%; inclusions in garnet have slightly lower contents of 81%. No difference between plagioclase within symplectites surrounding garnet and the sub- to euhedral grains was observed. The composition of the majority of the enstatite is homogeneous with 1·2–1·6 wt % Al_2O_3, 1·0 wt % MnO and Mg# = 53–55. Some core domains of orthopyroxene in the symplectites surrounding garnets show higher Al_2O_3 contents (up to 2·8 wt %) and Mg# (up to 63), and lower MnO (as low as 0·4 wt %). One rutile inclusion in garnet from the heavy-mineral separate was analysed and showed a relatively low Zr content (868 μg g^{-1}; Table 3). Six rutile grains from the heavy-mineral separate were also analysed and showed Zr contents that were close to detection limit in four grains, but higher in the remaining two (Table 3).

Cummingtonite (Mg# 58–61) coexists with magnesiohornblende (Mg# 65–72, Fe^{3+}/Fe_{tot} 0·28–0·38). Amphibole inclusions in garnet are tschermakite with higher Mg# (78–86) and A-site occupancy (up to 46%) and lower Si (6·25–6·39 per formula unit) than the green hornblende in the matrix. TiO_2 contents of the tschermakite and the hornblende range from 0·6 to 1·4 wt % with the highest contents found in the tschermakite inclusions in garnet. The A-site occupancy of the hornblende is ~30%, dominated by Na.

Geothermobarometry

Felsic granulite Z7-14-5

An isochemical phase diagram ('pseudosection') was calculated for sample Z7-14-5, which includes isolines for the modal abundance and chemical composition of garnet using Perple_X, version 6.7.1 (Connolly, 2005, 2009). The thermodynamic data of Holland & Powell (2011) and the following mixing models were used: silicate melt [melt(HP); Holland & Powell, 2001; White

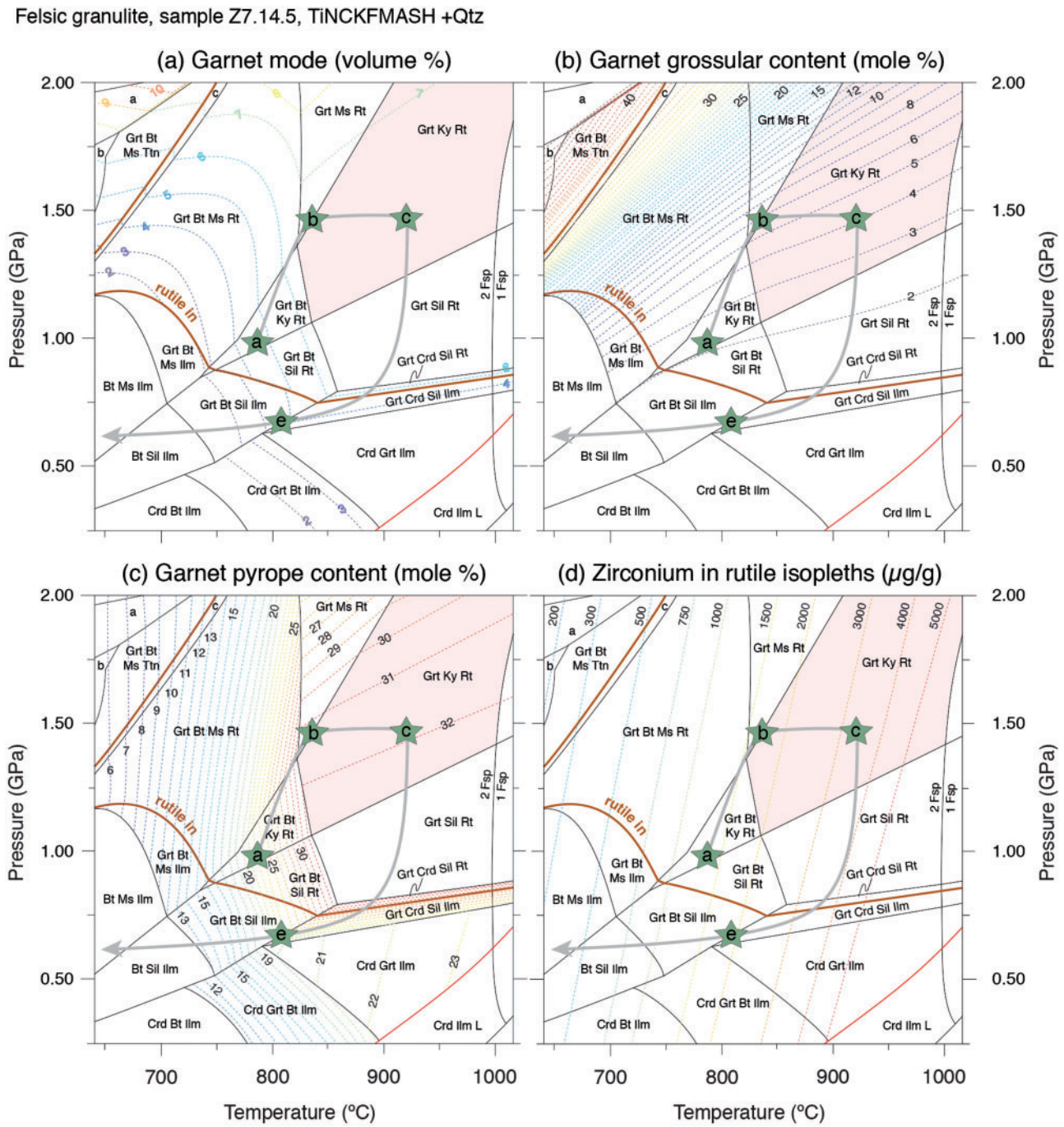

Fig. 9. Isochemical *P–T* phase diagram ('pseudosection') for felsic granulite sample Z7-14-5 calculated from the whole-rock composition determined by XRF. All fields include quartz and two feldspars in addition to the listed phases, with the exception of the high-*T* field labeled '1 Fsp', which contains only one feldspar. The thick brown line marks the boundary of the field of rutile stability in this rock. (a) Isopleths of volume per cent garnet mode; (b) isopleths of grossular content in garnet; (c) isopleths of pyrope content in garnet; (d) isopleths of Zr in rutile (Tomkins *et al.*, 2007). Metamorphic stages M_{2a}, M_{2b}, M_{2c} and M_{2e} are marked with stars along the *P–T* path (grey line with arrow). Stages M_{2a}, M_{2b} and M_{2c} are reconstructed by the combination of Zr-in-rutile thermometry on rutile inclusions and the pressures derived from the grossular content of their respective garnet hosts. Stage M_{2d} is not recorded in sample Z7-14-5. Mineral abbreviations follow Whitney & Evans (2010).

et al., 2001], feldspar (Fuhrmann & Lindsley, 1988), garnet (GtWPH; White *et al.*, 2007), cordierite (hCrd: ideal model of Baumgartner, L., unpublished data, 2003), biotite [TiBio(HP); Powell & Holland, 1999], pyroxenes [Opx(HP) and Cpx(HP); Powell & Holland, 1999], and ilmenite [Ilm(WPH): White *et al.*, 2000].

The pseudosection (Fig. 9) was calculated in the system TiO_2–Na_2O–CaO–K_2O–FeO–MgO–Al_2O_3–SiO_2–H_2O ('TiNCKFMASH') using the chemical composition of the whole-rock (Table 2). Hydrous minerals in the rock are restricted to the dark biotite–cordierite-rich layers and rare inclusions of biotite in the garnet. These account

for the 0·72% loss on ignition in the whole-rock analyses, most probably in the form of OH^- and H_2O in these minerals. Most of these are hydrous minerals that formed on the retrograde path, probably through the influx of external fluids; the prograde and peak metamorphic H_2O contents of the rock are unknown. The pseudosection was, therefore, calculated with excess H_2O to compute possible maximum stabilities of hydrous phases (biotite, muscovite), but no H_2O-bearing melt was allowed (Fig. 9). High amounts of H_2O would lead to partial melting of this felsic rock, in particular at ultrahigh temperatures. A calculation of a bulk composition with 0·72% H_2O with the inclusion of H_2O-bearing melt results in the same peak assemblage (garnet + kyanite + rutile + two feldspars + quartz) as in the dry-melt case, but with the addition of a small portion of silicate liquid at temperatures above ~720°C (not shown). Garnet grossular isopleths are not strongly influenced by the presence or absence of melt, whereas Mg/Fe ratios of garnet are higher in the melt-present case, owing to the preferential partitioning of Fe into the melt. The garnet pyrope isolines displayed in Fig, 9c, therefore, may or may not be relevant for the prograde path of the sample, but they are plotted to represent peak and retrograde compositions, during which cordierite, ilmenite and biotite formed. The dry solidus of the rock is indicated in Fig. 9.

The stable assemblage inferred for sample Z7-14-5 (garnet + kyanite + rutile + two ternary feldspars + quartz) is predicted to be stable over a large *P–T* range at temperatures between approximately 800 and 1000°C and at pressures above 1·1 GPa to 1·4 GPa (depending on *T*; Fig. 9). The Ti-bearing phase is ilmenite at low pressures and low temperatures, and rutile at high pressures and high temperatures (rutile-in curve in Fig. 9). Garnet is the only predicted Mg- and Fe-bearing mineral in sample Z7-14-5 at high temperatures and pressures in excess of ~0·8 GPa, and the garnet mode is very constant between 6 and 7 vol. % for the *P–T* region > 0·8 GPa and >800°C (Fig. 9a). The pyrope isolines are far spaced in this region and predict a slight decrease from the maximum pyrope content of ~32 mol % close to the kyanite–sillimanite phase boundary to ~30 mol % at *c.* 2 GPa (Fig. 9c).

The grossular content of garnet is very sensitive to pressure and provides a good barometer for this sample (Fig. 9b). The Ca zonation observed in garnet grains of different grain sizes provides the key to unravelling a larger section of the prograde and retrograde *P–T* path, especially in combination with rutile inclusions found in the respective garnet growth zones (see below). It should be noted that the larger garnet grains in this sample preserve low-Ca cores, which are interpreted as relics from the prograde history of the rock. The core domains of these garnets were effectively removed from the reaction volume of the rock for any subsequent *P–T* stage of the rock, such as the peak-*T* and the retrograde stages. This fractionation effect is not accounted for in our pseudosection calculation. This is a general problem of the pseudosection technique and has been addressed in other studies by adjusting the bulk composition along the *P–T* path (e.g. Konrad-Schmolke *et al.*, 2005; Zeh, 2006). We have not attempted this procedure here, and instead have calculated the pseudosection for a constant bulk-rock composition as determined by XRF analysis.

In rocks that contain the assemblage rutile + zircon + quartz, the Zr-in-rutile thermometer has a high potential to preserve evidence for ultrahigh-temperature conditions, whereas conventional thermometry commonly underestimates the peak temperatures owing to advanced re-equilibration during retrogression (e.g. Zack *et al.*, 2004; Kooijman *et al.*, 2012; Ewing *et al.*, 2013). Typically, matrix rutile re-equilibrates during cooling, whereas inclusions in garnet preserve higher Zr contents and may record the earlier high-temperature history of high-grade rocks (e.g. Zack *et al.*, 2004; Kooijman *et al.*, 2012). Sample Z7-14-5 was saturated in zircon and quartz throughout its *P–T* history. Thus, Zr-in-rutile thermometry was used to estimate the temperatures of garnet growth stages using rutile inclusions in garnet. The pressure-dependent calibration of Tomkins *et al.* (2007) was employed in combination with pressures retrieved from the grossular isopleths displayed in the pseudosections (Fig. 9b). Temperatures calculated through alternative Zr-in-rutile calibrations are provided in the Supplementary Data table.

The first subgroup of rutile inclusions that occur in the low-Ca core plateau region of the large garnet grains with ~2·3% grossular have Zr contents (1290–1448 μg g^{-1}) that reflect temperatures of 781–794°C (weighted mean 786 ± 9°C; 95% confidence level) at a pressure of 0·95 GPa (metamorphic Stage M_{2a}; Fig. 9b and d).

The subgroup of rutile grains included in the highest-Ca zones of the large grains and in small high-Ca grains with grossular contents >5% have slightly higher Zr contents (1437–2282 μg g^{-1}) that translate to temperatures of 818–871°C (weighted mean 844 ± 44°C) at a pressure of 1·45 GPa (Stage M_{2b}; Fig. 9d). The higher pressure estimated for the equilibration of this group of rutile inclusions is required to stabilize the much higher grossular content of their garnet hosts (Figs 8 and 9b).

The third subgroup of rutile inclusions, which has the highest Zr concentrations (3270–4200 μg g^{-1}), is included in garnet with moderately high grossular contents (3·9–4·6%), requiring temperatures of 917–950°C with a weighted mean of 929 ± 23°C at a pressure of 1·45 GPa (Stage M_{2c}; Fig. 9d). The pressure estimated for this third group of rutile inclusions, which equilibrated at the highest temperature, is identical to the pressure estimated for the second subgroup described above. This is due to the slight positive Clapeyron slope of the grossular isopleths, which results in a slight difference in grossular contents from 5–7% at 844°C to ~4% at 929°C at a constant pressure of 1·45 GPa. The three subgroups of rutile inclusions, in conjunction with their different garnet hosts, therefore, record three

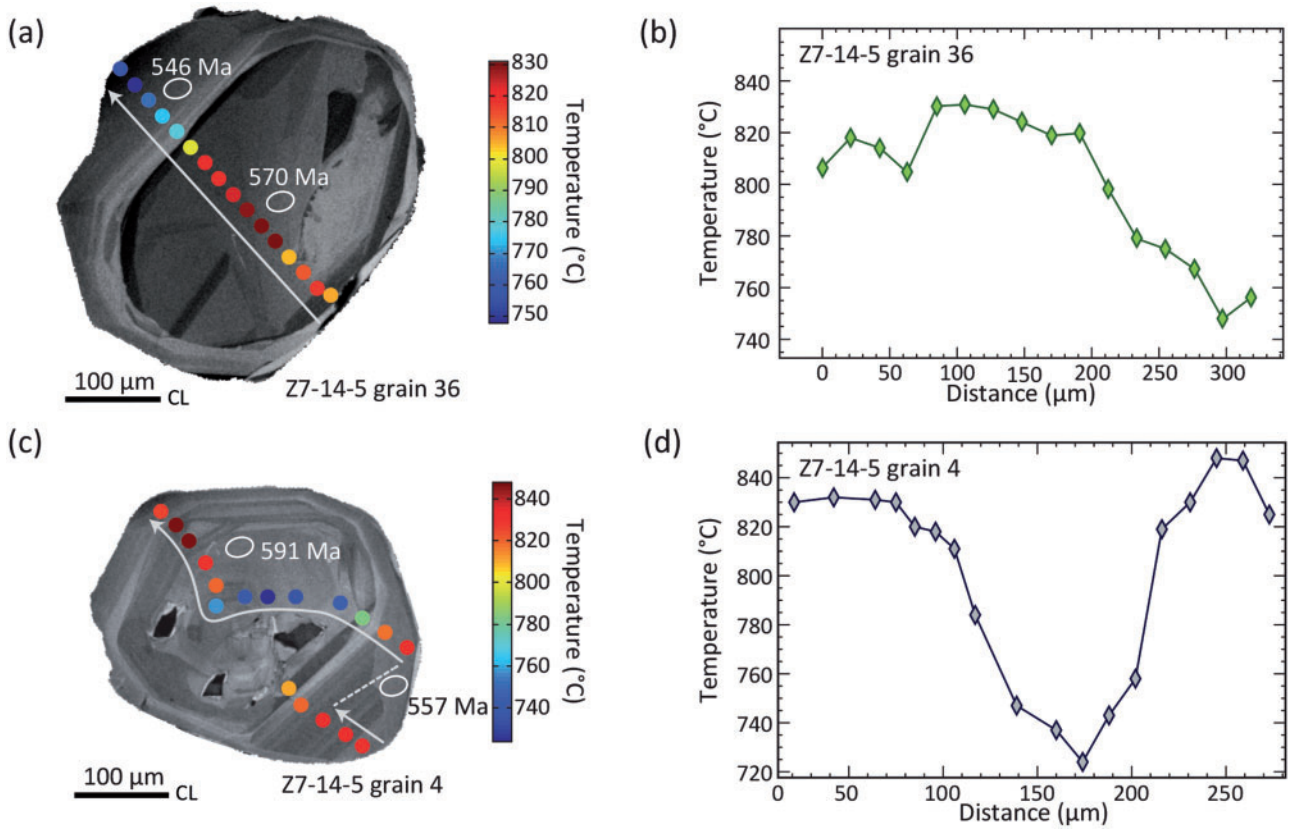

Fig. 10. (a, c) Cathodoluminescence images of polished zircon grains from felsic granulite sample Z7-14-5 with spot locations of U–Pb ages (white circles) and Ti analyses (coloured spots). The colour scheme represents Ti-in-zircon temperatures. (b, d) Rim–core–rim across-grain Ti-in-zircon temperature profiles of the sections displayed in (a) and (c), respectively. Profile (b) is interpreted as retrograde zircon growth, whereas the core of the grain in (c) and the profile displayed in (d) are interpreted as evidence of zircon growth during heating. Temperatures are calculated after Watson *et al.* (2006) and are assumed to be accurate for a pressure of 1 GPa.

subsequent *P–T* stages from 786°C at 0·95 GPa to a much higher pressure of 1·45 GPa at an only slightly higher temperature (844°C), followed by isobaric heating to ultrahigh temperatures of ~930°C (Fig. 9).

Temperatures based on the solubility of an element in a mineral, such as Zr in rutile, are considered minimum temperatures, owing to the possibility of retrograde diffusive Zr loss (e.g. Zack *et al.*, 2004). Nevertheless, high Zr concentrations in the group of rutile inclusions in the Ca-rich garnet preserve peak temperatures of 929 ± 23°C, which provide evidence for ultrahigh temperatures (UHT) of metamorphism. The UHT field was defined by Harley (1998) as crustal metamorphism in excess of 900°C at pressures not exceeding the stability field of sillimanite. Hence in the strict sense, the H.U. Sverdrupfjella rocks do not fall into the UHT field, as the peak metamorphic conditions are in the stability field of kyanite. *P–T* conditions in the stability field of kyanite are petrographically supported by the presence of the large angular aggregates of sillimanite that are interpreted as pseudomorphs after kyanite.

The matrix rutile grains show a narrow range in Zr concentrations that translate to a narrow range in temperatures that are significantly below the peak temperatures preserved by the inclusions in garnet. These lower concentrations are interpreted to represent loss of Zr from the matrix rutile during cooling on the retrograde path. The formation of assemblages containing cordierite + ilmenite + biotite + sillimanite (Fig. 4c) provides a pressure estimate for early retrograde conditions of ~0·6–0·7 GPa (Fig. 9). Temperatures for matrix rutile equilibration were, therefore, calculated for a pressure of 0·65 GPa. Matrix rutile is very homogeneous without preserved zoning in Zr or any strong zonation in any of the other analysed elements (see Supplementary Data Fig. S1). The majority of matrix grains (82% of the 67 grains analysed) give equilibration temperatures of 722–764°C. The median temperature of all analysed matrix grains is 738°C, and the mean is 733°C (Table 3).

Complementary to Zr-in-rutile thermometry, the Ti concentration in zircon has been calibrated as a thermometer for a pressure of 1·0 GPa (Watson *et al.*, 2006). A pressure correction has been suggested by Ferriss *et al.* (2008), based on a quantum-mechanical calculation, as 100°C GPa^{-1} at pressures below 2 GPa. Titanium concentrations and intra-grain zonation in several zircon grains in sample Z7-14-5 were determined and yield temperatures of 709–876°C for a pressure of 1 GPa (Fig. 10; Table 4). Pressure correction results in

Table 4: Zircon Ti content and thermometry for felsic granulite sample Z7-14-5

Grain	Zone	[Ti] ($\mu g\ g^{-1}$)	*T* (W'06) (°C)	*T* (F'08) (°C), 0·65 GPa	*T* (F'08) (°C), 1·45 GPa	$^{206}Pb/^{238}U$ age (Ma)
1	core	35·5	866	831	911	553 (2)
3	core	18·4	798	763	843	n.d.
4	core	8·2	724	689	769	n.d.
	mantle	22·8	819	784	864	593 (1)
	rim	30·0	848	813	893	556 (1)
5	core	15·2	779	744	824	n.d.
	mantle	36·6	870	835	915	569 (1)
7	core	10·6	746	711	791	571 (2)
9	core	27·3	838	803	883	587 (2)
	rim	31·3	852	817	897	567 (4)
17	core	22·2	816	781	861	593 (1)
	mantle	28·3	841	806	886	574 (3)
	rim	10·9	749	714	794	n.d.
23	mantle	37·9	873	838	918	554 (3)
	rim	12·7	763	728	808	541 (1)
29	core	19·9	805	770	850	543 (1)
	mantle	14·8	777	742	822	539 (2)
32	core	20·6	809	774	854	594 (1)
	mantle	20·5	808	773	853	569 (4)
	mantle	24·2	825	790	870	568 (4)
33	core	27·6	839	804	884	567 (3)
	rim	6·9	709	674	754	n.d.
34	core	23·7	823	788	868	568 (4)
	core	38·8	876	841	921	561 (5)
36	core	25·7	831	796	876	570 (5)
	rim	13·3	767	732	812	547 (2)
37	core	18·4	798	763	843	573 (5)
	core	23·0	820	785	865	564 (8)
39	core	20·4	808	773	853	590 (5)

T (W'06) is temperature (in °C) calculated using the calibration of Watson *et al.* (2006), which was calibrated for a pressure of 1·0 GPa. Ferriss *et al.* (2008) estimated a pressure correction for the Ti-in-zircon thermometer of 100°C GPa^{-1}, which was applied for the columns labeled F'08.

temperatures of up to 921°C for a pressure of 1·45 GPa (Table 4). The same zircon grains and growth zones that were analysed for Ti concentrations were also dated by the U–Pb method. Dating results show that the UHT metamorphic overprint is clearly of Pan-African age (see section on geochronology below for a detailed discussion of these ages).

Garnet has preserved four stages of growth or recrystallization in its grossular content, three of which contain rutile inclusions and were used to reconstruct two prograde metamorphic stages and the UHT peak metamorphic stage, as discussed above. The last *P–T* stage recorded in garnet is represented by the low-grossular rims that have lower pyrope contents and elevated Fe (Fig. 5). The pyrope content of the smaller garnet grains ($\leq$2·5 mm diameter) show core plateaux with 23–25% pyrope (Fig. 5), which we interpret to result from diffusive equilibration at temperatures of 800–820°C (Fig. 9c; Stage e). Low pressures for this stage are recorded in the low grossular content of the garnet, but a more quantitative estimate of pressure is given by the cordierite-bearing symplectites around garnet and the assemblage cordierite + sillimanite + ilmenite + biotite. The latter is estimated to be 0·65 ± 0·10 GPa (Fig. 9).

The low-Ca zones in the cores of the largest garnet grains clearly predate the UHT metamorphic event. This preservation of prograde zoning puts constraints on the duration of the UHT event, which can be quantified through diffusion modelling. Calcium diffusion in garnet has been determined experimentally and through the evaluation of arrested diffusion profiles in natural rocks (e.g. Schwandt *et al.*, 1996; Carlson, 2006; Vielzeuf *et al.*, 2007). The diffusion coefficients for the garnet compositions and peak temperature relevant for our study among these various calibrations agree within one or two orders of magnitude; these are $\log(D_{Ca}) = -22{\cdot}14$ $m^2\ s^{-1}$ (Schwandt *et al.*, 1996) and $\log(D_{Ca}) = -21{\cdot}35$ $m^2\ s^{-1}$ (Vielzeuf *et al.*, 2007). Carlson (2006) found a small effect of oxygen fugacity on Ca diffusion in garnet. For an oxygen fugacity buffered at the graphite–oxygen buffer, the $\log(D_{Ca})$ value is –20·66 $m^2\ s^{-1}$, whereas it is –20·99 $m^2\ s^{-1}$ at two log units below graphite–oxygen (calculations based on the garnet core composition). Three Ca concentration profiles across the high-Ca rim zones of one large garnet grain were used for diffusion modelling (Fig. 6). All three profiles were modelled with the same set of temperature (929°C) and diffusion coefficient–time products (*Dt*), and assuming an initial step function in Ca from the measured concentration in the core (~1 wt %) to the highest Ca content (2·4 wt %) observed in the rim. Diffusive relaxation of the Ca step function was modelled by fitting an error function to the measured data using a one-dimensional, semi-infinite diffusion model (Crank,

1975). A one-dimensional model is justified for the largest garnets that still preserve large, homogeneous core regions. The small garnet grains would require a spherical diffusion model, but they were not evaluated further here. Furthermore, garnet is resorbed at its rims and replaced by cordierite-bearing symplectites during the later stages of decompression (see below), and the composition of the rim region of garnet has adjusted to the lower *P*–*T* conditions. This is evident from short, steep Ca profiles that modify the outermost ~50 μm of the garnet (Fig. 6). This late-stage process is ignored in the diffusion model, but the time needed to form these short profiles also contributed to the relaxation of the core–rim Ca zonation. Our simplified model is calculated only for the peak temperature and, therefore, provides only an estimate for the maximum time that peak temperatures may have prevailed. The diffusion coefficients listed above result in time estimates ranging from less than half a million years to 1 Myr to 6·2 Myr for the diffusion coefficients calculated from the calibrations of Carlson (2006), Schwandt *et al.* (1996), and Vielzeuf *et al.* (2007), respectively (Fig. 6).

Rutile and garnet typically react to form ilmenite at low pressures exemplified by the reactions GRIPS (garnet + rutile reacting to plagioclase + ilmenite + quartz; e.g. Bohlen & Liotta, 1986) and GRAIL (garnet + rutile reacting to ilmenite + aluminosilicate + silica; Bohlen *et al.*, 1983). The cordierite-bearing coronae around garnet that are also breakdown products of garnet are mostly preserved as pinite. The pinite as well as the biotite–quartz–pinite symplectites indicate the former presence of cordierite, and cordierite–quartz symplectites ± biotite. Reactions involving garnet that probably produced cordierite in the reaction domains are evidence for high-*T* and medium- to low-*P* conditions, during which garnet reacts with aluminosilicate and quartz to form cordierite (e.g. Bucher & Grapes, 2011). The reaction may also involve alkali feldspar and produce cordierite–quartz–biotite assemblages (e.g. Marschall *et al.* 2003; Bucher & Grapes, 2011).

Biotite represents a further breakdown product of garnet. Most of the symplectitic biotite grains have low Ti contents. One biotite grain from a granitic inclusion (quartz + K-feldspar + plagioclase + biotite) within monazite was analysed and yielded 3·4 wt % TiO_2 and a Mg# = 47·5. The monazite grain was dated chemically (see section on geochronology below) and is part of the dominant age peak at 539 Ma. The granitic inclusion in this monazite grain supports the zircon data constraining timing of the peak metamorphic conditions to a minimum age of 539 Ma.

Amphibolized mafic garnet granulite Z7-15-2

Unfortunately, the compositions of the garnet and plagioclase relics in sample Z7-15-2 have been modified during retrogression, and it is, therefore, not possible to retrieve reliable estimates of peak *P*–*T* conditions. However, the observed textures record the decompression, rehydration and cooling history of the rock. These include formation of orthopyroxene–plagioclase symplectites between garnet and quartz, formation of ilmenite from rutile, and formation of hornblende and cummingtonite from orthopyroxene and garnet.

The orthopyroxene–plagioclase symplectites between garnet and quartz indicate near-isothermal decompression under granulite-facies conditions (Harley, 1989), or at least a high-*T*–low-*P* stage subsequent to a high-*P* stage. Orthopyroxene + plagioclase symplectites and other orthopyroxene and plagioclase (Type II) are interpreted to have resulted from the reaction between Type I plagioclase, garnet and quartz (GOPS: garnet + quartz reacts to orthopyroxene + plagioclase; e.g. Harley, 1989; Mengel & Rivers, 1991; Marschall *et al.*, 2003).

The presence of orthopyroxene and plagioclase in the coronae around garnet permits an estimate of pressure for the formation of these garnet breakdown products along the GOPS reaction. The geobarometers of Newton & Perkins (1982) and Eckert *et al.* (1991), based on coexisting orthopyroxene, plagioclase and garnet, were both applied. Only the innermost orthopyroxene and adjacent plagioclase in the coronae were used in combination with garnet rim compositions, which are most likely to represent an equilibrium state. The calibration of Newton & Perkins (1982) results in a pressure range of 0·59–0·86 GPa for different mineral triplets. The pressures obtained with the calibration of Eckert *et al.* (1991) are in the same range (0·54–0·82 GPa). The wide range of estimated pressures may reflect the continuous breakdown of garnet on the decompression path, but may also be a result of subsequent diffusive exchange of Fe and Mg between orthopyroxene and garnet. Temperatures recorded by the assemblage via orthopyroxene–garnet Mg–Fe thermometry are low (520–697°C; Harley, 1984), whereas Al-in-Opx temperatures recorded by the orthopyroxene are between 754 and 862°C for the highest alumina contents and range of Mg-numbers observed in orthopyroxene in this sample assuming a pressure of 0·75 GPa (Aranovich & Berman, 1997, corrected). For a pressure of 0·86 GPa, the highest Al-in-Opx temperature is 881°C. Ilmenite typically forms from rutile upon decompression presumably by a reaction with Fe-bearing silicate, such as GRIPS.

A pseudosection was calculated for sample Z7-15-2 in the system TiMnNCKFMAS with quartz in excess using the bulk-rock composition determined by XRF analysis (Fig. 11; Table 2). No H_2O and no hydrous phases were included, because hornblende and cummingtonite are interpreted as retrograde phases that formed during rehydration after decompression. The pseudosection is contoured for modal abundances of orthopyroxene (Fig. 11a) and clinopyroxene (Fig. 11b). The *P*–*T* path determined for the felsic granulite sample Z7-14-5 is shown for comparison. The peak pressure conditions determined for the felsic granulite (stages

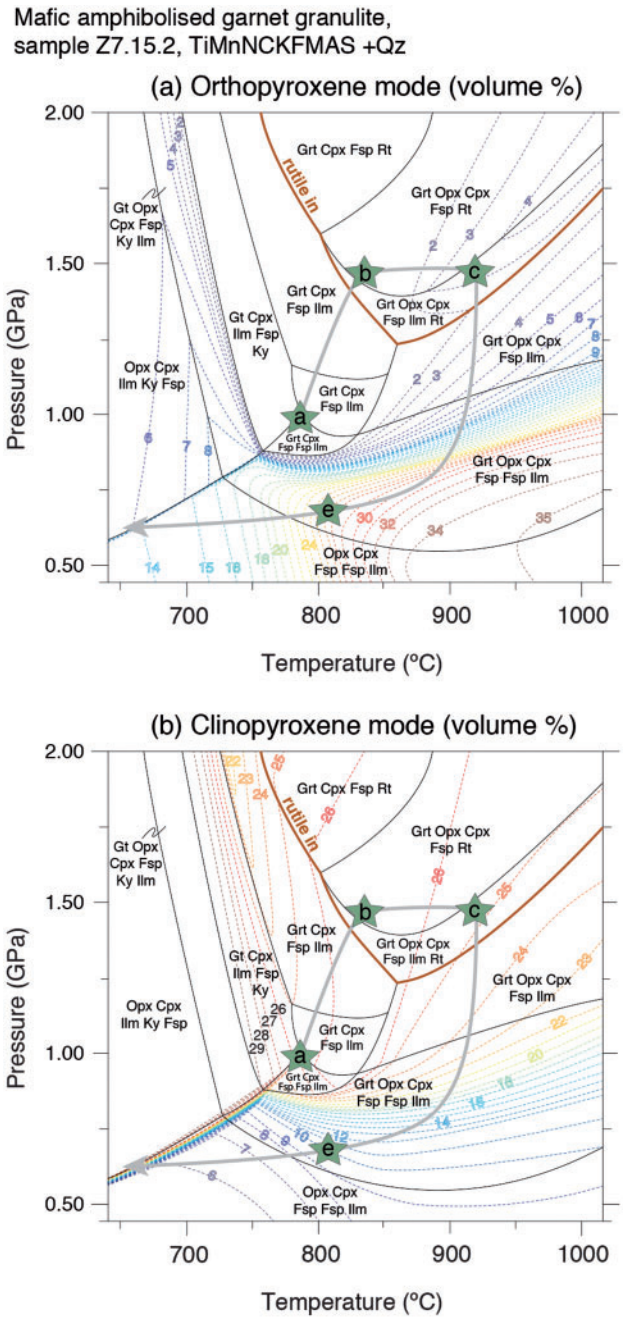

Fig. 11. Isochemical *P–T* phase diagram ('pseudosection') for mafic granulite sample Z7-15-2 calculated from the whole-rock composition determined by XRF. All fields include quartz in addition to the listed phases. The thick brown line marks the boundary of the field of rutile stability in this rock. (a) Isopleths of volume per cent orthopyroxene mode; (b) isopleths of volume per cent clinopyroxene. Metamorphic stages a, b, c and e (which refer to metamorphic stages 2a, 2b, 2c and 2e, respectively) and the *P–T* path derived from sample Z7-14-5 are shown for comparison. Mineral abbreviations follow Whitney & Evans (2010).

M_{2b} to M_{2c}) are consistent with the occurrence of rutile in the mafic granulite. The pseudosection further predicts that the mafic granulite contains very little orthopyroxene (~0–3 vol. %) at peak pressures, whereas the amount of clinopyroxene in this rock is predicted at ~25 vol. %. These abundances are predicted to be approximately reversed during decompression (Fig. 11). The orthopyroxene mode is predicted to increase during decompression to ~30 vol. % at low-*P*–high-*T* conditions and then decrease again upon cooling (Fig. 11a). The strongest increase in orthopyroxene mode between approximately 0·9 GPa (10%) and 0·6 GPa (30%; Fig. 11a) is consistent with the range of pressures calculated for the orthopyroxene symplectites by orthopyroxene–garnet barometry (i.e. 0·86–0·59 GPa).

The abundance of clinopyroxene is predicted to strongly decrease to ~10 vol. % at the low-*P* metamorphic Stage M_{2e} (Fig. 11b). It is evident from petrographic observation that hydration and the formation of cummingtonite consumed a large portion of the orthopyroxene, and it is likely that the remaining clinopyroxene was transformed to hornblende. No relic clinopyroxene was observed in our sample, but it has been reported from mafic lenses in the Rootshorga paragneiss (Board *et al.*, 2005). However, such clinopyroxene relics are described as very rare and restricted to the cores of resistant tectonic lenses (Board *et al.*, 2005).

An-rich plagioclase is predicted to be part of the stable mineral assemblage of sample Z7-15-2 along the entire *P–T* path, consistent with petrographic observation of the occurrence of large euhedral plagioclase (although it was largely replaced by quartz and sericite during rehydration). The rock is, therefore, classified as a retrogressed garnet granulite, not an eclogite, despite the large predicted mode of garnet and clinopyroxene at peak *P–T* conditions.

P–T conditions for rehydration during or after decompression were determined. In domains in which hornblende appears to be in textural equilibrium with plagioclase, the paragenesis hornblende + plagioclase provides a temperature estimate for the retrograde conditions during hydration. To this effect both Ca-amphibole thermometers of Holland & Blundy (1994) were applied. Although the resulting temperatures agree within error, the edenite–richterite calibration is preferred because of the absence of quartz in some of the amphibole–plagioclase-bearing domains (Fig. 4e and f). Thermometry on matrix hornblende–plagioclase pairs for pressures of 0·54–0·86 GPa are 863–887°C.

The exsolution of cummingtonite from hornblende typically happens during cooling at low pressures. Oba & Nicholls (1986) showed that high-grade hornblende with a CaO content of >3·4% exsolves cummingtonite at temperatures below 700°C.

Zircon geochronology

Felsic granulite Z7-14-5

A total of 29 analyses of 15 zircon grains were performed by SIMS to determine U and Pb isotope compositions (Table 5). All grains are large and isometric (~0·5 mm diameter) and show sector and oscillatory zoning (Fig. 12a–c). They are round and multifaceted

Table 5: SIMS U–Pb zircon dating results

Sample Grain no.	[U] ($\mu g\ g^{-1}$)	[Th] ($\mu g\ g^{-1}$)	[Pb*] ($\mu g\ g^{-1}$)	[HfO_2] (wt %)	Th/U atomic	Pb_c (%)	$^{206}Pb/^{238}U$ (2σ)	$^{207}Pb/^{206}Pb$ (2σ)	$^{207}Pb/^{235}U$ (2σ)	$^{206}Pb/^{238}U$ age (Ma)	$^{207}Pb/^{235}U$ age (Ma)	Disc. (%)
Sample Z7-14-5												
29a	188	91	19	1·23	0·49	2·30	0·0774 (5)	0·0649 (25)	0·629 (9)	480·5 (3·2)	495·5 (5·5)	3·1
35c	379	57	34	1·20	0·15	1·41	0·0801 (6)	0·0591 (30)	0·617 (6)	496·5 (3·4)	488·0 (3·5)	–1·7
23c	202	43	20	0·91	0·22	2·00	0·0817 (5)	0·0619 (38)	0·637 (6)	506·0 (3·1)	500·5 (3·6)	–1·1
Concordia age: 493·7 ± 7·4 Ma (MSWD = 0·28; p.o.c. = 0·97; $n = 3$)												
36b	184	62	19	1·30	0·34	0·40	0·0885 (3)	0·0609 (34)	0·711 (4)	546·5 (1·6)	545·6 (2·6)	–0·2
23b	174	39	17	1·36	0·22	0·37	0·0876 (2)	0·0589 (3)	0·698 (4)	541·2 (1·4)	537·4 (2·3)	–0·7
29b	171	99	19	1·24	0·58	0·76	0·0879 (2)	0·0602 (4)	0·700 (6)	543·3 (1·3)	539·0 (3·6)	–0·8
29c	396	42	38	1·36	0·11	0·77	0·0872 (3)	0·0604 (1)	0·710 (12)	539·1 (1·6)	545·0 (7·1)	–0·9
Concordia age: 542·3 ± 2·8 Ma (MSWD = 1·7; p.o.c. = 0·38; $n = 4$)												
1b	190	94	21	1·30	0·49	0·36	0·0895 (4)	0·0611 (2)	0·735 (11)	552·7 (2·5)	559·7 (6·3)	1·3
23a	112	25	11	1·35	0·22	0·39	0·0898 (5)	0·0599 (2)	0·725 (11)	554·6 (2·7)	553·7 (6·7)	–0·2
4b	219	57	22	1·19	0·26	0·15	0·0901 (1)	0·0599 (12)	0·734 (9)	556·1 (0·7)	558·6 (5·3)	0·5
Concordia age: 555·8 ± 2·8 Ma (MSWD = 0·54; p.o.c. = 0·46; $n = 3$)												
7	270	132	30	1·21	0·49	0·29	0·0926 (3)	0·0598 (3)	0·750 (8)	571·1 (1·8)	568·4 (4·7)	–0·5
9b	118	61	13	1·27	0·52	0·37	0·0920 (7)	0·0593 (3)	0·752 (7)	567·1 (4·1)	569·2 (4·1)	0·4
32a	172	93	19	1·21	0·54	0·34	0·0922 (6)	0·0602 (3)	0·749 (7)	568·4 (3·6)	567·7 (4·2)	–0·1
17b	161	72	18	1·36	0·45	0·42	0·0932 (5)	0·0598 (3)	0·749 (7)	574·5 (3·1)	567·6 (3·9)	–1·2
5	236	70	25	1·46	0·30	0·66	0·0922 (2)	0·0617 (29)	0·752 (5)	568·4 (0·9)	569·4 (2·6)	0·2
32b	103	51	11	1·28	0·49	0·39	0·0921 (6)	0·0601 (3)	0·745 (7)	568·2 (3·7)	565·4 (4·3)	–0·5
33	131	60	14	1·27	0·46	0·46	0·0920 (5)	0·0601 (2)	0·742 (7)	567·2 (3·2)	563·3 (4·4)	–0·7
34a	281	118	30	1·24	0·42	0·37	0·0921 (6)	0·0603 (2)	0·749 (11)	567·7 (3·8)	567·6 (6·3)	0·0
34b	145	78	16	1·28	0·54	0·20	0·0909 (9)	0·0601 (2)	0·745 (13)	561·0 (5·3)	565·1 (7·3)	0·7
35a	291	171	33	1·23	0·59	0·40	0·0933 (8)	0·0610 (1)	0·765 (12)	575·2 (4·8)	576·7 (6·9)	0·3
35b	225	58	23	1·21	0·26	0·18	0·0933 (3)	0·0601 (28)	0·764 (6)	575·1 (1·7)	576·4 (3·7)	0·2
36a	147	62	16	1·37	0·42	0·42	0·0925 (9)	0·0597 (3)	0·742 (10)	570·4 (5·3)	563·6 (5·9)	–1·2
37a	188	98	21	1·22	0·52	0·29	0·0929 (8)	0·0599 (3)	0·754 (9)	572·9 (4·8)	570·5 (5·2)	–0·4
37b	150	60	16	1·28	0·40	0·37	0·0915 (13)	0·0607 (3)	0·749 (10)	564·2 (7·9)	567·6 (5·9)	0·6
Concordia age: 569·7 ± 1·4 Ma (MSWD = 0·09; p.o.c. = 0·76; $n = 14$)												
39	117	62	14	1·30	0·53	0·39	0·0958 (8)	0·0606 (2)	0·779 (9)	589·9 (4·6)	585 (5·3)	–0·8
4a	239	58	26	1·22	0·24	0·34	0·0963 (1)	0·0607 (35)	0·787 (9)	592·7 (0·6)	589·5 (5·0)	–0·5
9a	n.d.	n.d.	n.d.	n.d.	n.d.	0·35	0·0953 (4)	0·0617 (4)	0·791 (7)	586·6 (2·4)	591·9 (4·0)	0·9
17a	204	67	23	1·40	0·33	0·53	0·0963 (0)	0·0614 (34)	0·786 (5)	592·8 (0·3)	588·8 (2·8)	–0·7
32c	225	61	25	1·28	0·27	0·66	0·0965 (2)	0·0628 (60)	0·797 (13)	594·0 (1·1)	595·2 (7·3)	0·2
Concordia age: 592·6 ± 2·1 Ma (MSWD = 0·95; p.o.c. = 0·65; $n = 5$)												
Sample Z7-15-2												
8b	253	37	25	1·34	0·15	0·58	0·0891 (12)	0·0604 (6)	0·719 (8)	550·1 (7·1)	549·9 (4·5)	0·0
Concordia age: 550·0 ± 8·5 Ma (MSWD = 0·0006; p.o.c. = 0·98; $n = 1$)												
4	322	56	33	0·98	0·17	0·35	0·0949 (7)	0·0599 (6)	0·766 (13)	584·3 (4·2)	577·2 (7·7)	–1·2
10	319	53	32	1·00	0·17	0·33	0·0916 (6)	0·0605 (4)	0·749 (7)	565·0 (3·8)	567·8 (4·1)	0·5
13	986	203	104	1·30	0·21	0·47	0·0945 (9)	0·0613 (5)	0·774 (7)	581·8 (5·2)	582·1 (4·0)	0·0
Concordia age: 575·8 ± 9·4 Ma (MSWD = 0·012; p.o.c. = 0·91; $n = 3$)												
8a	118	528	46	1·29	4·47	0·05	0·1629 (12)	0·0729 (2)	1·611 (7)	972·9 (6·5)	974·5 (2·9)	0·2
Concordia age: 973·6 ± 8·8 Ma (MSWD = 0·06; p.o.c. = 0·80; $n = 1$)												
Sample Z7-16-4												
1a	401	121	28	1·26	0·30	1·13	0·0599 (5)	0·0571 (32)	0·465 (6)	375·2 (3·0)	387·9 (3·9)	3·4
8	143	90	11	1·30	0·630	0·39	0·0600 (6)	0·0559 (47)	0·460 (8)	375·7 (3·8)	384·4 (5·3)	2·3
14	165	34	12	1·20	0·21	0·89	0·0608 (2)	0·0577 (27)	0·477 (10)	380·5 (0·9)	396·3 (7·0)	4·2
Concordia age: 379·7 ± 1·7 Ma (MSWD = 1·8; p.o.c. = 0·18; $n = 3$)												
1b	117	117	14	n.d.	1·00	1·91	0·0789 (3)	0·0631 (50)	0·624 (5)	489·8 (1·7)	492·5 (3·2)	0·5
6	66	98	8	1·00	1·48	0·09	0·0797 (3)	0·0570 (87)	0·623 (12)	494·2 (2·0)	492·0 (7·7)	–0·4
7	103	164	12	1·11	1·58	0·00	0·0782 (8)	0·0585 (61)	0·631 (5)	485·4 (5·0)	496·7 (3·4)	2·3
9	80	128	10	1·05	1·60	0·00	0·0790 (4)	0·0572 (56)	0·623 (8)	489·9 (2·3)	491·8 (4·9)	0·4
21	127	104	13	n.d.	0·82	0·10	0·0770 (15)	0·0614 (57)	0·625 (11)	478·0 (8·8)	492·9 (6·8)	3·1
Concordia age: 491·4 ± 4·3 Ma (MSWD = 0·40; p.o.c. = 0·52; $n = 5$)												
13	398	320	43	0·98	0·81	0·36	0·0836 (14)	0·0590 (21)	0·669 (10)	517·5 (8·6)	519·8 (5·9)	0·4
Concordia age: 517·5 ± 8·6 Ma (MSWD = 0·034; p.o.c. = 0·85; $n = 1$)												
20	219	36	23	n.d.	0·16	0·65	0·0911 (3)	0·0638 (74)	0·754 (9)	562·3 (1·7)	570·3 (5·3)	1·4
Concordia age: 562·0 ± 3·4 Ma (MSWD = 0·93; p.o.c. = 0·34; $n = 1$)												
Sample Z7-15-5												
32	244	13	21	1·34	0·05	0·01	0·0853 (6)	0·0571 (5)	0·672 (3)	527·9 (3·6)	521·7 (1·7)	–1·2
38b	174	74	17	1·30	0·43	0·07	0·0840 (8)	0·0578 (11)	0·667 (4)	519·8 (4·8)	518·7 (2·5)	–0·2
Concordia age: 521·2 ± 4·6 Ma (MSWD = 0·004; p.o.c. = 0·95; $n = 2$)												
18	100	59	11	1·04	0·59	0·12	0·0900 (10)	0·0575 (12)	0·709 (8)	555·4 (5·9)	544·2 (4·6)	–2·0
30	74	39	8	0·88	0·53	0·02	0·0869 (7)	0·0590 (11)	0·706 (3)	537·4 (4·4)	542·6 (2·1)	1·0
Concordia age: 541·9 ± 7·5 Ma (MSWD = 0·033; p.o.c. = 0·86; $n = 2$)												
3	153	14	15	1·34	0·09	0·10	0·0951 (7)	0·0568 (18)	0·748 (9)	585·6 (4·1)	567·1 (5·4)	–3·2
38	n.d.	n.d.	n.d.	n.d.	n.d.	0·07	0·0943 (7)	0·0580 (11)	0·750 (11)	580·8 (3·9)	568·4 (6·1)	–2·1
40a	120	22	12	1·14	0·18	0·10	0·0925 (10)	0·0595 (13)	0·755 (12)	570·3 (6·0)	571·0 (6·8)	0·1
40b	120	22	12	1·14	0·18	0·10	0·0934 (21)	0·0595 (13)	0·762 (10)	575·0 (12·0)	575·0 (5·7)	–0·1

(continued)

Table 5. Continued

Sample Grain no.	[U] (μg g^{-1})	[Th] (μg g^{-1})	[Pb*] (μg g^{-1})	[HfO_2] (wt %)	Th/U atomic	Pb_c (%)	$^{206}Pb/^{238}U$ (2σ)	$^{207}Pb/^{206}Pb$ (2σ)	$^{207}Pb/^{235}U$ (2σ)	$^{206}Pb/^{238}U$ age (Ma)	$^{207}Pb/^{235}U$ age (Ma)	Disc. (%)
41a	207	155	24	0·99	0·75	0·05	0·0909 (10)	0·0592 (12)	0·754 (9)	560·6 (6·1)	570·5 (5·0)	1·8
41b	207	155	24	0·99	0·75	0·05	0·0917 (10)	0·0592 (12)	0·746 (9)	565·6 (6·2)	565·8 (5·1)	0·0
Concordia age: 575·3 ± 5·6 Ma (MSWD = 0·82; p.o.c. = 0·65; *n* = 6)												
1	72	50	9	0·90	0·70	0·03	0·0950 (9)	0·0588 (20)	0·800 (10)	585·1 (5·0)	597 (11)	–1·9
12	166	43	20	1·09	0·26	0·04	0·1083 (6)	0·0597 (10)	0·924 (4)	662·8 (3·7)	664·5 (4·8)	–3·6
24	319	65	41	1·11	0·20	0·00	0·1178 (8)	0·0605 (58)	1·023 (17)	717·8 (4·4)	716 (17)	–4·1
39	155	56	30	1·08	0·36	0·20	0·1647 (18)	0·0765 (41)	1·636 (16)	983 (10)	984 (15)	0·1
Various ages and possibly discordant dates (*n* = 4)												
39b	89	77	21	1·18	0·86	0·10	0·1833 (28)	0·0772 (32)	1·906 (19)	1085 (15)	1083·0 (6·6)	–0·2
Concordia age: 1083 ± 12 Ma (MSWD = 1·12; p.o.c. = 0·29; *n* = 1)												

n.d., not determined; p.o.c. = probability of concordance.

(i.e. 'soccer-ball zircons'), a morphology that is typical for zircon from high-*T* metamorphic rocks (e.g. Harley & Kelly, 2007). Commonly, two to three distinct growth zones can be distinguished within a single grain (Fig. 12a–c). The majority of the grain cores make up the first growth zone and range from 100 to 300 μm in diameter. These core domains are all sector zoned, show resorption textures and are truncated by a second generation of zircon. A third growth zone can be distinguished in most grains and is generally made up by the outermost few micrometers of the rims. These domains are characterized by their particular brightness in CL images in comparison with the other two growth zones. In some grains the latter growth zone extends to almost 50 μm and was, hence, large enough to be analysed. Uranium concentrations in all domains range from 103 to 396 μg g^{-1} with Th/U ratios between 0·11 and 0·59 (median = 0·46). Discordance is less than 3% for all analyses.

Four distinct ages are recorded in zircon from this sample. The precision of dating of our secondary SIMS reference material (zircon Temora-2) is ~±1·3% (2SD). We therefore elect to present the weighted mean ages of the four age groups with an error of ±1·3% in cases where the standard deviation of the mean of the group is smaller than the precision of the secondary reference material (i.e. smaller than ±1·3%). The oldest group is defined by several anhedral, sector-zoned core domains (five analyses), which yielded a weighted mean age of 593 ± 8 Ma (Fig. 13a). The largest group of zircon domains (14 analyses) has a pooled concordia age of 570 ± 7 Ma (Fig. 13a). The third group is defined by seven analyses of rim domains and two core domains having a weighted mean age of 546 ± 7 Ma. Although indistinguishable on the basis of the geochronological data alone, trace element concentrations justify a subdivision of this group into domains with high Ti (30–38 μg g^{-1}; three grains) with a weighted mean age of 556 ± 7 Ma (Fig. 13a) and domains with lower Ti concentrations (13–20 μg g^{-1}; four analyses on two grains) that have a weighted mean age of 542 ± 7 Ma (Fig. 13a). The rim domains of three zircon grains gave an age of 494 ± 7 Ma (Fig. 13a).

Amphibolized mafic garnet granulite Z7-15-2

Zircon is rare in sample Z7-15-2 and only 15 grains could be recovered from 1·4 kg of crushed rock. Zircon grains are rounded, slightly ovoid and between 70 and 130 μm long. A total of six zircon grains had growth zones that were wide enough to be analysed for their U and Pb isotope compositions by SIMS (Table 5). Most of these zircon grains show sector zoning. Uranium concentrations range from 253 to 986 μg g^{-1} with Th/U ratios between 0·17 and 0·21. Discordance is less than 1·2% and the majority (four grains) have a weighted mean age of 576 ± 9 Ma. In one grain, the rim domain reveals an age of 550 ± 9 Ma (Fig. 13b).

A euhedral, oscillatory-zoned zircon core domain (Fig. 12d) differs from the main group of zircon grains with lower U concentrations of 118 μg g^{-1} and a significantly higher Th/U ratio of 4·47. The U/Pb isotope composition yields an age of 974 ± 9 Ma (Fig. 13c).

Rootshorga paragneiss sample Z7-15-5

A total of 15 analyses of 14 zircon grains were performed by SIMS to determine U and Pb isotope compositions. Uranium concentrations range from 72 to 320 μg g^{-1} with Th/U ratios between 0·05 and 0·86 (median = 0·36). Discordance is less than 3·2% for all analyses assigned to one of the age groups, whereas four analyses are interpreted to represent Pb loss or mixed ages. Several groups of zircon grains can be distinguished by their U–Pb isotope compositions (Table 5).

The dominant group of zircon grains (six analyses) has a pooled concordia age of 575 ± 7 Ma (Fig. 13d). Zircon grains of this group show mainly oscillatory internal zonation patterns. Two oscillatory-zoned zircon grains with a pooled concordia age of 542 ± 8 Ma define a second group (Fig. 13d). A third group consists of two zircon domains that show no internal zonation pattern. This group has a pooled concordia age of 521 ± 7 Ma (Fig. 13d).

Several single zircon grains show ages greater than 600 Ma. The oscillatory-zoned core domain of one grain yields a Grenvillian age of 1083 ± 12 Ma (Fig. 13e). The rim analysis of the same grain resulted in an age that we interpret as discordant, as did two other analyses. One oscillatory zircon grain has an apparent age of

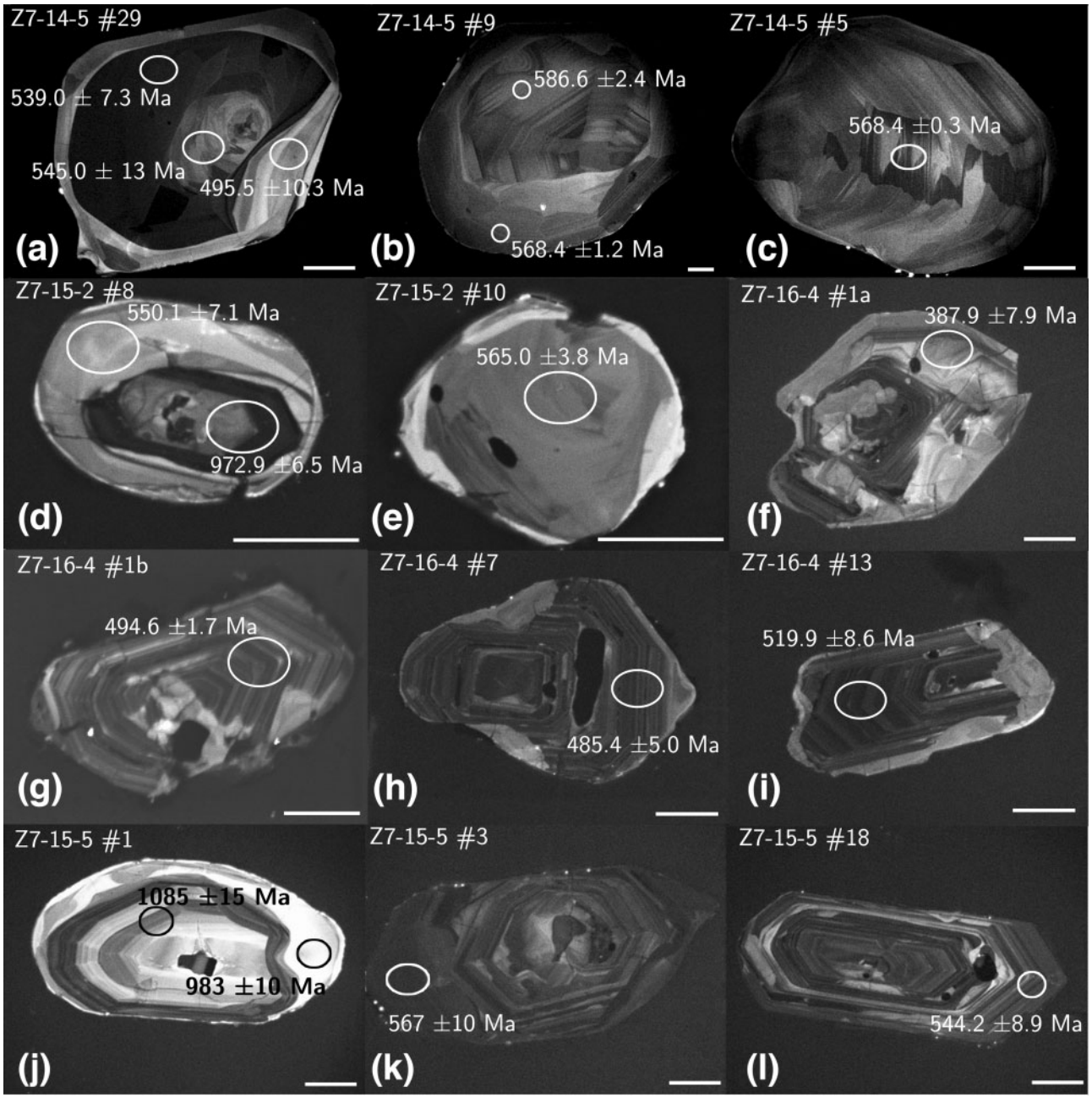

Fig. 12. Cathodoluminescence images of zircon grains. The scale bar in each image corresponds to 50 μm. SIMS analysis spots for U–Pb dating are marked by white ovals and $^{238}U/^{206}Pb$ ages are given. (a–c) Felsic granulite sample Z7-14-5 shows large grains that display oscillatory and sector zonation in their cores. Cores show truncation and embayments, and overgrowths by rims with high CL activity. (d, e) Amphibolized mafic garnet granulite Z7-15-2 shows mostly small grains with weak zonation. One grain displays an old prismatic, bi-pyramidal core with variable CL activity overgrown by a brighter rim of Late Neoproterozoic age. (f–i) Brattskarvet granite sample Z7-16-4 shows large grains with oscillatory zonation typical for igneous zircon; these show irregular partial replacement by younger zones with nebulous and patchy zonation. (j–l) Rootshorga paragneiss sample Z7-15-5 shows large, oscillatory and more complexly zoned grains.

608 ± 13 Ma (Fig. 13d). These four grain analyses are consistent with a discordia with upper and lower intercepts at the two concordant age groups of 1083 Ma and 575 Ma, respectively (Fig. 13e). However, the uncertainties do not allow a distinction between the analyses lying on the discordia or representing a range of concordant zircon growth ages (Fig. 13d and e).

Brattskarvet granite sample Z7-16-4

A total of 11 zircon grains were analysed for their U and Pb isotope compositions by SIMS. One analysis was discarded, because it is more than 10% discordant. The remaining analyses are less than 5% discordant. The main group of zircon grains (five analyses) is defined by oscillatory zonation and sub- to euhedral grain shapes.

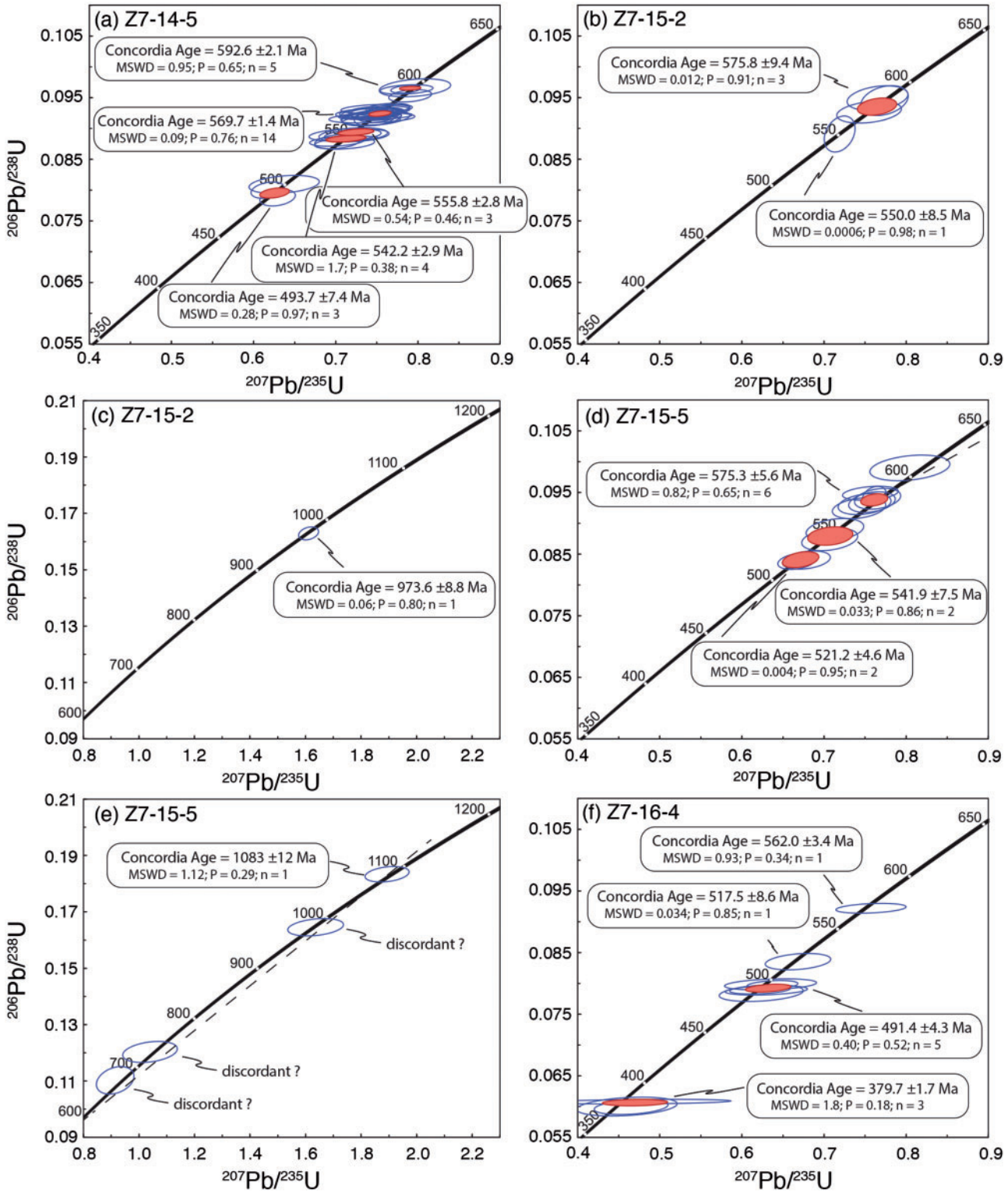

Fig. 13. Concordia diagrams for zircon. Open ellipses are single analyses; filled red ellipses mark pooled concordia ages. (a) Five zircon age groups were distinguished in felsic granulite sample Z7-14-5 based on a combination of pooled concordia ages and Ti concentrations. (b, c) Amphibolized mafic garnet granulite sample Z7-15-2 for which three ages were distinguished: two metamorphic ages and one older core that is displayed in Fig. 12d. (d, e) Zircon in paragneiss sample Z7-15-5 shows several groups of Neoproterozoic metamorphic growth zones, as well as metamorphic zircon growth during the Mesoproterozoic event, with a number of intermediate ages that are interpreted as discordant data. (f) Zircon in the Brattskarvet granite sample Z7-16-4 shows a dominant population of concordant grains that is interpreted to represent the intrusion age, some inherited grains and some younger ages determined on nebulous replacement zones (see Fig 12f).

The U concentrations range from 66 to 127 μg g^{-1} with Th/U ratios of 0·82 to 1·60 (median = 1·48). The group has a pooled concordia age of 491 ± 6 Ma (Fig. 13f). We infer these zircon grains to represent the intrusion age of the granite.

A second group is defined by three zircon analyses. The measured domains do not show any systematic internal zonation and the boundaries between these domains and the rest of the grains are irregularly shaped. These zircon domains have higher U concentrations between 143 and 401 μg g^{-1} with Th/U ratios that range from 0·21 to 0·63 (median = 0·30). The weighted mean age is 380 ± 5 Ma (Fig. 13f). These grains probably represent a younger metasomatic event that is unrelated to the Pan-African orogeny.

In addition, two single zircon grains have U concentrations of 398 μg g^{-1} and 219 μg g^{-1}, Th/U ratios of 0·81 and 0·16 and yield ages of 518 ± 9 Ma and 562 ± 3 Ma, respectively (Fig. 13f). These grains are interpreted as inherited grains assimilated from the metamorphic country rock.

Monazite geochronology

Monazite grains in sample Z7-14-5 were analysed for chemical age determination. A total of 347 points in 80 chemically defined domains of 36 monazite grains were analysed. Images of all grains are provided in Supplementary Data Figs S4 and S5. Out of the 36 grains, 11 grains were analysed *in situ* in thin sections and 25 grains picked from the heavy-mineral separate were analysed in a polished grain mount. Three petrographic groups are distinguished among these domains (Table 6): (1) inclusions in garnet; (2) cores of grains and homogeneous grains; (3) grain rims, replacement zones, patches and veins. Garnet inclusions (Group 1) show the oldest ages (563 to >600 Ma; Fig. 14). It should be noted that chemical dating does not allow for an evaluation of concordancy, nor the identification of partial Pb loss. Ages that significantly predate the UHT metamorphic event at *c.* 570 Ma may, therefore, represent partial Pb loss and (discordant) resetting of older monazite grains (e.g. Grenville-age monazite) during the Pan-African UHT metamorphic event. However, the monazite domains in this age group (Group 3) are chemically distinct with high Ca, Th and U contents, and significant Y (Fig. 15). They show elevated brabantite and huttonite components (Fig. 15a and b). The >600 Ma grain (Mnz_1; Fig. 16a) is associated with plagioclase, biotite and Zn-bearing hercynite. Grain Mnz_1 is Th-rich and shows a brabantite-type substitution (Ca + Th = 2REE) increasing from core to rim (Fig. 15a).

Monazite grain cores (Group 2) show a large range of ages from *c.* 580 Ma to ≤450 Ma. No single growth events can be distinguished within this group, neither based on the age distribution, nor on the basis of chemical composition. The observed age range and skew to younger ages may again represent diffusive Pb loss instead of monazite crystallization over more than 130 Myr. However, the most dominant peak in the probability density function of this group is at 539 Ma, with most grain domains ranging from *c.* 560 Ma to 520 Ma (Fig. 14). There also is a clear chemical evolution with age, with Ca and Th (brabantite and huttonite components) continuously decreasing from 560 Ma to≤450 Ma (Fig. 15f and g). The oldest domains in this group (*c.* 580 Ma) were observed in monazite associated with rutile, quartz, apatite, biotite, Zn-bearing hercynite and plagioclase.

The third group of monazite domains forms rims on Group 2 grains, or irregular veins cutting these grains, or replacement zones and patches with sharp contacts to the pre-existing grains that are interpreted as solution–reprecipitation fronts (Fig. 16). These zones are generally lower in Ca and Th than their host grains (Fig. 16b, c and e). Both brabantite- and huttonite-type substitutions are evident and the domains in this group continue the trend of decreasing Ca and Th with younger age (Fig. 15f and g). The oldest ages in this petrographic group are *c.* 550 Ma, but the dominant peak in the probability density function is at 474 Ma, with most analyses between 520 and 420 Ma (Fig. 14). Most domains in this group are as low in Y as the core domains, with the exception of a subset of analysed domains with ages *c.* 474 Ma that show strongly elevated Y contents (Fig. 15h). These domains occur in grains close to garnet porphyroblasts that show dissolution textures.

Elevated U contents (>0·4%) were found only in monazite inclusions in garnet. These may predate the major growth phase of zircon in this rock. Elevated Y contents in monazite were observed in garnet inclusions and the oldest cores of the matrix monazite, as well as monazite that formed very late at *c.* 474 Ma (Fig. 15h).

DISCUSSION

Pressure–temperature path

No metamorphic conditions could be assigned to the Late Mesoproterozoic metamorphism (M_1) from the investigated samples. However, the Neoproterozoic–Cambrian evolution of the area is well documented in the investigated granulites, and six stages in the Pan-African metamorphic evolution can be distinguished. These are summarized in Fig. 17 and describe a clockwise *P–T* path. The earliest stage (Stage M_{2a}) is recorded in the rutile-bearing low-Ca cores of the largest garnet grains in felsic granulite Z7-14-5 with *P–T* conditions of 786 ± 9°C at 0·95 GPa. This stage was followed by loading to a pressure of 1·45 GPa with only moderate heating by ~60°C to 844 ± 44°C (Stage M_{2b}), as recorded by rutile inclusions in high-Ca garnet zones. This increase in pressure by 0·5 GPa is equivalent to an increase in depth of about 18 km, or an increase from a depth of ~35 km to ~53 km (calculations based on the

Table 6: Weighted mean age of monazite domains in sample Z7-14-5

Grain no.	*n*	Age (Ma)	2σ	MSWD	Texture and grain domain	Chemical characteristic
Monazite inclusions in garnet						
Mnz_1	2	644	9	0·3	core	m Si, vh Ca, m-h Y
Mnz_1	4	607	13	0·096	core	l-m Si, h Ca, l-m Y
Mnz_1	4	621	14	0·65	rim patch	l Si, h Ca, m-h Y
Mnz_9	2	563	20	0·082	core	vl Si, h Ca, m Y
Mnz_9	3	571	19	0·71	core	vl Si, m Ca, m Y
Mnz_35	10	585	11	0·07	core	vl Si, h Ca, m Y
Matrix monazite, grain cores and homogeneous grains						
Mnz_2	4	513	43	0·2	core	l Si, l Ca, l Y
Mnz_3	5	520	57	0·06	core	vl Si, vl Ca, l-m Y
Mnz_3	2	468	84	0·33	core	vl Si, vl Ca, m-h Y
Mnz_4	4	447	73	0·077	homogeneous	vl Si, vl Ca, l Y
Mnz_5	3	445	48	0·0117	near Grt	vl Si, l Ca, l-m Y
Mnz_6	3	422	100	0·067	homogeneous	vl Si, vl Ca, l Y
Mnz_7	3	586	75	0·77	core	vl Si, vl Ca, l Y
Mnz_7	5	571	50	0·61	core	vl Si, l Ca, l Y
Mnz_7	3	481	68	0·0021	core	vl Si, vl Ca, l Y
Mnz_8	5	453	75	0·091	core	vl Si, vl Ca, l-m Y
Mnz_8	4	462	65	0·067	core	vl Si, vl Ca, l Y
Mnz_8	1	479	168		core	vl Si, vl Ca, l Y
Mnz_10	2	488	78	0·053	homogeneous	vl Si, l Ca, l-m Y
Mnz_11	6	523	18	0·024	core	m Si, l-m Ca, l Y
Mnz_12	8	560	11	0·18	core	m Si, m Ca, l Y
Mnz_12	5	554	17	0·16	core	m Si, m Ca, vl Y
Mnz_13	10	506	20	0·13	core	l Si, l Ca, l Y
Mnz_14	5	571	17	0·116	core	m Si, m Ca, vl Y
Mnz_14	4	579	17	0·3	core	m Si, m Ca, vl Y
Mnz_15	6	552	20	0·032	core	l Si, m Ca, m Y
Mnz_15	11	545	14	0·13	core	l Si, m Ca, m Y
Mnz_16	11	585·8	9·7	0·25	core	m Si, m Ca, l Y
Mnz_17	3	547	23	0·89	core	m Si, m Ca, l Y
Mnz_17	4	529	25	0·22	core	l Si, l-m Ca, vl Y
Mnz_18	4	530	17	0·18	core	m Si, m Ca, l Y
Mnz_18	2	434	44	0·034	core	l Si, l Ca, vl Y
Mnz_19	7	498	25	0·25	core	l Si, l-m Ca, l Y
Mnz_20	6	540	14	0·78	core	m Si, m Ca, l Y
Mnz_20	3	504	25	0·36	core	l Si, m Ca, l Y
Mnz_21	2	598	24	0·051	core	m Si, m Ca, l Y
Mnz_21	2	536	43	0·29	core	l Si, l-m Ca, l Y
Mnz_22	4	531	26	0·6	core	l-m Si, l-m Ca, l Y
Mnz_23	6	540	14	0·44	core	m Si, m Ca, l Y
Mnz_24	8	529	12	0·43	core	m Si, m Ca, vl Y
Mnz_24	5	514	18	0·114	core	l Si, m Ca, l Y
Mnz_25	10	474	21	0·35	core	l Si, l-m Ca, l Y
Mnz_26	4	498	33	0·18	core	l Si, l Ca, vl Y
Mnz_27	5	534	15	0·45	core	m Si, m Ca, l Y
Mnz_28	3	565	21	0·36	core	m Si, m Ca, vl Y
Mnz_28	1	545	43		core	l Si, m Ca, l Y
Mnz_29	4	553	18	0·39	core	m Si, m Ca, l Y
Mnz_29	2	553	38	0·5	core	l Si, l-m Ca, vl Y
Mnz_30	7	520	25	0·33	core	l Si, l-m Ca, l Y
Mnz_31	12	540	9·4	0·71	core	m Si, m Ca, l Y
Mnz_32	6	558	15	0·78	core	m Si, m Ca, l Y
Mnz_33	8	425	21	0·19	core	l Si, l-m Ca, l Y
Mnz_34	4	470	32	0·39	core	l Si, l-m Ca, l Y
Mnz_36	21	546	14	0·106	core	l Si, l-m Ca, l Y
Matrix monazite rims and veins						
Mnz_2	3	476	45	0·18	rim	vl Si, l Ca, vh Y
Mnz_2	4	467	50	0·022	rim	vl Si, l Ca, vh Y
Mnz_11	7	444	23	0·036	rim	vl Si, l-m Ca, h Y
Mnz_11	2	437	44	0·0077	rim	l Si, l Ca, h Y
Mnz_11	5	483	28	0·028	patch	l Si, l-m Ca, vl Y
Mnz_11	9	407	32	0·7	large rim patch	vl Si, l Ca, vl Y
Mnz_12	4	470	32	0·104	rim patch	l Si, l-m Ca, l Y
Mnz_13	5	452	39	0·068	thick rim	l Si, l Ca, l Y
Mnz_14	2	510	38	0·023	rim	l-m Si, l-m Ca, vl Y
Mnz_14	2	514	49	0·31	outer rim	vl Si, l-m Ca, l Y
Mnz_15	2	462	45	0·0018	vein	l Si, l-m Ca, l Y
Mnz_15	2	463	47	0·13	vein	vl Si, l-m Ca, l Y

(continued)

Table 6. Continued

Grain no.	*n*	Age (Ma)	2σ	MSWD	Texture and grain domain	Chemical characteristic
Mnz_15	3	416	48	0·057	rim/vein	vl Si,l Ca, l Y
Mnz_16	5	553	17	0·13	vein	l-m Si, m Ca, l Y
Mnz_16	2	505	31	0·094	vein	l Si, m Ca, l Y
Mnz_17	1	549	54		rim	vl Si, m Ca, l Y
Mnz_22	1	552	89		rim	vl Si, l Ca, l Y
Mnz_23	4	482	24	0·3	rim	vl Si, m Ca, l Y
Mnz_25	3	451	43	0·026	rim	vl Si, l-m Ca, l Y
Mnz_26	3	491	46	0·46	rim	vl Si, l-m Ca, l Y
Mnz_27	4	476	27	0·97	rim	vl Si, m Ca, l Y
Mnz_28	2	524	52	0·18	vein	vl Si, l-m Ca, l Y
Mnz_30	2	458	65	0·013	rim	vl Si, l Ca, l-m Y
Mnz_31	2	488	44		rim	vl Si, l-m Ca, l Y
Mnz_31	1	462	62		outer rim	vl Si, l-m Ca, l-m Y
Mnz_32	2	476	43	0·15	rim	vl Si, l-m Ca, l Y
Mnz_34	2	454	54	0·21	vein/light patch	vl Si, l-m Ca, l Y

n, number of analyses; vl, very low; l, low; m, medium; h, high.

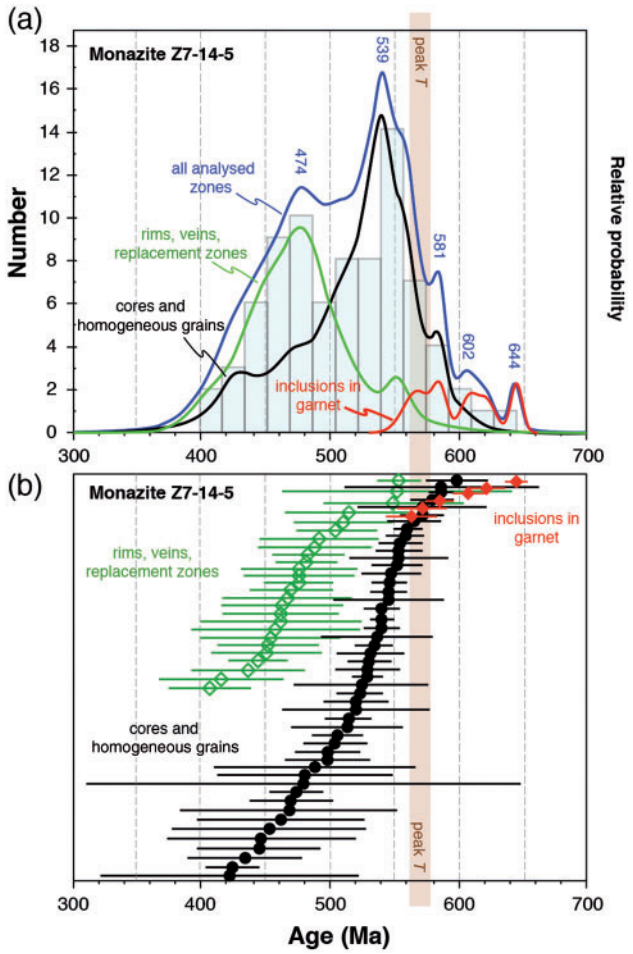

Fig. 14. Monazite age dating results for felsic granulite sample Z7-14-5. (a) Probability density plots of all analysed samples (blue), inclusions in garnet (red), cores of grains and homogeneous grains (black), and grain rims, replacement zones and veins (green). Also shown is a histogram of all analyses, and the age of the metamorphic temperature peak as determined from zircon in this sample. (b) Analyses with 2σ error bars for all analysed grains. Each datum point is based on up to 21 EPMA analyses. The colours are the same as in (a).

assumption of lithostatic pressure and an average crustal density of 2800 kg m^{-3}).

Loading was followed by isobaric heating with a temperature increase of ~85°C to 929 ± 23°C (Stage M_{2c}), as recorded by the high-Zr rutile included in Ca-rich garnet in felsic granulite sample Z7-14-5. The apparent geothermal gradient changes from a relatively hot Stage M_{2a} geotherm of 22·7°C km^{-1} to a much cooler M_{2b} geotherm of 16·0°C km^{-1} during the loading event followed by isobaric heating to a gradient of 17·6°C km^{-1} in Stage M_{2c}. This high-*P*–*T* stage (M_{2c}) is also reflected by rutile and garnet relics in mafic sample Z7-15-2, which are interpreted as part of the peak metamorphic assemblage garnet + clinopyroxene (?) + plagioclase + quartz + rutile. However, this stage could not be quantified in that sample.

The metamorphic peak stage (Stage M_{2c}) was followed by near-isothermal decompression to high-*T* and medium-crustal pressure conditions followed by subsequent near-isobaric cooling. The high-*T*–low-*P* stage is documented in mafic sample Z7-15-2 in the form of orthopyroxene + plagioclase symplectites replacing garnet, and in hornblende–plagioclase pairs that document rehydration at high temperatures. Orthopyroxene in the symplectites most probably formed during decompression between *c.* 0·9 and 0·6 GPa at temperatures in excess of 850°C, as recorded by Al-in-orthopyroxene thermometry. Rehydration and the formation of hornblende and cummingtonite in some domains of this rock occurred at similarly high temperatures, as recorded by hornblende–plagioclase thermometry. Hornblende subsequently exsolved cummingtonite lamellae upon cooling.

An initial high-pressure stage for the Rootshorga Formation was previously suggested by several researchers (Groenewald & Hunter, 1991; Grantham *et al.*, 1995; Board *et al.*, 2005), although reliable estimates for both peak pressures and temperatures were not made. It was also uncertain whether this high-*P* event occurred during the Neoproterozoic or already during the

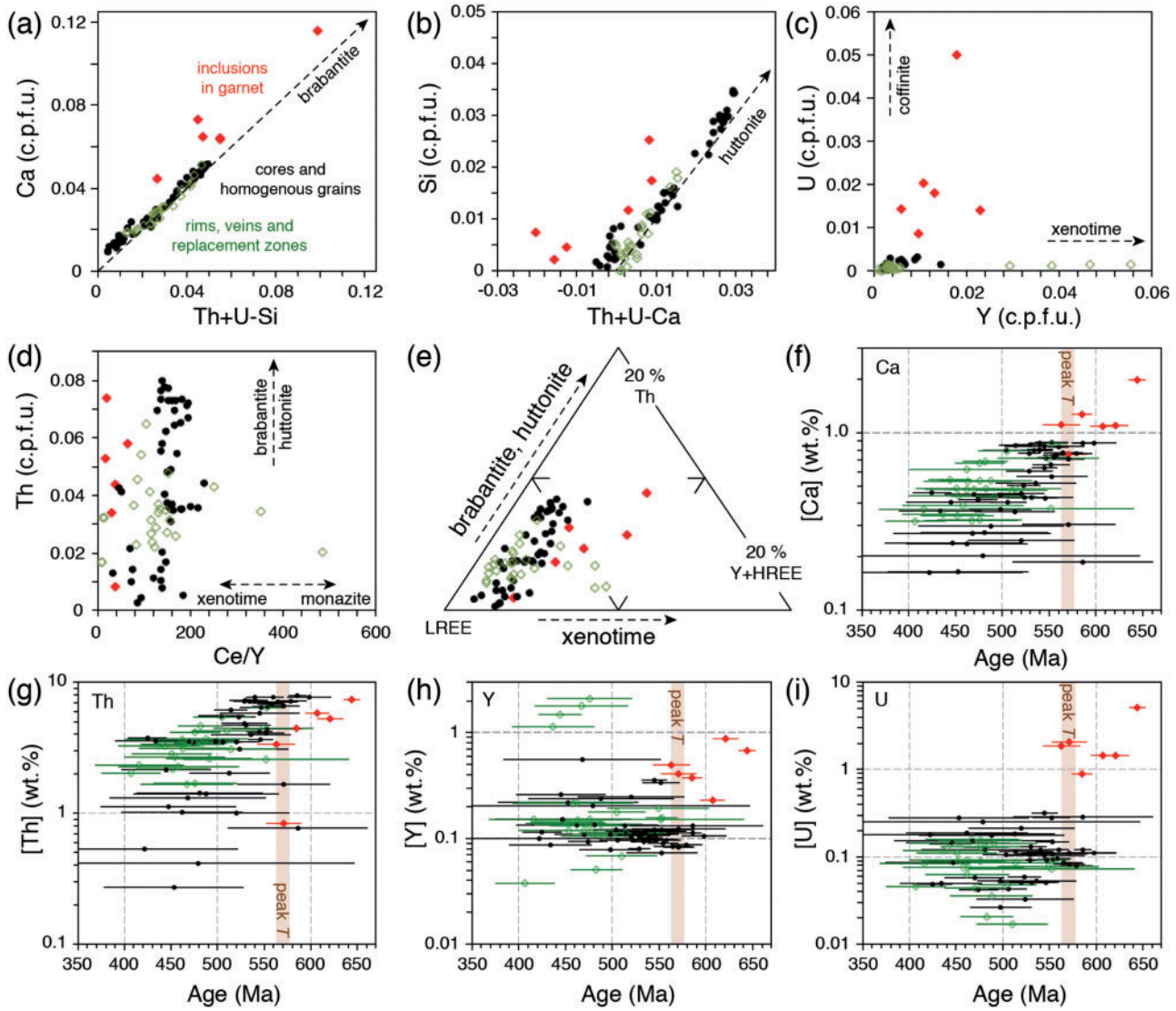

Fig. 15. Chemical variation of monazite in sample Z7-14-5. (a) Brabantite-type (2REE = Ca + Th) substitution. (b) Huttonite-type (REE + P = Th + Si) substitution. The garnet-hosted monazite grains deviate from both substitution trends and show Ca enrichment. (c) U vs Y plot showing U and Y enrichments in the garnet inclusions and Y enrichment in some rims. (d) Th vs Ce/Y. (e) Ternary plot showing REE and Th variations. (f–i) Minor element abundances vs age. The vertical bar marks the age of the metamorphic temperature peak as determined from zircon in this sample. A continuous decrease in Ca (f) and Th (g) with age is observed. (h) Y enrichment is observed in the oldest age groups and in some of the *c.* 474 Ma matrix monazite rims. (i) High U contents are observed only in garnet inclusions. All data are given in the Supplementary Data tables, and images of all analysed monazite grains are provided in Supplementary Data Figs S4 and S5.

Mesoproterozoic orogeny. The metamorphic peak conditions estimated for the rocks investigated here correspond to the eclogite–high-pressure granulite facies (E–HPG) as defined by Brown (2007), which is typical for collisional orogens in the Proterozoic–Cambrian eras (Brown, 2007). Despite the ultrahigh temperatures that these samples experienced, they record a moderate geothermal gradient of 17·6°C km^{-1} for the E–HPG stage. The prograde path records a period of loading at the onset of high-grade metamorphism from *c.* 35 km to 53 km depth. This suggests that the rocks had been located at or near the base of continental crust of normal thickness (i.e. 35 km), before they were buried by a further ~18 km, followed by heating.

Near-isothermal decompression from Stage M_{2c} to M_{2d} is best recorded in the mafic sample. Metamorphic conditions preserved in garnet breakdown products in mafic sample Z7-15-2 correspond to temperatures up to 887°C at 0·54–0·86 GPa, recorded by Al-in-orthopyroxene, GOPS and hornblende–plagioclase thermobarometry. Similar *P–T* conditions of 850–880°C at 0·9–1·1 GPa were obtained by Groenewald & Hunter (1991). This high-grade stage has often been interpreted to be of Grenvillian age (e.g. Board *et al.*, 2005), but evidence for this age interpretation for these samples was always circumstantial at best. We thus tentatively assume that the study by Groenewald & Hunter (1991) also describes the Pan-African Stage M_{2d}. Stage M_{2e} is

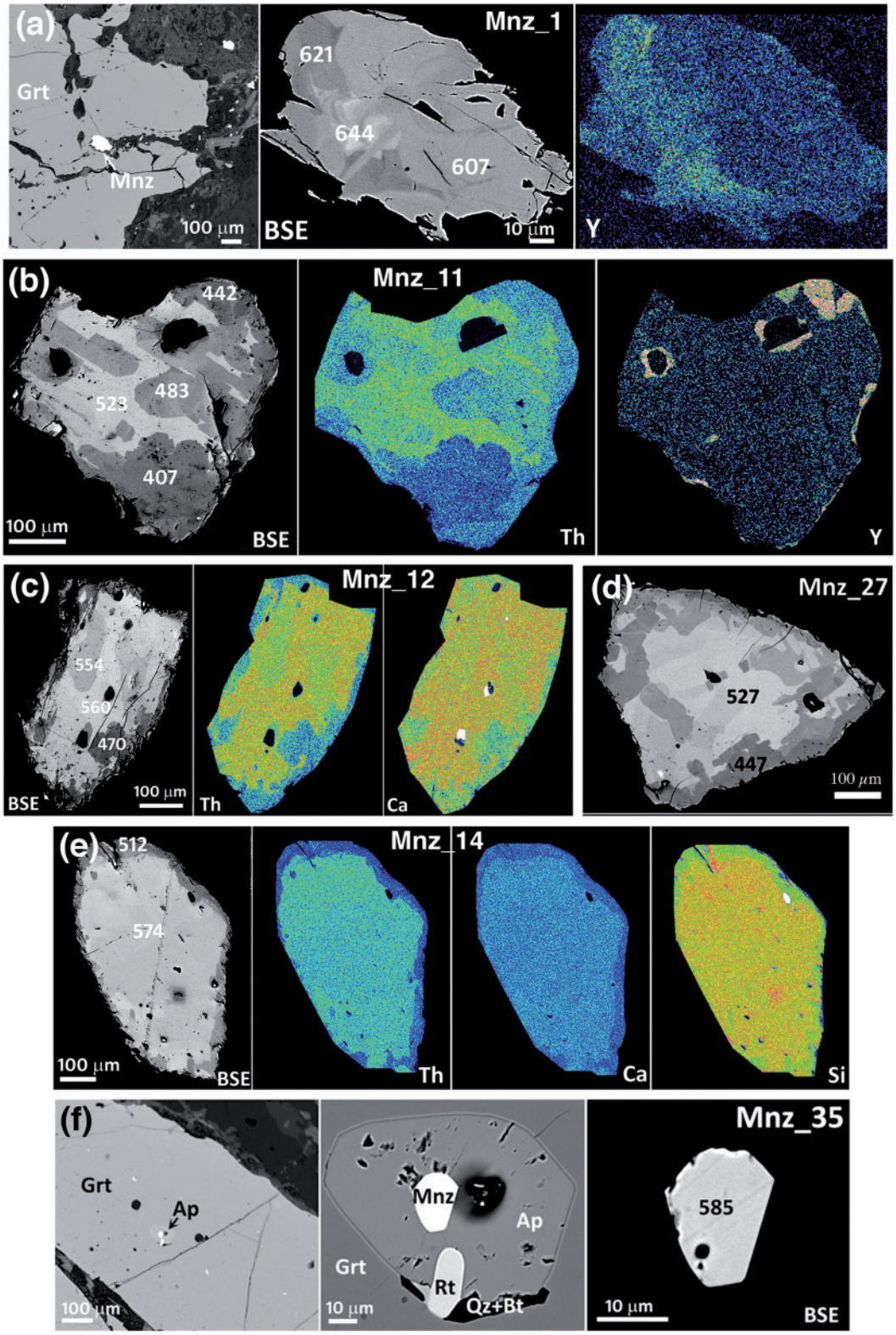

Fig. 16. Back-scattered electron (BSE) images and X-ray maps (Y, Ca and Th) of monazite grains in felsic granulite sample Z7-14-5. (a) Three panels showing Mnz_1 in a fracture inside garnet; (b–d) grains Mnz_11 (three panels), Mnz_12 (three panels) and Mnz_27 showing solution–reprecipitation zones that are younger than the cores of the grains and show various lower levels of Th. Some of these zones are enriched in Y. (e) Low-Ca–Th–Si rim on grain Mnz_14. (f) Grain Mnz_35 (three panels) included in apatite associated with rutile, quartz and biotite, all included in garnet. The mineral abbreviations are as given by Whitney & Evans (2010). The numbers on the BSE images represent weighted-mean ages in Ma of each domain (uncertainties in the ages are given in Table 6). Images of all analysed monazite grains are provided in Supplementary Data Figs S4 and S5.

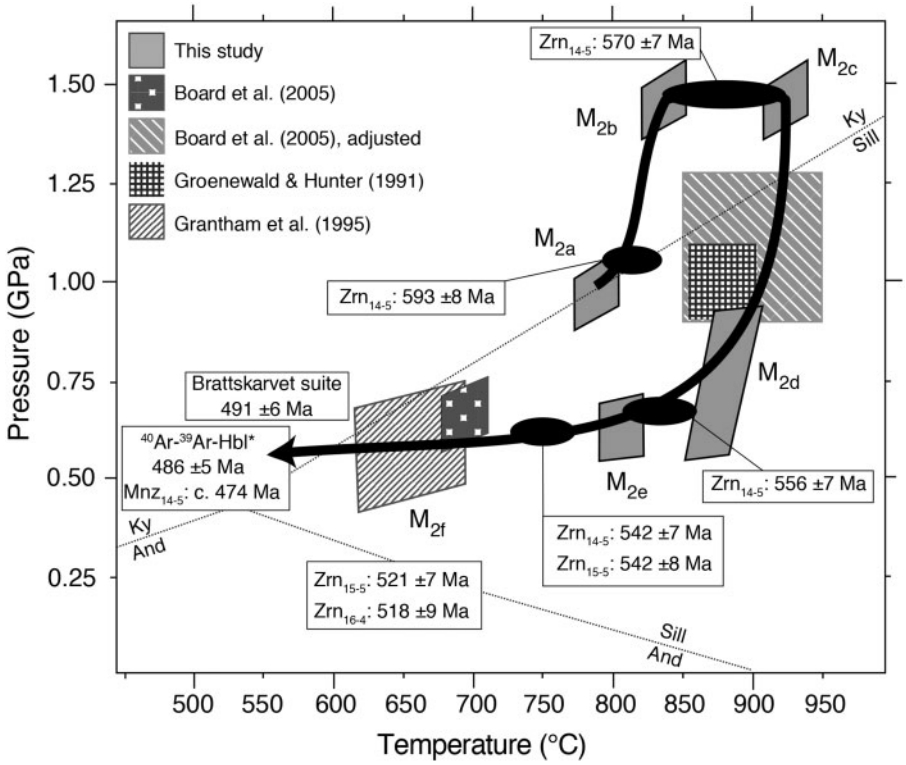

Fig. 17. Summary of the *P–T* evolution with age dates of various stages for felsic granulite sample Z7-14-5 and amphibolized mafic garnet granulite sample Z7-15-2. Peak conditions were 929 ± 23°C at 1·45 GPa. Also shown are *P–T* estimates from published studies on rocks from the H.U. Sverdrupfjella and a field of *P–T* conditions adjusted for low fluid activities from Board *et al.* (2005). The latter are preferred here over the medium-*T*, high-*P* conditions favoured by Board *et al.* (2005). *Hornblende Ar–Ar age (486 ± 5 Ma) from Board *et al.* (2005).

constrained in felsic granulite sample Z7-14-5 by the partial equilibration of garnet to very low Ca contents and pyrope contents of 23–25% (corresponding to 800–820°C at low pressures), the formation of cordierite + sillimanite + ilmenite assemblages, and the biotite-in reaction at *c.* 800°C and 0·65 ± 0·1 GPa (Fig. 9). The evolution from Stage M_{2d} to M_{2e} is consistent with the observations of near-isobaric cooling by Groenewald & Hunter (1991).

The samples studied by Grantham *et al.* (1995) and Board *et al.* (2005) consistently record amphibolite-facies conditions around 675°C and 0·7 GPa, which are referred to here as Stage M_{2f}. Formation of muscovite in Z7-14-5 may be related to this metamorphic stage, but no attempt was made here to determine *P–T* conditions for this stage.

Most of the previously published data are in good agreement with different stages of the *P–T* path presented in this study. Nevertheless, Board *et al.* (2005) reported a *P–T* path stage at ~750°C and 1·0 GPa for garnet–clinopyroxene-bearing mafic boudins in the Rootshorga paragneiss from a locality ~60 km SW of Brattskarvet (just off the map in Fig. 1b). Such *P–T* conditions deviate from the metamorphic evolution path determined in this study. The origin of this discrepancy may be diverse, such as that the mineral assemblages used for geothermobarometry do not record temperatures and pressures from the same stage, or that the rocks represent different structural units that underwent different *P–T* paths. To constrain metamorphic conditions, Board *et al.* (2005) applied the average *P–T* method of Powell & Holland (1994). They obtained average *P–T* estimates of ~900°C and 1·2 GPa for dry conditions, and discredited them as 'geologically unreasonable'. Thus, they assumed fluid presence, which lowered resulting temperature estimates to ~750°C. However, the peak metamorphic mineral paragenesis described in those metabasic rocks was anhydrous, consisting of garnet + clinopyroxene + quartz + rutile ± plagioclase. Preserved clinopyroxene with plagioclase lamellae testifies that fluid activity was low during decompression. Therefore, fluid infiltration may be assumed to have happened during retrogression after decompression at upper amphibolite-facies conditions, which is supported by hornblende–plagioclase thermometry that yields ~750°C for these rocks (Board *et al.*, 2005). Hence, the average *P–T* conditions of Board *et al.* (2005) for dry conditions (~900°C; 1·2 GPa) are preferred and agree with the initial decompression stage on the *P–T* path presented here (Fig. 17).

Trace elements and rutile and zircon thermometry

Rutile trace element patterns in sample Z7-14-5 are very uniform among the large grains that occur in the rock matrix. These include Cr, Nb, Fe and Zr (all ~1000 μg g^{-1};

Table 3; Fig. 7, and Supplementary Data), as well as Al (~200 μg g^{-1}). Silicon and Ca contents are below the detection limits in almost all analysed matrix grains. Zr-in-rutile thermometry of the matrix rutile results in a very narrow range of temperatures for the vast majority of analysed grains of ~740°C (Table 3). Contents of Nb and Cr in matrix rutile are higher than the respective concentrations in rutile grains included in garnet (Table 3; Fig. 7). These temperatures and trace element concentrations are best interpreted to reflect a loss of Zr, Fe, Ca and Si from and gain of Cr and Nb by rutile during cooling from peak temperatures (~930°C) to amphibolite-facies temperatures of ~740°C. Zirconium is probably released to the grain matrix and added to existing zircon grains. This process is also evident from the retrograde growth zones of the zircon grains; these formed at temperatures between 873 and 744°C (calculated for $P = 1$ GPa) and yield ages postdating the peak-T event (Fig. 17). Ewing *et al.* (2013) showed that rutile from UHT metamorphic rocks in the Ivrea Zone (Italian Alps) that initially equilibrated at temperatures in excess of 1000°C adjusted to lower temperatures of ~750°C on the retrograde path by exsolution of zircon and baddelyite lamellae. Similar lamellae have been observed in UHT granulites from the Napier complex (Enderby Land, East Antarctica; Degeling, 2002). No exsolution lamellae of zircon or baddelyite were observed in rutile in the H.U. Sverdrupfjella samples, possibly owing to the lower peak metamorphic temperatures of these samples compared with the two other localities.

The increased Nb contents in the H.U. Sverdrupfella rutile probably reflect the retrograde formation of ilmenite and biotite. Niobium compatibility in ilmenite and biotite is lower than in rutile. This leads to a preferential enrichment of Nb in rutile in rocks in which rutile coexists with ilmenite or biotite (Luvizotto & Zack, 2009). At peak-P–T conditions, rutile was the only stable Ti-bearing mineral in Z7-14-5, and peak metamorphic rutile is expected to have the lowest Nb content, which is determined by the whole-rock Nb/Ti ratio. This is consistent with the lower Nb contents found in the garnet inclusions compared with the matrix rutile (Fig. 7).

Chromium is a trace element that is relatively compatible in rutile (e.g. Zack *et al.*, 2002), and it can also be incorporated in high concentrations in kyanite, but less so in sillimanite (e.g. Seifert & Langner, 1970). It is predicted from the pseudosection and supported by petrographic observation that the peak assemblage of Z7-14-5 contained coexisting kyanite and rutile. The kyanite was replaced by fibrous sillimanite during decompression, and the increased Cr contents in the matrix rutile (Fig. 7) probably represent this replacement of Cr-bearing kyanite by low-Cr sillimanite. High concentrations of Si and Ca and elevated Al in high- and ultra-high-temperature metamorphic rutile included in garnet possibly record a higher solubility of these elements in rutile at these conditions.

It is evident from the comparison of rutile inclusions with matrix grains that armouring by garnet inhibits or at least effectively decreases the efficiency of post-inclusion modification of trace elements such as Zr, Nb and Cr. The fact that selected rutile grains, and especially inclusions in garnet, record higher peak temperatures than zircon in any particular sample seems to be a recurring pattern in high-T metamorphic rocks (e.g. Baldwin *et al.*, 2007; Baldwin & Brown, 2008; Harley, 2008; Kotkovà & Harley, 2010). Rutile incorporates several thousands of μg g^{-1} Zr under UHT conditions and thus is expected to induce a noticeable dissolution of zircon at the thermal maximum rather than zircon growth (Kelsey & Powell, 2011; Kohn *et al.*, 2015). Mass-balance calculations using the whole-rock composition of sample Z7-14-5, and its modal abundances of rutile and zircon (iteratively calculated from Zr and Ti abundances), predict some net dissolution (4·1%) of zircon for a temperature increase from Stage M_{2a} (786°C, 0·95 GPa) to peak Stage M_{2c} (929°C, 1·45 GPa). In contrast, the fraction of rutile that needs to dissolve to saturate zircon in Ti over the same temperature interval is four orders of magnitude smaller (~0·0008%).

More importantly, though, than the respective solubilities, large differences in trace element diffusion are expected to cause potential discrepancies in the UHT metamorphic record of rutile and zircon, respectively. The diffusion coefficient of Ti in zircon is at least 10 orders of magnitude lower than for Zr in rutile at 900°C (Cherniak & Watson, 2007) and the concentrations of Ti in zircon are two orders of magnitude lower than the concentrations of Zr in rutile (Tomkins *et al.*, 2007). Hence, it is predicted that the entire rutile grains can diffusively adjust to higher temperatures and take up Zr into a bulk grain by volume diffusion, even if their rims slightly dissolve so as to saturate zircon (and possibly other minerals) in Ti. The homogeneity of the matrix rutile grains supports the experimentally predicted fast intra-grain diffusion of transition metals in rutile (Cherniak *et al.*, 2007; van Orman & Crispin, 2010; Marschall *et al.*, 2013*a*).

Zircon, in contrast, can only record those parts of the metamorphic history that led to zircon growth or recrystallization. Intra-grain diffusion of Ti (and most other elements) into zircon growth zones produced during earlier growth phases is inhibited and those zones cannot equilibrate diffusively to changing P–T conditions. This prediction is again supported by observation in the form of preserved intra-grain zoning of Ti in zircon (Fig. 10). However, the highest Ti-in-zircon temperatures recorded in zircon from felsic granulite sample Z7-14-5 are ~900–920°C (estimated for peak pressure conditions; Table 4), which is within error of the peak temperature estimated from Zr-in-rutile thermometry in this rock. There is a discrepancy between zircon growth zones that record peak temperature conditions and the predicted resorption of zircon in this rock at UHT conditions from the mass-balance calculation discussed above. This discrepancy is best resolved by invoking Ostwald ripening during which small grains are preferentially dissolved, whereas large grains grow even

larger. The common presence of very large zircon grains (500–1000 μm long) in granulites in general, and in felsic granulite Z7-14-5 in particular, supports the hypothesis that Ostwald ripening is an important growth process for single zircon grains under UHT conditions. This does not conflict with the slight decrease of the modal amount of zircon in the rock during heating. Our results show that zircon provides a powerful and robust tool to link age to temperature information for the prograde, peak, and retrograde sections of the *P–T* path (Fig. 17).

Ostwald ripening probably also led to the growth of garnet rims at peak temperatures and during initial decompression at high temperatures. The mode of garnet predicted from the pseudosection is approximately constant between Stage M2b, Stage M2c and during much of the decompression path into the stability field of sillimanite (Fig. 9a). However, rutile inclusions recording peak temperatures in the rim area of garnet (Fig. 8b) and one sillimanite inclusion very close to the preserved edge of one garnet grain (Supplementary Data Fig. S2y) demonstrate that single grains of garnet must have continued to grow under UHT conditions, even when the garnet mode in the rock stayed constant.

Geochronology

The oldest age in this set of samples is preserved by zircon in sample Z7-15-5 (Rootshorga gneiss) where a single grain analysis revealed an age of 1083 ± 12 Ma. Very similar zircon ages are known from other parts of the H.U. Sverdrupfella (1030–1050 Ma; Board *et al.*, 2005), from Gjelsvikfjella (*c.* 1070 Ma; Bisnath *et al.*, 2006), Kirwanveggen (1081 ± 4 Ma; Jackson, 1999), from the Ritscherflya sediments (1086 ± 4 Ma; Marschall *et al.*, 2013*b*), from Central Dronning Maud Land (*c.* 1080 Ma; Jacobs *et al.*, 1998), and from Sør Rondane (958–1115 Ma; Grantham *et al.*, 2013), and are interpreted as metamorphic ages related to the assembly of Rodinia. Geochronological data from metamorphic zircon from Grantham *et al.* (1995) and Groenewald *et al.* (1995) support the interpretation of a high-grade metamorphic event (M_1) at *c.* 1080 Ma in the H.U. Sverdrupfjella.

The oscillatory zoned, euhedral core domain of a zircon grain from sample Z7-15-2 (amphibolized mafic garnet granulite) has an age of 974 ± 4 Ma with a high Th/U ratio of >1·0; this age is, therefore, interpreted as the emplacement age of the mafic magmatic protolith probably as a result of post-collisional (with respect to the Grenville-age event) magmatic activity. Alternatively, this domain may be a xenocryst assimilated by the protolith mafic magma from the Rootshorga paragneiss country rock represented by sample Z7-15-5. In the latter case, 974 ± 4 Ma would be considered the maximum age of intrusion of the mafic magma. Hence, intrusion of the mafic magma occurred after Mesoproterozoic metamorphism, either in the early Neoproterozoic (at *c.* 974 Ma) or later, but prior to Pan-African collision recorded at *c.* 576 Ma in this sample.

The onset of Neoproterozoic metamorphism is marked by monazite growth in sample Z7-14-5 and zircon growth or recrystallization in sample Z7-15-5. Monazite inclusions in garnet yielding ages >600 Ma predate high-grade metamorphism accompanying major garnet growth as indicated by textural evidence and elevated Y and U contents. The oldest recorded monazite age is 644 ± 9 Ma (Fig. 14). However, as discussed above, these older monazite inclusions may as well represent partially reset Grenville-age monazite grains. The 608 ± 13 Ma zircon age from paragneiss sample Z7-15-5 may support the pre-600 Ma onset of metamorphism, yet the uncertainty on this analysis also prevents a clear distinction between concordance and discordance of this zircon age group (see Fig. 13d). Thus, the best estimate for the onset of Neoproterozoic metamorphism in the H.U. Sverdrupfjella is at 593 ± 8 Ma, but may possibly be as early as 640 Ma.

Felsic granulite sample Z7-14-5 has a group of zircon core domains with an age of 593 ± 8 Ma (Fig. 13a). Titanium thermometry in these age domains yields crystallization temperatures of 808–838°C (Fig. 18; or 5°C lower for a pressure of 0·95 GPa). Hence, zircon pins the timing of the attaining of temperatures of more than 800°C to *c.* 593 Ma.

The most pervasive zircon growth event that affected all investigated samples was between *c.* 575 and 560 Ma. The 570 ± 7 Ma age from felsic granulite sample Z7-14-5 is similar to those recorded in the amphibolized mafic garnet granulite (sample Z7-15-2), the Brattskarvet granite sample Z7-16-4, and the paragneiss Z7-15-5 (576 ± 9 Ma, 562 ± 3 Ma and 575 ± 7 Ma, respectively) and younger than most of the ages of monazite inclusions in garnet (see Fig. 14). Monazite included in garnet indicates significant garnet growth post-dating 581 Ma. Granitic inclusions (quartz + K-feldspar + plagioclase + biotite ± rutile ± zircon) in a *c.* 539 Ma domain of monazite in sample Z7-14-5 can be used to constrain a minimum age of the high-grade metamorphism. Therefore, the timing of high-grade metamorphism may be bracketed between 593 and 539 Ma.

Titanium contents in *c.* 570 Ma zircon domains in sample Z7-14-5 indicate crystallization temperatures of up to 876°C for $P = 1$ GPa, yet the *c.* 570 Ma dates are considered to be linked to prograde and peak temperatures at peak pressures. A pressure adjustment to the peak conditions of 1·45 GPa elevates the highest recorded Ti-in-zircon temperature to 921°C, which is indistinguishable from the peak temperature recorded in rutile. Zircon rims that constitute the 556 ± 7 Ma age group show similar Ti contents that translate to temperatures of up to 873°C at $P = 1$ GPa (Table 4; Fig. 18). Pressure adjustment of this rutile group is less straightforward, but our preferred interpretation is that these rim domains grew during cooling and, therefore, during or after decompression. The measured Ti contents translate to temperatures of 813–838°C for a pressure of 0·65 GPa (Table 4).

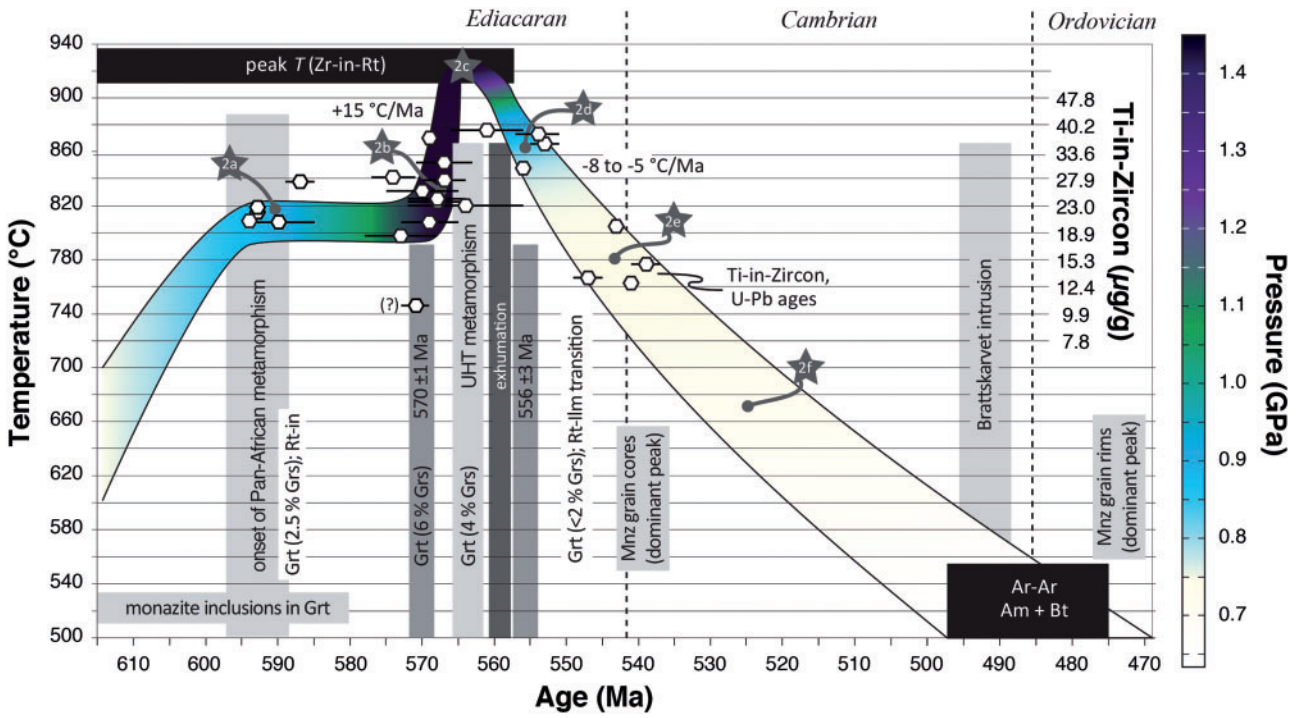

Fig. 18. Summary of temperature–time evolution of the investigated samples. The *T–t* path is colour-contoured for pressure as given by the scale on the right-hand side. Hexagons mark combined zircon U–Pb age and Ti thermometry (for $P = 1$ GPa) with the concentration scale given on the right-hand side. The onset of metamorphism is marked by zircon at 593 Ma, but may be as early as 640 Ma, indicated by monazite inclusions in garnet. The earliest generation of garnet (low Ca) with rutile inclusions and the growth of zircon cores at *c.* 590 Ma is interpreted as metamorphic Stage M_{2a}. A short period of rapid heating following near-isothermal loading led to a short-lived period of ultrahigh temperatures with peak conditions of 929 ± 29°C at 1·45 GPa at *c.* 570 Ma. This stage was immediately followed by near-isothermal decompression to *c.* 0·75 GPa and was followed by a ≥50 Myr period of cooling. The Brattskarvet intrusive suite was emplaced in the late Cambrian.

The majority of monazite grains in the matrix of sample Z7-14-5 are younger than 570 Ma with the dominant age peak at *c.* 539 Ma and a continuum in ages correlated with a continuous change in chemical compositions to≤450 Ma. This is interpreted as recrystallization of monazite after decompression under high-temperature–low-pressure conditions, and during isobaric cooling from granulite- or upper-amphibolite-facies conditions probably into the greenschist facies. Garnet was probably the major reservoir of Y in this rock after 581 Ma until it began to break down to cordierite, biotite and other minerals before 474 Ma. Monazite domains that grew or recrystallized between 570 and 480 Ma do not show elevated Y contents, although decompression and initial garnet breakdown most probably occurred shortly after 560 Ma. This is interpreted to reflect the consumption of only small portions of garnet in this rock combined with efficient back-diffusion of Y into the remaining garnet. High-Y monazite formed at *c.* 474 Ma, probably during fluid influx. This fluid replaced garnet by micas at temperatures that were probably too low for back-diffusion of Y into remaining garnet. The youngest monazite domains form irregular veins cutting through the grains and patches that probably represent solution–reprecipitation fronts related to fluid activity postdating the intrusion of the Brattskarvet granite.

Ages of *c.* 570 Ma have been reported from Central Dronning Maud Land (575–560 Ma; Mikhalsky *et al.*, 1997; Jacobs *et al.*, 1998), Gjelsvikfjella (*c.* 570 Ma; Bisnath *et al.*, 2004) as well as from Kirwanveggen (585 ± 20 Ma; Harris *et al.*, 1995), where they were also interpreted to date pervasive deformation, migmatization and high-grade metamorphism. Board *et al.* (2005) reported a pooled zircon U–Pb age of 565 ± 11 Ma for a sample from the Rootshorga Paragneiss. This pooled age consists of single grain analyses that were interpreted as originating from a single growth event. The ages of single grains range from 594 ± 15 to 555 ± 20 Ma. These ages cover the same age range as our high-*T* zircon ages and can be assigned to the age groups defined in this study.

Zircon grains from the Rootshorga paragneiss, in addition to those from the felsic granulite and the amphibolized mafic garnet granulite all show ages in the 550–540 Ma range (550 ± 8 Ma, 542 ± 7 Ma and 542 ± 8 Ma in samples Z7-15-2, Z7-14-5 and Z7-15-5, respectively). Ti-in-zircon thermometry linked to U–Pb ages in 542 Ma growth domains of the felsic granulite indicates temperatures of 728–770°C (for $P = 0{\cdot}65$ GPa; Table 4). Upper amphibolite-facies conditions are, therefore, well documented for 542 ± 7 Ma, and this is also indistinguishable from the dominant age observed in the monazite in sample Z7-14-5 (539 Ma). Monazite

and zircon ages (540 ± 6 Ma) from Board *et al.* (2005) support this timing for the retrograde amphibolite-facies conditions.

A brief heating event at *c.* 570 Ma that led to the peak metamorphic temperatures results from zircon temperature and age information (Fig. 18). UHT conditions are bracketed by the zircon U–Pb ages to a maximum duration of 14 ± 10 Myr, which corresponds to the timescale for the duration of the UHT metamorphic event in the Anápolis–Itauçu Complex in Brazil (Baldwin & Brown, 2008). Further restrictions to the maximum duration of UHT conditions in our samples come from diffusion modelling of the preserved prograde Ca zonation in garnet. Depending on the choice of diffusion coefficients, peak temperatures can have persisted only for a maximum of 6·2, 1, or less than 0·5 Myr. The age of the high-pressure stage, corresponding to ~53 km depth, in combination with the age of the retrograde M_{2d} stage at pressures of 0·75 GPa (~27 km depth), requires an exhumation rate of at least 0·18 ± 0·14 cm a^{-1}. Cooling rates estimated from the resulting *P–T* path are in the range of –8°C Ma^{-1} to –5°C Ma^{-1} for a duration of 80 Myr (Fig. 18).

Samples Z7-16-4 and Z7-15-5 show zircon crystallization events at 518 ± 9 Ma and 521 ± 7 Ma, respectively. No direct link to the *P–T* path can be established, but U/Pb concordia ages of 528 ± 6 Ma were also found by Board *et al.* (2005) for monazite in H.U. Sverdrupfjella. Furthermore, Jacobs *et al.* (2003b) described an undeformed mafic dyke with a zircon crystallization age of 523 ± 5 Ma in Gjelsvikfella that is considered to postdate major tectonic activity (Jacobs *et al.*, 2003*b*).

Our geochronological data provide a well-constrained crystallization age of 491 ± 6 Ma for the Brattskarvet intrusion. Board *et al.* (2005) reported ^{40}Ar–^{39}Ar hornblende and biotite cooling ages of different samples across H.U. Sverdrupfjella (486 ± 5 Ma) as well as an upper intercept zircon age of 480 ± 10 Ma interpreted as the intrusion age for a post-tectonic granitic dyke, supporting magmatic activity accompanying thermal input in the latest Cambrian and early Ordovician. The zircon crystallization age for the Brattskarvet intrusion obtained in this study is consistent with the intrusion age reported by Bisnath & Frimmel (2005) of *c.* 489 Ma, and it is slightly younger than the whole-rock Rb/Sr age (518 ± 15 Ma, MSWD = 1·5) and the low-precision Sm/Nd age (522 ± 120 Ma, MSWD = 5·4) of Moyes *et al.* (1993*b*).

The intrusion age of the Stabben suite, located in Gjelsvikfjella (65 km east of Brattskarvet), is constrained to 490–500 Ma (Paulsson & Austrheim, 2003; Bisnath *et al.*, 2006). In addition, a granite sheet from Gygra, located ~15 km eastwards of the Stabben intrusive body, was dated at 487 ± 4 Ma using zircon (Jacobs *et al.*, 2003*b*). Monazite and to a minor extent zircon in sample Z7-14-5 were also affected by the Brattskarvet intrusion, which included the block from which sample Z7-14-5 was taken. These recrystallization zones yield ages of *c.* 474 Ma in monazite and 494 ± 7 Ma, in zircon, which are similar to or slightly younger than the advocated intrusion age of the pluton. Magmatism in the H.U. Sverdrupfjella lasted to at least 470 Ma as documented by the Dalmatian two-mica granite (*c.* 470 Ma; Grantham *et al.*, 1991) 30–40 km SE of the location of the samples investigated here. Zircon recrystallization and solution–reprecipitation of monazite as observed in sample Z7-14-5 may be attributed to hydrothermal activity related to that magmatism.

A period of extensive late Cambrian magmatism around 500–490 Ma is evident throughout the entire Central DML in the form of A2-type charnockite and syenite intrusions covering ~15 000 km^2 (Jacobs *et al.*, 2008*a*). The Brattskarvet intrusive complex probably represents the westernmost intrusion of this magmatic activity (Jacobs *et al.*, 2008*a*), and our new datum shows that it also shares an intrusion age with the syenites in Central DML. Monazite and zircon dating in this study also show the effects of weak thermal pulses or fluid activity that caused solution–reprecipitation events into the Silurian and Devonian as late as 380 Ma.

Geodynamic and palaeogeographical implications

Timing of eclogite–high-pressure granulite (E–HPG)-facies metamorphism at *c.* 570 Ma in H.U. Sverdrupfjella determined in this study correlates well with the *P–T–t* evolution of the rest of DML (Fig. 19). DML is characterized by rocks metamorphosed at high to ultrahigh temperatures at initially high pressures, discriminating the majority of them as E–HP granulites (Shiraishi & Kojima, 1987; Harris, 1999; Bisnath & Frimmel, 2005; Baba *et al.*, 2008; Yoshimura *et al.*, 2008; Elvevold & Engvik, 2013). Most age estimates for peak metamorphism within DML are in the range of 580–560 Ma (Harris *et al.*, 1995; Jacobs *et al.*, 2003*a*; Bisnath *et al.*, 2004, 2006; Board *et al.*, 2005; Shiraishi *et al.*, 2008; Tsunogae *et al.*, 2014), which is coeval with high-grade metamorphism determined for the H.U. Sverdrupfjella in this study and the inferred time of the peak of collision. Although temperature estimates for the Schirmacher Hills, the northeastern part of Sør Rondane and perhaps the northern Humboldt Mountains are consistent with those for the rest of DML, considerably lower peak pressures and an earlier time for the peak of metamorphism of *c.* 630 Ma have been inferred (Asami *et al.*, 1992; Ravikant & Kundu, 1998; Baba *et al.*, 2006, 2008, 2013; Ravikant *et al.*, 2007; Shiraishi *et al.*, 2008; Pant *et al.*, 2013). Geochronological data indicate, however, a second Neoproterozoic overprint of the Schirmacher Hills, the Sør Rondane and the Humboldt Mountains at *c.* 580 Ma (Ravikant *et al.*, 2007; Grantham *et al.*, 2013; Pant *et al.*, 2013). Granulites from the latter regions may represent continental arc granulites formed at *c.* 630 Ma, predating the subsequent E–HPG metamorphism.

Eclogite–HPG metamorphism is taken as an indication of continent–continent collision (see Brown, 2007),

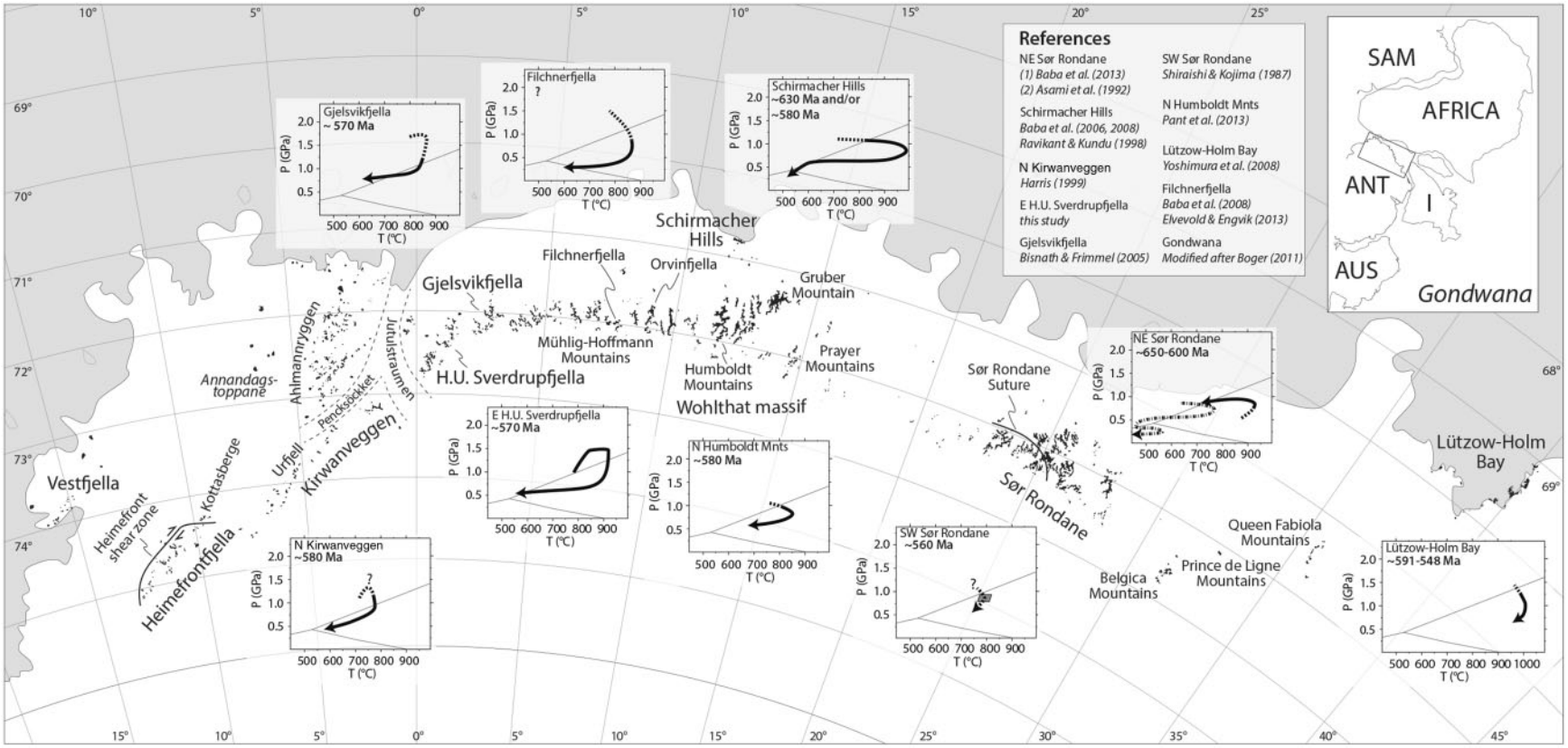

Fig. 19. Map of Dronning Maud Land showing the coastline along the Atlantic sector of Antarctica. Rock outcrop is marked in black. Ultrahigh-temperature granulite-facies and eclogite–high-pressure granulite-facies rocks with metamorphic ages between 650 and 550 Ma were observed in a number of localities throughout DML, as indicated by the inset *P–T* diagrams compiled from the literature (Eastern H.U. Sverdrupfjella: this study). All *P–T* diagrams are drawn at the same scale. The inset shows the position of DML within the reconstructed Gondwana supercontinent (SAM, South America; ANT, Antarctica; AUS, Australia; I, India).

which is recorded in DML at *c.* 580–560 Ma. In particular, the near-isothermal loading from normal crustal thickness (~35 km) to significantly greater depth (~53 km) recorded in felsic granulite sample Z7-14-5 in our study probably resulted from rapid crustal thickening during collision. A proximal position of the H.U. Sverdrupfjella with respect to the collision suture is thus indicated. The samples studied here record a clockwise *P–T* path during which loading (crustal thickening or stacking) was followed by isobaric heating. This *P–T* evolution is consistent with thermal models of thickening of continental crust in collision zones (e.g. England & Thompson, 1986; Thompson & Connolly, 1995).

Significant heating of the crust leads to mechanical weakening and eventually to orogenic collapse, which in turn leads to rapid, near-isothermal exhumation of deeply buried crust (e.g. Vanderhaeghe & Teyssier, 2001; Brown, 2007). The very short-lived UHT peak metamorphic phase (<6 Myr) followed by near-isothermal decompression recorded in the H.U. Sverdrupfjella is consistent with collapse of the hot, weak core of the orogen following collision. The extremely short-lived UHT event shows, in fact, how quickly the orogen may be destabilized by heating. Our observations are also consistent with the geodynamic model of Jacobs & Thomas (2004), who argued that escape tectonics led to the rapid collapse of the East African–Antarctic orogen shortly after continental collision.

Terranes adjacent to DML, such as Madagascar, Sri Lanka and South India, show a very similar evolution to the one observed in DML (Milisenda *et al.*, 1988; Baur *et al.*, 1991; Hiroi *et al*, 1994; Hölzl *et al.*, 1994; Markl *et al.*, 2000; Nandakumar & Harley, 2000; Cenki *et al.*, 2002; Braun & Bröcker, 2004; Collins, 2006). All of these regions are characterized by (U)HT–HP metamorphism at 580–560 Ma. Mozambique, and Kenya and Somalia farther to the north, also show evidence for a metamorphic overprint at that time (Key *et al.*, 1989; Sassi *et al.*, 1993; Lenoir *et al.*, 1994; Meert & Van Der Voo, 1996; Kröner *et al.*, 1997, 2001; Meert, 2003). A genetic relationship between these regions has previously been established and is referred to as the Mozambique Belt (e.g. Collins *et al.*, 2007). This belt very probably extended southwards into DML, as is evident from our data and from studies on the surrounding areas (Grantham *et al.*, 2013). The amalgamation of greater India to central Africa is thought to be responsible for the formation of this orogen (e.g. Möller *et al.*, 2000; Boger & Miller, 2004), whereas it was postulated that an independent collision between the Coats Land Block and the Kalahari Craton may have been responsible for high-grade metamorphism in DML at *c.* 560 Ma (Kleinschmidt & Boger, 2009; Boger, 2011). The contemporaneity of the orogenic events along the Mozambique Belt including DML, as discussed above, requires that the Coats Land Block was part of greater India. This interpretation is consistent with the evolution model for the Coats Land Block proposed by Kleinschmidt & Boger (2009).

CONCLUSIONS

Detailed petrological and geochronological investigations of two granulite samples and a small number of supplementary samples from the H.U. Sverdrupfjella carried out in this study result in a well-defined *P–T–t* path for at least part of the Rootshorga Formation, and clearly reveal the dimensions and significance of metamorphism in the H.U. Sverdrupfjella at the time of the Pan-African orogeny. The following conclusions are drawn from this study.

1. Evidence for prograde, peak, and retrograde metamorphism is preserved in the samples. The *P–T* evolution determined in this study indicates that the investigated rocks from the H.U. Sverdrupfjella underwent loading from ~30 km to 50 km depth at *c.* 800°C, reflecting eclogite–high-pressure granulite (E–HPG)-facies metamorphic conditions, followed by heating to peak conditions of 929 ± 23°C and 1·45 GPa. The E-HPG stage was followed by near-isothermal decompression to a crustal depth of 25–30 km with subsequent near-isobaric cooling.
2. Combined Ti-in-zircon thermometry and U/Pb age data for zircon and complementary Zr-in-rutile thermometry were used to unravel the *T–t* history of this unit of the H.U. Sverdrupfjella. Zircon indicates that temperatures above 800°C were already attained by *c.* 590 Ma, some 25 Myr prior to the attainment of peak metamorphic conditions, and that such high temperatures persisted for at least 40 Myr. At *c.* 570 Ma a very short-lived heating period affected the samples. The timing for the E–HPG metamorphism at near-peak conditions is constrained by combined Ti-in-zircon thermometry and U–Pb dating of zircon to shortly after 570 ± 7 Ma. Further, it is evident from zircon data and from preserved prograde Ca zonation in garnet that ultrahigh temperatures in excess of 900°C lasted for a maximum of 6 Myr. Subsequent to peak pressure–temperature conditions, the sampled rocks were exhumed to crustal depths of 25–30 km. Average cooling rates are 5–8°C Ma^{-1} for a duration of *c.* 80 Myr throughout the late Ediacaran, the Cambrian and possibly the early Ordovician.
3. E–HP granulites produced and exhumed through a clockwise *P–T* path are characteristic of continent–continent collisions. This, together with near-isothermal loading from pressures reflecting a normal crustal thickness to ~50 km depth followed by isobaric heating are strong evidence for the proximity of these samples to a collision suture. That evidence supports amalgamation of a continent or terrane to DML at *c.* 570 Ma. The correlation of contemporaneous HP–(U)HT metamorphosed terranes in DML and adjacent terranes (i.e. Madagascar, South India, Sri Lanka), as well as indications for a metamorphic overprint in Mozambique, Kenya and Somalia, suggests a continuation of the *c.* 570 Ma Mozambique Belt farther to the south including DML. The striking

similarities in age estimates for peak metamorphic conditions in all of these terranes imply that greater India, including the Coats Land Block as its southern continuation, collided with West Gondwana at *c.* 570 Ma, resulting in a continuous orogenic belt stretching from Somalia to Dronning Maud Land.

4. The high-grade Ediacaran–Cambrian metamorphic overprint in DML was characterized by penetrative deformation and granulite-facies recrystallization. It is, therefore, difficult to reliably assign any *P–T* estimates to the pre-Pan-African metamorphic history of the rocks, such as the Mesoproterozoic event related to the assembly of Rodinia that is evident from the zircon ages determined in this study, as well as published zircon ages for DML.
5. It is demonstrated that Zr and other trace elements in rutile inclusions in garnet can deliver information on the *P–T* history of a rock, in particular for rocks that preserve prograde garnet zones. The chemical composition of the garnet host in combination with a pseudosection was used as a geobarometer and combined with the Zr-in-rutile thermometer applied to the inclusions to derive several stages along the prograde and peak metamorphic *P–T* path. Matrix rutile, in contrast, records late-stage equilibration of trace elements and Zr during cooling to temperatures of ~750°C. The increase of Nb and Cr abundances in matrix rutile in comparison with the rutile inclusions in garnet is interpreted to reflect the replacement of rutile by ilmenite and biotite, and of kyanite by sillimanite, respectively.

ACKNOWLEDGEMENTS

We thank Rainer Altherr, Klaus Mezger, Chris Hawkesworth and Phil Leat for discussion and guidance at various stages of this project. Technical guidance with the Raman spectrometer by Frieder Klein is acknowledged. Very detailed and constructive reviews by Simon Harley, Dave Kelsey and Geoff Grantham are acknowledged, as well as review comments and editorial handling by Joerg Hermann. Simon Harley is also acknowledged for providing a correction to the Aranovich & Berman (1997) thermometer. The British Antarctic Survey (BAS) is acknowledged for preparation for and organization of the field season and the logistics during the trip, with special thanks to field assistants Sune Tamm and Teddy Wolrath. Also, the Norwegian Polar Institute and the team of Troll station are thanked for actively supporting our field party.

FUNDING

This study was financially supported by the NSF polar program (AES grant 1142156 to H.R.M.). Ion microprobe analyses at the Northeast National Ion Microprobe Facility at Woods Hole Oceanographic Institution were partially subsidised by the Instrumentation and Facilities Program, Division of Earth Sciences, National Science Foundation (Grants 1035310 and 1258876).

SUPPLEMENTARY DATA

Supplementary data for this paper are available at *Journal of Petrology* online.

REFERENCES

Aranovich, L. Y. & Berman, R. G. (1997). A new garnet–orthopyroxene thermometer based on reversed Al_2O_3 solubility in $FeO–Al_2O_3–SiO_2$ orthopyroxene. *American Mineralogist* **82**, 345–353.

Armstrong, J. T. (1995). CITZAF—A package of correction programs for the quantitative electron microbeam X-ray analysis of thick polished materials, thin-films, and particles. *Microbeam Analysis* **4**, 177–200.

Arndt, N. T., Todt, W., Chauvel, C., Tapfer, M. & Weber, K. (1991). U–Pb zircon age and Nd isotopic composition of granitoids, charnockites and supracrustal rocks from Heimefrontfjella, Antarctica. *International Journal of Earth Sciences* **80**, 759–777.

Asami, M., Osanai, Y., Shiraishi, K. & Makimotot, H. (1992). Metamorphic evolution of the Sør Rondane Mountains, East Antarctica. In: Yoshida, Y., Kaminuma, K. & Shiraishi, K. (eds) *Recent Progress in Antarctic Earth Science*. Terra, pp. 7–15.

Baba, S., Owada, M., Grew, E. S. & Shiraishi, K. (2006). Sapphirine granulite from Schirmacher Hills, Central Dronning Maud Land. In: Fütterer, D. K., Damakse, D., Kleinschmidt, G., Miller, H. & Tessensohn, F. (eds) *Antarctica: Contributions to Global Earth Sciences*. Springer, pp. 37–44.

Baba, S., Owada, M. & Shiraishi, K. (2008). Contrasting metamorphic *P–T* path between Schirmacher Hills and Mühlig-Hofmannfjella, central Dronning Maud Land, East Antarctica. In: Satish-Kumar, M., Motoyoshi, Y., Osanai, Y., Hiroi, Y. & Shiraishi, K. (eds) *Geodynamic Evolution of East Antarctica: A Key to the East–West Gondwana Connection. Geological Society, London, Special Publications* **308**, 401–417.

Baba, S., Osanai, Y., Nakano, N., Owada, M., Hokada, T., Horie, K., Adachi, T. & Toyoshima, T. (2013). Counterclockwise *P–T* path and isobaric cooling of metapelites from Brattnipene, Sør Rondane Mountains, East Antarctica: Implications for a tectonothermal event at the proto-Gondwana margin. *Precambrian Research* **234**, 210–228.

Baldwin, J. A. & Brown, M. (2008). Age and duration of ultrahigh-temperature metamorphism in the Anápolis–Itaçuu Complex, Southern Brasília Belt, central Brazil—constraints from U–Pb geochronology, mineral rare earth element chemistry and trace-element thermometry. *Journal of Metamorphic Geology* **26**, 213–233.

Baldwin, J. A., Brown, M. & Schmitz, M. D. (2007). First application of titanium-in-zircon thermometry to ultrahigh-temperature metamorphism. *Geology* **35**, 295–298.

Baur, N., Kröner, A., Liew, T. C., Todt, W., Williams, I. S. & Hofmann, A. W. (1991). U–Pb isotopic systematics of zircons from prograde and retrograde transition zones in high-grade orthogneisses, Sri Lanka. *Journal of Geology* **99**, 527–545.

Bisnath, A. & Frimmel, H. E. (2005). Metamorphic evolution of the Maud Belt *P–T–t* path for high-grade gneisses in Gjelsvikfjella, Dronning Maud Land, East Antarctica. *Journal of African Earth Sciences* **43**, 505–524.

Bisnath, A., Frimmel, H. E. & Armstrong, R. A. (2004). Age and tectonothermal evolution of Gjelsvikfjella, Maud Belt, East

Antarctica. In: Ashwal, L. D. (ed.) *Abstract Volume, University of Witwatersrand, Johannesburg, South Africa*, pp. 60–61.

Bisnath, A., Frimmel, H. E., Armstrong, R. A. & Board, W. S. (2006). Tectonothermal evolution of the Maud Belt: New SHRIMP U–Pb zircon data from Gjelsvikfjella, Dronning Maud Land, East Antarctica. *Precambrian Research* **150**, 95–121.

Black, L. P., Kamo, S. L., Allen, C. M., et al. (2004). Improved $^{206}Pb/^{238}U$ microprobe geochronology by the monitoring of a trace-element-related matrix effect; SHRIMP, ID-TIMS, ELA-ICP-MS and oxygen isotope documentation for a series of zircon standards. *Chemical Geology* **205**, 115–140.

Board, W. S., Frimmel, H. E. & Armstrong, R. A. (2005). Pan-African tectonism in the western Maud Belt: *P–T–t* path for high-grade gneisses in the H.U. Sverdrupfjella, East Antarctica. *Journal of Petrology* **46**, 671–699.

Boger, S. D. (2011). Antarctica—before and after Gondwana. *Gondwana Research* **19**, 335–371.

Boger, S. D. & Miller, J. M. L. (2004). Terminal suturing of Gondwana and the onset of the Ross–Delamerian Orogeny: the cause and effect of an Early Cambrian reconfiguration of plate motions. *Earth and Planetary Science Letters* **219**, 35–48.

Bohlen, S. R. (1991). On the formation of granulites. *Journal of Metamorphic Geology* **9**, 223–229.

Bohlen, S. R. & Liotta, J. J. (1986). A barometer for garnet amphibolites and garnet granulites. *Journal of Petrology* **27**, 1025–1034.

Bohlen, S. R., Wall, V. J. & Boettcher, A. L. (1983). Experimental investigations and geological applications of equilibria in the system $FeO–TiO_2–Al_2O_3–SiO_2–H_2O$. *American Mineralogist* **68**, 1049–1058.

Braun, I. & Bröcker, M. (2004). Monazite dating of granitic gneisses and leucogranites from the Kerala Khondalite Belt, southern India: implications for Late Proterozoic crustal evolution in East Gondwana. *International Journal of Earth Sciences* **93**, 13–22.

Brown, M. (2007). Metamorphic conditions in orogenic belts: a record of secular change. *International Geology Review* **49**, 193–234.

Bucher, K. & Grapes, R. (2011). *Petrogenesis of Metamorphic Rocks*. Springer.

Carlson, W. D. (2006). Rates of Fe, Mg, Mn, and Ca diffusion in garnet. *American Mineralogist* **91**, 1–11.

Cenki, B., Kriegsman, L. M. & Braun, I. (2002). Melt-producing and melt-consuming reactions in the Achankovil cordierite gneisses, South India. *Journal of Metamorphic Geology* **20**, 543–561.

Chatterjee, N., Banerjee, M., Bhattacharya, A. & Maji, A. K. (2010). Monazite chronology, metamorphism–anatexis and tectonic relevance of the mid-Neoproterozoic Eastern Indian Tectonic Zone. *Precambrian Research* **179**, 99–120.

Cherniak, D. J. & Watson, E. B. (2007). Ti diffusion in zircon. *Chemical Geology* **242**, 470–483.

Cherniak, D. J., Manchester, J. & Watson, E. B. (2007). Zr and Hf diffusion in rutile. *Earth and Planetary Science Letters* **261**, 267–279.

Collins, A. S. (2006). Madagascar and the amalgamation of Central Gondwana. *Gondwana Research* **9**, 3–16.

Collins, A. S., Clark, C., Sajeev, K., Santosh, M., Kelsey, D. E. & Hand, M. (2007). Passage through India: the Mozambique Ocean suture, high-pressure granulites and the Palghat–Cauvery shear zone system. *Terra Nova* **19**, 141–147.

Connolly, J. A. D. (2005). Computation of phase equilibria by linear programming: A tool for geodynamic modeling and its application to subduction zone decarbonation. *Earth and Planetary Science Letters* **236**, 524–541.

Connolly, J. A. D. (2009). The geodynamic equation of state: what and how. *Geochemistry, Geophysics, Geosystems* **10**, Q10014.

Crank, J. (1975). *The Mathematics of Diffusion*, 2nd edn. Oxford University Press.

Degeling, H. S. (2002). Zircon equilibria in metamorphic rocks. PhD thesis, Australian National University, Canberra, ACT.

Dietz, R. S. & Sproll, W. P. (1970). Fit between Africa and Antarctica: a continental drift reconstruction. *Science* **167**, 1612–1614.

Eckert, J. O., Newton, R. C. & Kleppa, O. J. (1991). The ΔH of reaction and recalibration of garnet–pyroxene–plagioclase–quartz geobarometers in the CMAS system by solution calorimetry. *American Mineralogist* **76**, 148–160.

Elvevold, S. & Engvik, A. K. (2013). Pan-African decompressional *P–T* path recorded by granulites from central Dronning Maud Land, Antarctica. *Mineralogy and Petrology* **107**, 651–664.

England, P. C. & Thompson, A. (1986). Some thermal and tectonic models for crustal melting in continental collision zones. In: Coward, M. P. & Ries, A. C. (eds) *Collision Tectonics. Geological Society, London, Special Publications* **19**, 83–94.

Ewing, T. A., Hermann, J. & Rubatto, D. (2013). The robustness of the Zr-in-rutile and Ti-in-zircon thermometers during high-temperature metamorphism (Ivrea–Verbano Zone, northern Italy). *Contributions to Mineralogy and Petrology* **165**, 757–779.

Ferriss, E. D. A., Essene, E. J. & Becker, U. (2008). Computational study of the effect of pressure on the Ti-in-zircon geothermometers. *European Journal of Mineralogy* **20**, 745–755.

Fitzsimons, I. C. W. (2000). Grenville-age basement provinces in East Antarctica: Evidence for three separate collisional orogens. *Geology* **28**, 879–882.

Frimmel, H. E. (2004). Formation of a late Mesoproterozoic supercontinent: the South Africa–East Antarctica connection. In: Eriksson, P., Altermann, W., Nelson, D., Mueller, W., Catuneanu, O. & Catuneanu, O. (eds) *The Precambrian Earth: Tempos and Events. Developments in Precambrian Geology* **12**, 240–255.

Fuhrmann, M. L. & Lindsley, D. H. (1988). Ternary-feldspar modeling and thermometry. *American Mineralogist* **73**, 201–215.

Grantham, G. H. (1996). Aspects of Jurassic magmatism and faulting in western Dronning Maud Land, Antarctica: implications for Gondwana break-up. In: Storey, B. C., King, E. C. & Livermore, R. A. (eds) *Weddell Sea Tectonics and Gondwana Break-up. Geological Society, London, Special Publications* **108**, 63–71.

Grantham, G. H., Moyes, A. B. & Hunter, D. R. (1991). The age, petrogenesis and emplacement of the Dalmatian Granite, H.U. Sverdrupfjella, Dronning Maud Land, Antarctica. *Antarctica Science* **3**, 197–204.

Grantham, G. H., Jackson, C., Moyes, A. B., Groenewald, P. B., Harris, P. D., Ferrar, G. & Krynauw, J. R. (1995). The tectonothermal evolution of the Kirwanveggen–H.U. Sverdrupfjella areas, Dronning Maud Land, Antarctica. *Precambrian Research* **75**, 209–229.

Grantham, G. H., Manhica, A. D. S. T., Armstrong, R. A., Kruger, F. J. & Loubser, M. (2011). New SHRIMP, Rb/Sr and Sm/Nd isotope and whole rock chemical data from central Mozambique and western Dronning Maud Land, Antarctica: Implications for the nature of the eastern margin of the Kalahari Craton and the amalgamation of Gondwana. *Journal of African Earth Sciences* **59**, 74–100.

Grantham, G. H., Macey, P. H., Horie, K., Kawakami, T., Ishikawa, M., Satish-Kumar, M., Tsuchiya, N., Graser, P. & Azevedo, S. (2013). Comparison of the metamorphic history of the Monapo Complex, northern Mozambique and Balchenfjella and Austhameren areas, Sør Rondane, Antarctica: Implications for the Kuunga Orogeny and the amalgamation of N and S. Gondwana. *Precambrian Research* **234**, 85–135.

Groenewald, P. B. & Hunter, D. R. (1991). Granulites of the northern H.U. Sverdrupfjella, western Dronning Maud Land: metamorphic history from garnet–pyroxene assemblages, coronas and hydration reactions. In: Thomson, M. R. A., Crame, J. A. & Thomson, J. W. (eds) *Geological Evolution of Antarctica*. Cambridge University Press, pp. 61–66.

Groenewald, P. B., Grantham, G. H. & Watkeys, M. K. (1991). Geological evidence for a Proterozoic to Mesozoic link between southeastern Africa and Dronning Maud Land, Antarctica. *Journal of the Geological Society, London* **148**, 1115–1123.

Groenewald, P. B., Moyes, A. B., Grantham, G. H. & Krynauw, J. R. (1995). East Antarctic crustal evolution: geological constraints and modelling in western Dronning Maud Land. *Precambrian Research* **75**, 231–250.

Grosch, E. G., Bisnath, A., Frimmel, H. E. & Board, W. S. (2007). Geochemistry and tectonic setting of mafic rocks in western Dronning Maud Land, East Antarctica: implications for the geodynamic evolution of the Proterozoic Maud Belt. *Journal of the Geological Society, London* **164**, 465–475.

Grosch, E. G., Frimmel, H. E., Abu-Alam, T. & Košler, J. (2015). Metamorphic and age constraints on crustal reworking in the western H.U. Sverdrupfjella: implications for the evolution of western Dronning Maud Land, Antarctica. *Journal of the Geological Society, London* **172**, 499–518.

Harley, S. L. (1984). An experimental study of the partitioning of Fe and Mg between garnet and orthopyroxene. *Contributions to Mineralogy and Petrology* **86**, 359–373.

Harley, S. L. (1989). The origins of granulites: a metamorphic perspective. *Geological Magazine* **126**, 215–247.

Harley, S. L. (1998). On the occurrence and characterization of ultrahigh-temperature crustal metamorphism. In: Treloar, P. J. & O'Brien, P. J. (eds) *What Drives Metamorphism and Metamorphic Reaction? Geological Society, London, Special Publications* **138**, 81–107.

Harley, S. L. (2003). Archaean–Cambrian crustal development of East Antarctica: metamorphic characteristics and tectonic implications. In: Yoshida, M., Windley, B. E. & Dasgupta, S. (eds) *Proterozoic East Gondwana: Supercontinent Assembly and Breakup. Geological Society, London, Special Publications* **206**, 203–230.

Harley, S. L. (2008). Refining the *P–T* records of UHT crustal metamorphism. *Journal of Metamorphic Geology* **26**, 125–154.

Harley, S. L. & Kelly, N. M. (2007). The impact of zircon–garnet REE distribution data on the interpretation of zircon U–Pb ages in complex high-grade terrains: an example from the Rauer Islands, East Antarctica. *Chemical Geology* **241**, 62–87.

Harley, S. L., Fitzsimons, I. C. W. & Zhao, Y. (2013). Antarctica and supercontinent evolution: historical perspectives, recent advances and unresolved issues. In: Harley, S. L., Fitzsimons, I. C. W. & Zhao, Y. (eds) *Antarctica and Supercontinent Evolution. Geological Society, London, Special Publications* **383**, 1–34.

Harris, C. & Grantham, G. H. (1993). Geology and petrogenesis of the Straumsvola nepheline syenite complex, Dronning Maud Land, Antarctica. *Geological Magazine* **130**, 513–532.

Harris, P. D. (1999). *The geological evolution of Neumayerskarvet in the northern Kirwanveggen, Western Dronning Maud Land, Antarctica*. PhD thesis, University of Johannesburg.

Harris, P. D., Moyes, A. B., Fanning, C. M. & Armstrong, R. A. (1995). Zircon ion microprobe results from the Maudheim high-grade gneiss terrane, western Dronning Maud Land, Antarctica. In: Barton, J. M. & Copperthwaite, Y. E. (eds) *Centennial Geocongress, Extended Abstracts, Geological Society of South Africa*, pp. 240–242.

Hiess, J., Nutman, A. P., Bennett, V. C. & Holden, P. (2008). Ti-in-zircon thermometry applied to contrasting Archean metamorphic and igneous systems. *Chemical Geology* **247**, 323–338.

Hiroi, Y., Ogo, Y. & Namba, K. (1994). Evidence for prograde metamorphic evolution of Sri Lankan pelitic granulites, and implications for the development of continental crust. *Precambrian Research* **66**, 245–263.

Holland, T. J. B. & Blundy, J. (1994). Non-ideal interactions in calcic amphiboles and their bearing on amphibole–plagioclase thermometry. *Contributions to Mineralogy and Petrology* **116**, 433–447.

Holland, T. & Powell, R. (2001). Calculation of phase relations involving haplogranitic melts using an internally consistent thermodynamic dataset. *Journal of Petrology* **42**, 673–683.

Holland, T. & Powell, R. (2011). An improved and extended internally consistent thermodynamic dataset for phases of petrological interest, involving a new equation of state for solids. *Journal of Metamorphic Geology* **29**, 333–383.

Hölzl, S., Hofmann, A. W., Todt, W. & Köhler, H. (1994). U–Pb geochronology of the Sri Lanka basement. *Precambrian Research* **66**, 123–149.

Jackson, C. (1999). *Characterization of Mesoproterozoic to Palaeozoic crustal evolution of western Dronning Maud Land. Study 3: Deformational history and thermochronology of the central Kirwanveggen*. Unpublished report. Pretoria: Department of Environmental Affairs and Tourism.

Jacobs, J. (1999). Neoproterozoic/Lower Palaeozoic events in Central Dronning Maud Land (East Antarctica). *Gondwana Research* **2**, 473–480.

Jacobs, J. & Thomas, R. J. (2004). Himalayan-type indenter-escape tectonics model for the southern part of the late Neoproterozoic–early Paleozoic East African–Antarctic orogen. *Geology* **32**, 721–724.

Jacobs, J., Ahrendt, H., Kreutzer, H. & Weber, K. (1995). K–Ar, ^{40}Ar–^{39}Ar and apatite fission-track evidence for Neoproterozoic and Mesozoic basement rejuvenation events in the Heimefrontfjella and Mannefallknausane (East Antarctica). *Precambrian Research* **75**, 251–262.

Jacobs, J., Fanning, C. M., Henjes-Kunst, F., Olesch, M. & Paech, H. (1998). Continuation of the Mozambique Belt into East Antarctica: Grenville-age metamorphism and polyphase Pan-African high-grade events in central Dronning Maud Land. *Journal of Geology* **106**, 385–406.

Jacobs, J., Bauer, W. & Fanning, C. M. (2003a). Late Neoproterozoic/Early Palaeozoic events in central Dronning Maud Land and significance for the southern extension of the East African Orogen into East Antarctica. *Precambrian Research* **126**, 27–53.

Jacobs, J., Fanning, C. M. & Bauer, W. (2003b). Timing of Grenville-age vs. Pan-African medium- to high grade metamorphism in western Dronning Maud Land (East Antarctica) and significance for correlations in Rodinia and Gondwana. *Precambrian Research* **125**, 1–20.

Jacobs, J., Bingen, B., Thomas, R. J., Bauer, W., Wingate, M. T. D. & Feitio, P. (2008a). Early Palaeozoic orogenic collapse and voluminous late-tectonic magmatism in Dronning

Maud Land and Mozambique: insights into the partially delaminated orogenic root of the East African–Antarctic Orogen?. In: Satish-Kumar, M., Motoyoshi, Y., Osanai, Y., Hiroi, Y. & Shiraishi, K. (eds) *Geodynamic Evolution of East Antarctica: A Key to the East-West Gondwana Connection. Geological Society, London, Special Publications* **308**, 69–90.

Jacobs, J., Pisarevsky, S., Thomas, R. J. & Becker, T. (2008b). The Kalahari Craton during the assembly and dispersal of Rodinia. *Precambrian Research* **160**, 142–158.

Kelsey, D. E. & Powell, R. (2011). Progress in linking accessory mineral growth and breakdown to major mineral evolution in metamorphic rocks: a thermodynamic approach in the Na_2O–CaO–K_2O–FeO–MgO–Al_2O_3–SiO_2–H_2O–TiO_2–ZrO_2 system. *Journal of Metamorphic Geology* **29**, 151–166.

Key, R. M., Charsley, T. J., Hackman, B. D., Wilkinson, A. F. T. & Rundle, C. C. (1989). Superimposed Upper Proterozoic collision-controlled orogenies in the Mozambique orogenic belt of Kenya. *Precambrian Research* **44**, 197–225.

Kleinschmidt, G. & Boger, S. D. (2009). The Bertrab, Littlewood and Moltke Nunataks of Prinz-Regent-Luitpold-Land (Coats Land)—enigma of East Antarctic geology. *Polarforschung* **78**, 95–104.

Kohn, M. J., Corrie, S. L. & Markley, C. (2015). The fall and rise of metamorphic zircon. *American Mineralogist* **100**, 897–908.

Konrad-Schmolke, M., Handy, M. R., Babist, J. & O'Brien, P. J. (2005). Thermodynamic modelling of diffusion-controlled garnet growth. *Contributions to Mineralogy and Petrology* **149**, 181–195.

Kooijman, E., Smit, M. A., Mezger, K. & Berndt, J. (2012). Trace element systematics in granulite facies rutile: implications for Zr geothermometry and provenance studies. *Journal of Metamorphic Geology* **30**, 397–412.

Kotkovà, J. & Harley, S. L. (2010). Anatexis during high-pressure crustal metamorphism: evidence from garnet–whole-rock REE relationships and zircon–rutile Ti–Zr thermometry in leucogranulites from the Bohemian Massif. *Journal of Petrology* **51**, 1967–2001.

Kröner, A., Sacchi, R., Jaeckel, P. T. & Costa, M. (1997). Kibaran magmatism and Pan-African granulite metamorphism in northern Mozambique: single zircon ages and regional implications. *Journal of African Earth Sciences* **25**, 467–484.

Kröner, A., Willner, A. P., Hegner, E., Jaeckel, P. & Nemchin, A. (2001). Single zircon ages, *PT* evolution and Nd isotopic systematics of high-grade gneisses in southern Malawi and their bearing on the evolution of the Mozambique belt in southeastern Africa. *Precambrian Research* **109**, 257–291.

Krynauw, J. R. (1996). A review of the geology of east Antarctica, with special reference to the *c.* 1000 Ma and c. 500 Ma events. *Terra Antartica* **3**, 77–89.

Lenoir, J.-L., Liégeois, J.-P., Küster, D., Utke, A., Matheis, G. & Haider, A. (1994). Origin and regional significance of late Precambrian and early Palaeozoic granitoids in the Pan-African belt of Somalia. *International Journal of Earth Sciences* **83**, 624–641.

Ludwig, K. R. (2003). Isoplot/Ex Version 3.00: a geological toolkit for Microsoft Excel. *Berkeley Geochronology Center Special Publication* **4**, 1–70.

Ludwig, K. R. (2008). Isoplot/Ex Version 3.75: a geological toolkit for Microsoft Excel. *Berkeley Geochronology Center Special Publication* **5**, 1–75.

Luvizotto, G. L. & Zack, T. (2009). Nb and Zr behavior in rutile during high-grade metamorphism and retrogression: an example from the Ivrea–Verbano Zone. *Chemical Geology* **261**, 303–317.

McGuire, A. V., Francis, C. A. & Dyar, M. D. (1992). Mineral standards for electron microprobe analysis of oxygen. *American Mineralogist* **77**, 1087–1091.

Markl, G., Bäuerle, J. & Grujic, D. (2000). Metamorphic evolution of Pan-African granulite facies metapelites from Southern Madagascar. *Precambrian Research* **102**, 47–68.

Marschall, H. R., Kalt, A. & Hanel, M. (2003). *P–T* evolution of a Variscan lower-crustal segment: a study of granulites from the Schwarzwald, Germany. *Journal of Petrology* **44**, 227–253.

Marschall, H. R., Hawkesworth, C. J., Storey, C. D., Dhuime, B., Leat, P. T., Meyer, H.-P. & Tamm-Buckle, S. (2010). The Annandagstoppane Granite, East Antarctica: evidence for Archaean intracrustal recycling in the Kaapvaal–Grunehogna Craton from zircon O and Hf isotopes. *Journal of Petrology* **51**, 2277–2301.

Marschall, H. R., Dohmen, R. & Ludwig, T. (2013a). Diffusion-induced fractionation of niobium and tantalum during continental crust formation. *Earth and Planetary Science Letters* **375**, 361–371.

Marschall, H. R., Hawkesworth, C. J. & Leat, P. T. (2013b). Mesoproterozoic subduction under the eastern edge of the Kalahari–Grunehogna Craton preceding Rodinia assembly: the Ritscherflya detrital zircon record, Ahlmannryggen (Dronning Maud Land, Antarctica). *Precambrian Research* **236**, 31–45.

Martin, A. K. & Hartnady, C. J. H. (1986). Plate tectonic development of the South West Indian Ocean: A revised reconstruction of East Antarctica and Africa. *Journal of Geophysical Research: Solid Earth* **91**, 4767–4786.

Meert, J. G. (2003). A synopsis of events related to the assembly of eastern Gondwana. *Tectonophysics* **362**, 1–40.

Meert, J. G. & Van Der Voo, R. (1996). Paleomagnetic and $^{40}Ar/^{39}Ar$ study of the Sinyai Dolerite, Kenya: implications for Gondwana assembly. *Journal of Geology* **104**, 131–142.

Mengel, F. & Rivers, T. (1991). Decompression reactions and *P–T* conditions in high-grade rocks, northern Labrador: *P–T–t* paths from individual samples and implications for early Proterozoic tectonic evolution. *Journal of Petrology* **32**, 139–167.

Mikhalsky, E. V., Beliatsky, B. V., Savva, E. V., Wetzel, H.-U., Fedorov, L. V. & Hahne, K. (1997). Reconnaissance geochronological data on polymetamorphic and igneous rocks of the Humboldt Mountains, Central Queen Maud Land, East Antarctica. In: Ricci, C. A. (ed.) *The Antarctic region: geological evolution and processes: Proceedings of the 7th International Symposium on Antarctic Earth Sciences, Siena. Terra Antarctica Publications*, p. 45–53.

Milisenda, C. C., Liew, T. C., Hofmann, A. W. & Kröner, A. (1988). Isotopic mapping of age provinces in Precambrian high-grade terrains: Sri Lanka. *Journal of Geology* **96**, 608–615.

Möller, A., Mezger, K. & Schenk, V. (2000). U–Pb dating of metamorphic minerals: Pan-African metamorphism and prolonged slow cooling of high pressure granulites in Tanzania, East Africa. *Precambrian Research* **104**, 123–146.

Moyes, A. B. & Groenewald, P. B. (1996). Isotopic constraints on Pan-African metamorphism in Dronning Maud Land, Antarctica. *Chemical Geology* **129**, 247–256.

Moyes, A. B., Barton, J. M. & Groenewald, P. B. (1993a). Late Proterozoic to Early Palaeozoic tectonism in Dronning Maud Land, Antarctica: supercontinental fragmentation and amalgamation. *Journal of the Geological Society, London* **150**, 833–842.

Moyes, A. B., Groenewald, P. B. & Brown, R. W. (1993b). Isotopic constraints on the age and origin of the Brattskarvet intrusive suite, Dronning Maud Land, Antarctica. *Chemical Geology* **106**, 453–466.

Nandakumar, V. & Harley, S. L. (2000). A reappraisal of the pressure–temperature path of granulites from the Kerala Khondalite belt, southern India. *Journal of Geology* **108**, 687–703.

Newton, R. C. & Perkins, D. (1982). Thermodynamic calibration of geobarometers based on the assemblages garnet–plagioclase–orthopyroxene (clinopyroxene)–quartz. *American Mineralogist* **67**, 203–222.

Oba, T. & Nicholls, I. A. (1986). Experimental study of cummingtonite and Ca–Na amphibole relations in the system Cum–Act–Pl–Qz–H_2O. *American Mineralogist* **71**, 1354–1365.

O'Brien, P. J. & Rötzler, J. (2003). High-pressure granulites: formation, recovery of peak conditions and implications for tectonics. *Journal of Metamorphic Geology* **21**, 3–20.

Pant, N. C., Kundu, A., D'Souza, M. J. & Saikia, A. (2013). Petrology of the Neoproterozoic granulites from Central Dronning Maud Land, East Antarctica—Implications for southward extension of East African Orogen (EAO). *Precambrian Research* **227**, 389–408.

Paulsson, O. & Austrheim, H. (2003). A geochronological and geochemical study of rocks from Gjelsvikfjella, Dronning Maud Land, Antarctica—implications for Mesoproterozoic correlations and assembly of Gondwana. *Precambrian Research* **125**, 113–138.

Powell, R. & Holland, T. (1994). Optimal geothermometry and geobarometry. *American Mineralogist* **79**, 120–133.

Powell, R. & Holland, T. (1999). Relating formulations of the thermodynamics of mineral solid solutions: Activity modeling of pyroxenes, amphiboles, and micas. *American Mineralogist* **84**, 1–14.

Ravikant, V. & Kundu, A. (1998). Reaction textures of retrograde pressure–temperature deformation paths from granulites of Schirmacher Hills, East Antarctica. *Journal of the Geological Society of India* **51**, 305–314.

Ravikant, V., Laux, J. H. & Pimentel, M. (2007). Sm–Nd and U–Pb isotopic constraints for crustal evolution during Late Neoproterozoic from rocks of the Schirmacher Oasis, East Antarctica: geodynamic development coeval with the East African Orogeny. In: Cooper, A. K., Raymond, C. R., Anderson, J., et al. (eds) *Antarctica: A Keystone in a Changing World—Online Proceedings of the 10th ISAES. Short Research Paper* doi: 10.3133/of2007-1047.srp007.

Riedel, S., Jacobs, J. & Jokat, W. (2013). Interpretation of new regional aeromagnetic data over Dronning Maud Land (East Antarctica). *Tectonophysics* **585**, 161–171.

Riley, T. R., Curtis, M. L., Leat, P. T. & Millar, I. L. (2009). The geochemistry of Middle Jurassic dykes associated with the Straumsvola–Tvora alkaline plutons, Dronning Maud Land, Antarctica and their association with the Karoo large igneous province. *Mineralogical Magazine* **73**, 205–226.

Sassi, F. P., Visonà, D., Ferrara, G., Gatto, G. O., Ibrahim, H. A., Said, A. A. & Tonarini, S. (1993). The crystalline basement of north Somalia: lithostratigraphy and the sequence of events. In: Abbate, E., Sagri, M. & Sassi, F. (eds) *Geology and Mineral Resources of Somalia and Sourrounding Regions. Relazioni e Monographie Agrarie Subtropicali e Tropicali Nuova Serie Istituto Agronomico l'Otremare, Firenze* **113**, 3–40.

Schuhmacher, M., De Chambost, E., McKeegan, K. D., Harrison, T. M. & Migeon, H. (1994). *In situ* dating of zircon with the CAMECA ims 1270. In: Benninghoven, A., Nihel, Y., Shimizu, R. & Werner, H. (eds) *Secondary Ion Mass Spectrometry*. John Wiley, pp. 919–922.

Schwandt, C. S., Cygan, R. T. & Westrich, H. R. (1996). Ca self-diffusion in grossular garnet. *American Mineralogist* **81**, 448–451.

Seifert, F. & Langner, K. (1970). Stability relations of chromium kyanite at high pressures and temperatures. *Contributions to Mineralogy and Petrology* **28**, 9–18.

Shiraishi, K. & Kojima, S. (1987). Basic and intermediate gneisses from the western part of the Sør Rondane Mountains, East Antarctica. In: Yoshida, Y., Ejiri, M., Hiroi, Y., et al. (eds) *Proceedings of the NIPR Symposium on Antarctic Geosciences. National Institute of Polar Research*, **1**, pp. 129–149.

Shiraishi, K., Dunkley, D. J., Hokada, T., Fanning, C. M., Kagami, H. & Hamamoto, T. (2008). Geochronological constraints on the Late Proterozoic to Cambrian crustal evolution of eastern Dronning Maud Land, East Antarctica: a synthesis of SHRIMP U–Pb age and Nd model age data. In: Satish-Kumar, M., Motoyoshi, Y., Osanai, Y., Hiroi, Y. & Shiraishi, K. (eds) *Geodynamic Evolution of East Antarctica: A Key to the East–West Gondwana Connection. Geological Society, London, Special Publications* **308**, 21–67.

Smith, A. G. & Hallam, A. (1970). The fit of the southern continents. *Nature* **255**, 139–144.

Stacey, J. S. & Kramers, J. D. (1975). Approximation of terrestrial lead isotope evolution by a two-stage model. *Earth and Planetary Science Letters* **26**, 207–221.

Thompson, A. B. & Connolly, J. A. D. (1995). Melting of the continental crust: Some thermal and petrological constraints on anatexis in continental collision zones and other tectonic settings. *Journal of Geophysical Research* **100**, 15565–15579.

Tomkins, H. S., Powell, R. & Ellis, D. J. (2007). The pressure dependence of the zirconium-in-rutile thermometer. *Journal of Metamorphic Geology* **25**, 703–713.

Tsunogae, T., Dunkley, D. J., Horie, K., Endo, T., Miyamoto, T. & Kato, M. (2014). Petrology and SHRIMP zircon geochronology of granulites from Vesleknausen, Lützow-Holm Complex, East Antarctica: Neoarchean magmatism and Neoproterozoic high-grade metamorphism. *Geoscience Frontiers* **5**, 167–182.

Vanderhaeghe, O. & Teyssier, C. (2001). Crustal-scale rheological transitions during late-orogenic collapse. *Tectonophysics* **335**, 211–228.

Van Orman, J. A. & Crispin, K. L. (2010). Diffusion in oxides. In: Zhang, Y. & Cherniak, D. J. (eds) *Diffusion in Minerals and Melts. Mineralogical Society of America and Geochemical Society, Reviews in Mineralogy and Geochemistry* **72**, 757–825.

Vielzeuf, D., Baronnet, A., Perchuk, A. L., Laporte, D. & Baker, M. B. (2007). Calcium diffusivity in alumino-silicate garnets: an experimental study. *Contributions to Mineralogy and Petrology* **154**, 153–170.

Wareham, C. D., Pankhurst, R. J., Thomas, R. J., Storey, B. C., Grantham, G. H., Jacobs, J. & Eglington, B. M. (1998). Pb, Nd, and Sr isotope mapping of Grenville-age crustal provinces in Rodinia. *Journal of Geology* **106**, 647–660.

Watson, E. B., Wark, D. A. & Thomas, J. B. (2006). Crystallization thermometers for zircon and rutile. *Contributions to Mineralogy and Petrology* **151**, 414–433.

White, R. W., Powell, R., Holland, T. J. B. & Worley, B. A. (2000). The effect of TiO_2 and Fe_2O_3 on metapelitic assemblages at greenschist and amphibolite facies conditions: mineral equilibria calculations in the system K_2O–FeO–MgO–Al_2O_3–SiO_2–H_2O–TiO_2–Fe_2O_3. *Journal of Metamorphic Geology* **18**, 497–512.

White, R. W., Powell, R. & Holland, T. J. B. (2001). Calculation of partial melting equilibria in the system Na_2O–CaO–K_2O–FeO–MgO–Al_2O_3–SiO_2–H_2O (NCKFMASH). *Journal of Metamorphic Geology* **19**, 139–153.

White, R. W., Powell, R. & Holland, T. J. B. (2007). Progress relating to calculation of partial melting equilibria for metapelites. *Journal of Metamorphic Geology* **25**, 511–527.

Whitney, D. L. & Evans, B. W. (2010). Abbreviations for names of rock-forming minerals. *American Mineralogist* **95**, 185–187.

Wiedenbeck, M., Allé, P., Corfu, F., Griffin, W. L., Meier, M., Oberli, F., Quadt, A. V., Roddick, J. C. & Spiegel, W. (1995). Three natural zircon standards for U–Th–Pb, Lu–Hf, trace element and REE analyses. *Geostandards Newsletter* **19**, 1–23.

Will, T. M., Frimmel, H. E., Zeh, A., Le Roux, P. & Schmädicke, E. (2010). Geochemical and isotopic constraints on the tectonic and crustal evolution of the Shackleton Range, East Antarctica, and correlation with other Gondwana crustal segments. *Precambrian Research* **180**, 85–112.

Williams, I. S. (1998). U–Th–Pb geochronology by ion microprobe. In: McKibben, M. A., Shanks, W. C., III & Ridley, W. I. (eds) *Applications of Microanalytical Techniques to Understanding Mineralizing Processes. Reviews in Economic Geology* **7**, 1–35.

Wolmarans, L. G. & Kent, L. E. (1982). Geological investigations in western Dronning Maud Land, Antarctica—a synthesis. *South African Journal of Antarctic Research* **2**, 1–93.

Yoshimura, Y., Motoyoshi, Y. & Miyamoto, T. (2008). Sapphirine + quartz association in garnet: implication for ultrahigh-temperature metamorphism at Rundvågshetta, Lützow-Holm Complex, East Antarctica. In: Satish-Kumar, M., Motoyoshi, Y., Osanai, Y., Hiroi, Y. & Shiraishi, K. (eds) *Geodynamic Evolution of East Antarctica: A Key to the East–West Gondwana Connection. Geological Society, London, Special Publications* **308**, 377–390.

Yuan, H., Gao, S., Liu, X., Li, H., Günther, D. & Wu, F. (2004). Accurate U–Pb age and trace element determinations of zircon by laser ablation–inductively coupled plasma-mass spectrometry. *Geostandards and Geoanalytical Research* **28**, 353–370.

Zack, T., Kronz, A., Foley, S. F. & Rivers, T. (2002). Trace element abundances in rutiles from eclogites and associated garnet mica schists. *Chemical Geology* **184**, 97–122.

Zack, T., Moraes, R. & Kronz, A. (2004). Temperature dependence of Zr in rutile: empirical calibration of a rutile thermometer. *Contributions to Mineralogy and Petrology* **148**, 471–488.

Zeh, A. (2006). Calculation of garnet fractionation in metamorphic rocks, with application to a flat-top, Y-rich garnet population from the Ruhla Crystalline Complex, Central Germany. *Journal of Petrology* **47**, 2335–2356.